January 2013

Model Pt- and Pd-based Electrocatalysts for Low Temperature Fuel Cells Applications

Selasi Ofoe Blavo
University of South Florida, selasi.blavo@gmail.com

Model Pt- and Pd-based Electrocatalysts for Low Temperature Fuel Cells Applications

by

Selasi O. Blavo

A dissertation submitted in partial fulfillment
of the requirements for the degree of
Doctor of Philosophy
Department of Chemical and Biomedical Engineering
College of Engineering
University of South Florida

Major Professor: John N. Kuhn, Ph.D.
Babu Joseph, Ph.D.
Alberto Sagüés, Ph.D.
Shengquian Ma, Ph.D.
Sylvia Thomas, Ph.D.

Date of Approval:
July 2, 2013

Keywords: Catalysis, Oxygen Reduction Reaction,
Cyclic Voltammetry, Electrocatalysis, Nanoparticles

DEDICATIONS

My parents,

Harry Osei Blavo and Margaret Lucy Blavo

ACKNOWLEDGMENTS

Dr. John N. Kuhn accepted the challenge of taking me own as a graduate student researcher. He guided me while giving me enough freedom, trusting that I would get to this point. He believed in me when I doubted myself. Thank you.

Dr. David Loveday was instrumental in helping me set-up the Electrochemistry equipment that was used to generate the data shown in this document. His patience in answering my questions as well as his depth of knowledge was reassuring.

My fiancée, Esther Lare, who has endured the brunt of my being devoted to this path, especially in the past few months.

Ms. Catherine Burton in the College of Engineering was very helpful in formatting my dissertation document according to the requirements of the college and the university. Her lighthearted nature and attention to detail made sure that this document was not going to be released until it was ready.

Mr. Bernard Batson, who at USF has been the silent voice cheering in my corner, the invisible committee member and a significant propulsion force behind me getting the exposure that I have been lucky to benefit from, for the 3.5 years I have been in Tampa.

Mr. Edward Haller, Lab Manager in the integrative biology electron microscope core was a very kind spirit who despite his extensive experience in TEM microscopy was eager to make his students and new recruits independent behind the microscope. This helped me build confidence and self-reliance.

Ms. Maria Sanchez & Ms. Shelby Krebs, my enterprising undergraduate colleagues who were always excited at the prospect of trying to make something new. Both passionate and hardworking, I was lucky to have them working on the projects.

TABLE OF CONTENTS

LIST OF TABLES

LIST OF FIGURES

ABSTRACT

In the search for alternative energy technologies, low temperature fuel cells continue to feature as technologies with the most promise for mass commercialization. Among the low temperature fuel cells, alkaline and proton exchange membrane fuel cells are the most popular. Alkaline fuel cells have typically been used for water generation as well as auxiliary power for space shuttles. Their bulkiness however makes them undesirable for other applications, especially in automobiles, where there is a great demand for alternative technologies to internal combustion engines. Proton exchange membrane fuel cells on the other hand possess numerous qualities including their compact size, high efficiency and versatility. Their mass implementation has however been delayed, because of cost among other reasons. Most of this cost is owed to the Pt/C catalyst that accounts for about half of the price of the PEM Fuel Cell. This catalyst is used to drive the sluggish oxygen reduction reaction that occurs at the cathode of the PEM Fuel Cell.

To overcome this obstacle, which is to make PEM Fuel Cell technology more affordable, reducing the amount Pt has traditionally been the approach. Another approach has been to find new ideal catalyst-support combinations that increase the intrinsic activity of the supported material. One more strategy has been to find lower cost alternative materials to Pt through synthetic and kinetic manipulations to rival or exceed the current oxygen reduction reaction activity benchmark.

To this end, Palladium has garnered significant interest as a monometallic entity. Its manipulation through synthetic chemistry to achieve different morphologies - which favor select

lattice planes - in turn promotes the oxygen reduction reaction to different degrees. In bimetallic or, in more recent times multimetallic frameworks, geometric and ligand effects can be used to form ideal compositions and morphologies that are synergistic for improved oxygen reduction reaction kinetics.

In this dissertation, we have explored three different approaches to make contributions to the catalysis and electrocatalysis body of literature. In the first instance, we look at the influence of ligand effects through the active incorporation of a PVP capping agent on the stability of ~3nm Pt NPs. Washed (no capping agent) and unwashed (with capping agent) batches of NPs were evaluated via cyclic voltammogram analyses to evaluate differences there might be between them. It was found that the current density measurements for unwashed particle batches were higher. This increase in current density was attributed to the monodentate and bidentate ligand bonding from the PVP, which increased as a function of cycle number and plateaued when the PVP was completely decomposed. The complete decomposition of PVP during the CV experiment was estimated to occur around 200 cycles.

The remaining portion of the dissertation explores the electrocatalytic properties of Palladium based NPs. The first instance, a monometallic study of Palladium cubes and dendrites was aimed at building on a recent publication on the enhanced ORR activity that was achieved with a PdPt bimetallic dendrite morphology. In our work, we sought to isolate the dendritic morphology properties of the monometallic Pd composition in order to understand what advantages could be achieved via this morphology. Pd cubes were used as a comparison, since they could be generated through the combination of a similar set of reagents simply by switching the order of addition. It was found that while there was no significant variation in the ORR activity as a function of morphology / shape, there was an interesting interaction between

hydrogen and the palladium NPs in the hydrogen oxidation region that varied as a function of shape. This led to further sorption and ethylene hydrogenation studies, which suggested that, the interaction between hydrogen and Pd depended on the environment. Within the electrochemical environment, the ECSA measured, suggested that hydrogen was being reversibly absorbed into the sub-surface octahedral sites of Pd. The higher ECSA for Pd cubes corroborated with higher sorption for Pd cubes as well. However ethylene hydrogenation showed that the fringes of the Pd dendrites provided additional sites for reaction, which in turn translated to higher conversion. Furthermore, through a Koutecky-Levich analysis, it was found out that the Pd dendrites while exhibiting slightly lower activity, favored the 4-electron oxygen reduction process more than the Pd cubes.

In the last part of this dissertation we explored the electrocatalytic properties of Pd-based bimetallic NPs under different morphologies including nanocages and sub-10nm alloys. With the inclusion of Ag, it was found out, through Koutecky-Levich analysis that the 4-electron process was better observed under alkaline conditions using a 0.1M $NaOH_{(aq)}$ electrolyte solution instead of a 0.1M $HClO_{4\,(aq)}$ for acidic media testing. It was found that, for PdAg nanocage morphologies, where the Pd galvanically replaced the Ag to form cages, the four-electron process was suited to thinner Pd shells. Indeed the average electron numbers measured for Ag nanocubes coated with a 6nm shell was in agreement, within reason of literature values for bulk Ag. However, since the binding energy that both metals have for OH is so close, the potential for contributions to the ORR kinetics in alkaline media by Pd is a potential consideration.

CHAPTER 1: INTRODUCTION TO LOW-TEMPERATURE FUEL CELL CATALYSIS

1.1 The Need for Alternative Energy

The continuing depletion of the world's fossil fuel resources has been a driving factor for the development of alternative fuel sources and technologies. This pursuit however has also been motivated by the desire to reduce the emission of toxic as well as greenhouse gases into the atmosphere, which have increased considerably. As of April 2013, the level of CO_2 recorded in the atmosphere was 398.35ppm - the highest value on record in human history and well on par to hit 400ppm (CO_2, www.now.org) Furthermore, the rate at which atmospheric CO_2 is increasing is more than 100% faster than it was during the industrial revolution and the highest ever recorded since the end of the last ice age [3]. Notwithstanding this tremendous consumption pattern, the growing human population and by inference its energy need is expected to continue to increase exponentially. This startling information suggests that at the current consumption rate and without a foreseeable decrease in the dependence on fossil fuels, the climate might be headed to a point of irreversible and substantial change.

The increase in the emission of greenhouse gases, which has steadily progressed in the aftermath of major world milestones such as the industrial revolution, has not led to change the means by which energy is traditionally generated. Today, the use of crude oil and natural gas from coal or from other sources continues to dominate the world's energy platform. However, the continued depletion of purported world proven reserves has triggered, in recent times, a financial incentive to move away from fossil fuels. This push is also informed by the desire by

some of the world's largest economies, like the United States, to become independent [4] of foreign sources of crude oil, which in a large number of cases are found in conflict prone regions of the world. It has been suggested that based on the United States Department Of Energy's Energy Information Administration annual report of proved world reserves of energy resources, there maybe as little as 43 more years of crude oil left and 61 and 148 years of natural gas and coal respectively (information based on 2006 levels and flows, DOE EIA) production data.

In light of these phenomena, the need to provide alternative energy technologies for many future generations to live comfortably is very important. Several alternative forms of technology, some proving to be more efficient and most proving to emit less greenhouse gases have been proposed. These include the use of photovoltaic (or solar) cells, which harness the sun's energy, and convert it to electricity, and geothermal energy, which takes advantage of the thermal energy, stored deep in the earth's crust. Hydroelectric, nuclear and wind-powered energy resources have also garnered some interest over the years. Still in more recent times, biofuels and fuel cells feature most prominently in the scientific and political discourse. Thus there are several forms of alternative energy technologies that have been proposed. However, among all of the forms of alternative energy technologies mentioned above, fuel cells offer one of the best alternatives by virtue of their high efficiency, minimal greenhouse gas emission [5] and long term deployment.

There has been resurgence in research interest revolving around fuel cells after they were first commercially employed for powering of space shuttles. Their use ensured that the shuttles generated auxiliary power, and water which could be used for human consumption.

1.2 Low Temperature Fuel Cells

There are generally six major types of fuel cell categories [1] as listed in Table 1. While their operation may adopt the same general mechanism, they vary based on variables such as the charge carrier, operating temperature and electrolyte solution. Currently, among the different types of fuel cells that have been listed here, PEMFCs, feature prominently in literature. Their small size and high efficiency makes them ideal candidates for automotive applications and replacement of internal combustion engines. In fact, the use of PEMFCs dates back to the first NASA space programs where they were used for energy generation and to provide the astronauts with clean drinking water. The Gemini program – as it was called - employed a 1kW fuel cell stack as an auxiliary power source. [6] This original fuel cell was however fundamentally flawed, due to the use of a polystyrene sulfonate (PSS) polymer membrane, which was not stable. As a result, the alkaline fuel cell (AFC) (also indicated in Table 1) became the FC of choice. In the late 1960s, Walter Grot of DuPont, would discover, what we know today as Nafion – replacing PSS - and this new component would dramatically improve the performance of PEMFCs. Indeed, Ballard started using a modified PEMFC system incorporating the use of Nafion. With this modification, a four-fold increase in current density measurements was observed as a function of voltage. [1, 7].

Nafion can be described as a copolymer consisting of tetrafluoroethylene (TFE or Teflon) and sulfonic acid ($-SO_3^-H^+$) containing-perfluorinated vinyl ether. [9, 10] While it was originally studied for its use as a membrane separator of chloralkali cells used in production of chlorine and sodium hydroxide, it was its use as an essential component of the proton exchange membrane assembly that would bring it to fame.

Table 1 A summary of the most common fuel cell types and their properties (adapted from Carrette et. al [1]). The properties of PEM Fuel Cells make it ideal for Transportation as well as small-scale applications

	Alkaline	**Proton exchange Membrane**	**Direct Methanol**	**Phosphoric Acid**	**Molten Carbonate**	**Solid Oxide**
Charge carrier in electrolyte	OH^-	H^+	H^+	H^+	$(CO_3)^{2-}$	O^{2-}
Operating Temperature (°C)	< 100	60 - 120	60 - 120	160 - 220	600 - 800	800 - 1000
Anodic Rxn	$H_2 + 2OH^- \rightarrow 2H_2O + 2e^-$	$H_2 \rightarrow 2H^+ + 2e^-$	$CH_3OH + H_2O \rightarrow CO_2 + 6H^+ + 6e^-$	$H_2 \rightarrow 2H^+ + 2e$	$H_2 + (CO_3)^{2-} \rightarrow H_2O + CO_2 + 2e^-$	$H_2 + O^{2-} \rightarrow 2H_2O + 2e^-$
Cathodic Rxn	$H_2O + 2e^- + 0.5O_2 \rightarrow 2OH^-$	$0.5O_2 + 2H^+ + 2e \rightarrow H_2O$	$1.5O_2 + 6H^+ + 6e^- \rightarrow 3H_2O$	$0.5O_2 + 2H^+ + 2e \rightarrow H_2O$	$0.5O_2 + CO_2 + 2e \rightarrow (CO_3)^-$	$0.5O_2 + 2e^- \rightarrow O^{2-}$
Applications	Transportation, Space, Military, Energy Storage Systems			Stationary Heat & Power	Stationary Heat & Power and Transportation	
Reliable Power	5 – 150kW	5 – 250kW	5kW	50kW – 1MW	100kW – 2MW	100 – 250kW

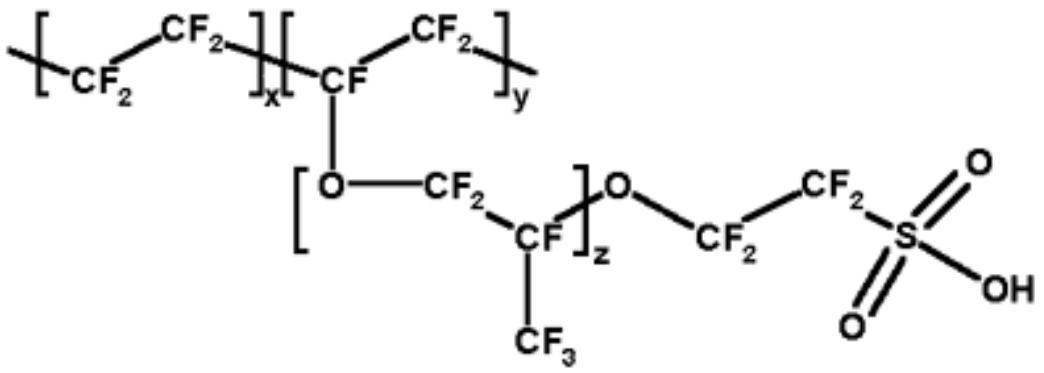

Figure 1 Molecular structure of Nafion® [8]

Ballard Power Systems started using a different membrane in their PEM fuel cells which gave about four times higher current densities at the same voltage and this discovery would launch a new field of research with stakeholders, such as Dow Chemicals and other research institutions and groups, heavily invested in it. [1, 7].

A typical PEMFC can be divided into three main constituent parts, i.e. the anode, the cathode and membrane assembly. Each component has a distinct function and together, they facilitate the generation of electricity from H_2 and O_2. During this process, fuel, typically in the form of pure H_2 (g), is admitted at the inlet (anode, eqn 1.1), with an outlet on the same side to let out excess H_2 (g). At the membrane assembly, protons selectively travel through a semi-permeable membrane constituted of – among other components – Nafion ®, a proton conductor

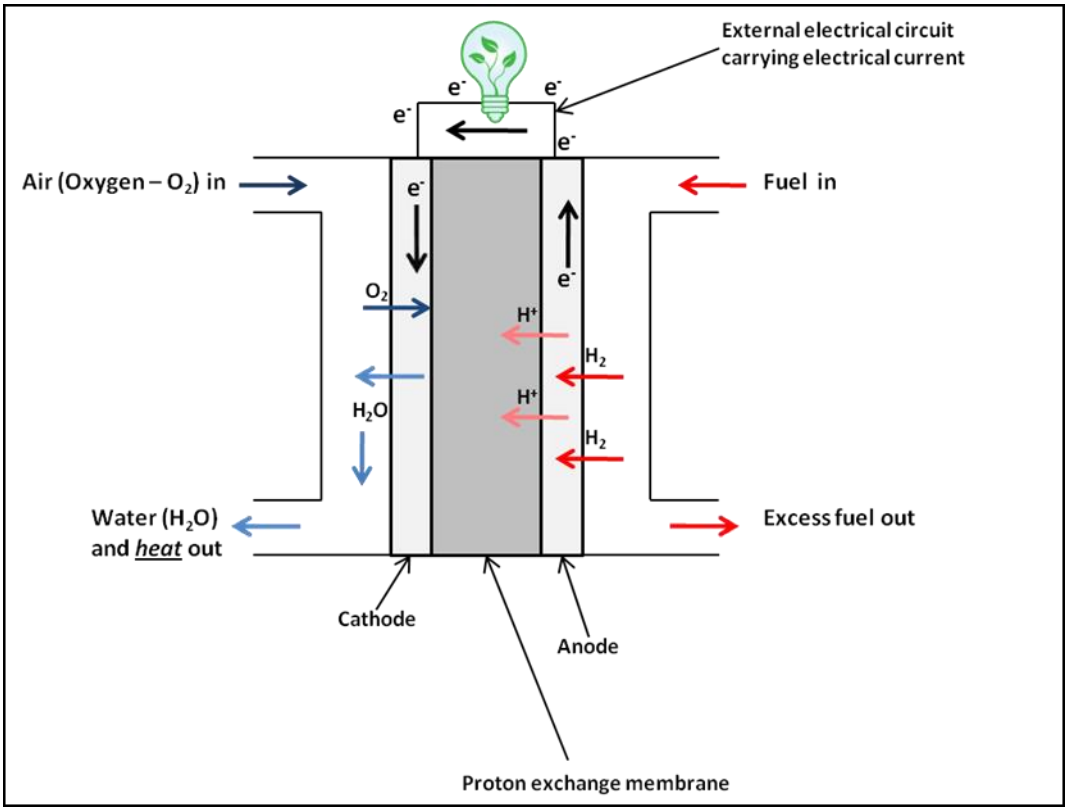

Figure 2 Illustrative operation of a generic low temperature fuel cell

The respective electrons are ejected from the atoms and out of the cell through an electrical circuit to generate electricity and power. On the opposite end of the PEMFC, i.e. the cathode (eqn 1.2), the ejected electrons recombine with O_2 (g) typically from the atmosphere and the protons from the MEA. This process results in the generation of water, H_2O (g) at a slightly elevated temperature (60 – 120°C).

$$H_2 \rightarrow 2H^+ + 2e^- \quad (1)$$

$$0.5\, O_2 + 2H^+ + 2e^- \rightarrow H_2O \quad , \quad (2)$$

Both reactions have traditionally facilitated though the use of a platinum catalyst. However both scenarios come with their own flaws. At the anode, an ideal scenario would involve the use of a pure stream of H_2 (g). A more realistic scenario however is one, which accounts for the inclusion of trace elements such as CO and S, which would come from the production of hydrogen through external processes. The presence of these trace elements, especially CO, can reduce the performance of the anode by poisoning the Pt catalyst. At the cathode, a combination of factors including the low partial pressure of atmospheric oxygen, the Ostwald-ripening of smaller Pt NPs [11] and the low operating temperature conditions of the fuel cell further retard the already slow kinetics of the oxygen reduction reaction. The traditional way to compensate for this loss in activity has been to increase the amount of Pt catalyst at the cathode. However the prohibitive cost of Pt as well as its scarcity suggests that this approach is uneconomical. It is for this reason that a number of different research groups, including ours have invested efforts into various ways of circumventing the current problem.

1.3 Catalysts for Low Temperature Fuel Cells

A traditional way of approaching the problem has been to reduce the amount of Pt being used by combining it with other materials in a bimetallic composition. To this extent, there have been several Pt-based studies published in the ORR electrocatalysis literature. Some have been focused on the combination of Pt with other materials [12-18] , while others have looked at different Pt – support combinations [19-23] ORR. Shape can also play an important part in catalytic and electrocatalytic reactions. Indeed, advances in synthetic chemistry now allow for the efficient control of size and shape at the nanoscale [24-28]

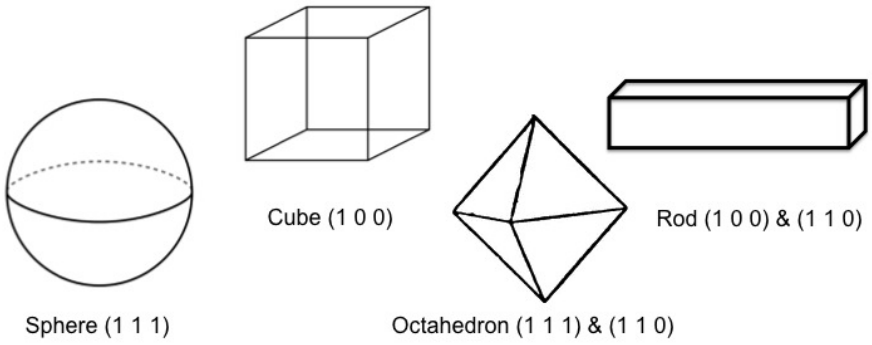

Figure 3 An illustration of a subset of different NP morphologies achievable through synthetic chemistry and the lattice facets they enclose (in parentheses).

Different shapes of NPs, by virtue of their geometry, can promote reactions to different extents. The underlying principle revolves around the prevalence of different lattice planes, which prevail as a function of particle morphology and the selectivity of these lattice planes towards a reaction pathway of interest. Previous work on single crystal modeling of the Pt – O_2 interaction [29] showed that oxygen reduction over the Pt (110) surface was more active and more selective to H_20 than the Pt (100) and (111) respectively. This also corresponds to a decreasing trend in surface coordination number, i.e. (1 1 0): 7 > (1 0 0): 8 > (1 1 1): 9 respectively [30]. This trend also correlates with the selectivity of the more kinetically favored morphologies, which demonstrate higher selectivity to H_2O reduction than the more thermodynamically favored ones.

A more recent approach, informed by density functional theory modeling proposes, the consideration of alternative materials that can replace the use of Pt in PEMFCs. Through, the computational screening of different materials, it is possible to rank different materials based on how their surface interacts with oxygen.

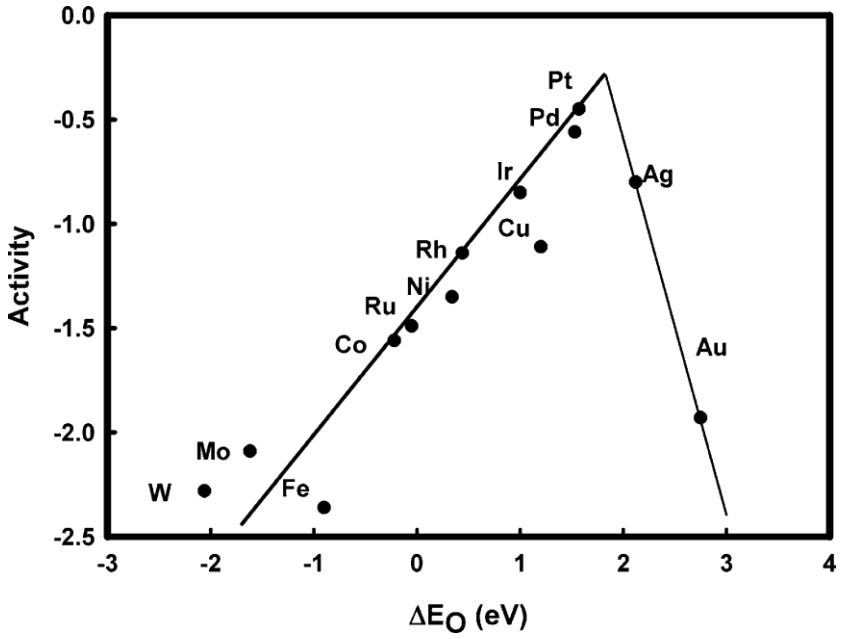

Figure 4 A volcano plot of the activity on the (111) surface of different metals. Image courtesy of Norskov et. al. [31]

Norskov et al. [31] , generated a ranking of different metal surfaces which was illustrated in the form of a volcano (figure 9), where the oxygen reduction activity is given as a function of the oxygen binding energy. From this diagram, the reasoning behind the adoption of Pt as an ideal Pt catalyst becomes evident. Platinum displays the best activity towards the oxygen reduction reaction. However, Pd falls right below Pt with a slightly lower binding energy and at approximately half the price of Pt (www.kitco.com) it is a potent contender to replace Pt as an electrocatalyst for PEMFCs.

1.4 Pd-based Electrocatalysts for Low Temperature Fuel Cells

Pd has traditionally been used for a number of different catalytic applications, particularly in the electronics and petroleum cracking industry. It has also been considered for hydrogen storage applications. More recently, the search for new catalysts for electrocatalysis as well as other catalytic applications primarily driven by advances in synthetic chemistry. Some of

the methods typically used have resulted in the generation of novel kinetically favored monometallic morphologies of Pd NPs. Indeed, Lee et al. [32] and more recently Niu et al [33, 34] have reported on elegant techniques for tailoring the shape of Pd nanocrystals by changing the kinetic parameters – some as simple as changing the order of added reagents - that govern the nucleation and growth of Pd nanoparticles. Other scientists have adopted the combination of palladium with other materials through the use of innovative processes of generating new compositions of NPs. Crooks et al. are well known for the galvanically deposited dendrimer-encapsulated mono-and bimetallic NPs [35-38]. Xia et al. are also well known for a variety of innovative new materials for different applications [39-42] including electrocatalysis. A major publication [43] looks at the combination of Pd with Pt in a dendrite framework which resulted in improved electrocatalytic properties vis-a-vis the status quo.

In the current work, the authors considered the different approaches that have been so far adopted in studying different materials. The current work is designed around three objectives. Through modifications in composition, morphology or the active incorporation of a surfactant, this dissertation presents a study of three different approaches to improving PEMFC electrocatalyst performance each of which builds on one of the major approaches aimed at improving PEM FC technology.

In a first instance, a monometallic study of palladium dendrites and cubes builds on the work by Xia et al. with the objective to isolate and capture the electrocatalytic properties of Pd and comparing it to that of Pd cubes as a basis of reference. A discussion on how morphology differences may affect influence hydrogen storage properties is also presented.

A second objective of this dissertation was to study the influence of new NP composition on the electrocatalytic properties of PdAg bimetallic NPs, through a synthesis technique

originally designed to generate Au nanocages, using Ag sacrificially. In this work, a modified synthesis was used to generate PdAg nanocages, which were compared with DEN synthesized bimetallic compositions of $PdNi_{11}$ & $PdAg_{11,}$ where the subscripts denote the molar ratios of each component.

A final objective was to study the electrocatalytic influence of the active incorporation of a surfactant / stabilizing agent. This was done using a system comprising ca. 3nm Pt NPs capped with PVP as a model system. The initial part of the work compared washed and unwashed NPs. A follow up to this work [44], not included here, looked at catalytic studies of PVP-Pt interaction via TPO experiments as a function of NP size.

Ligand and geometric [45-47] effects play an important role in improving the activity of bimetallic electrocatalysts [48]. Ligand effects rely on changing the electronic structure of the primary metal site [49] through which a favorable charge transfer is induced. Geometric effects include particle size, dispersion state and bond strain. These two properties inform the discussion sections of this work.

CHAPTER 2: EXPERIMENTAL METHODOLOGY

2.1 Syntheses

2.1.1 Aqueous Synthesis of Pd Cubes and Dendrites

Palladium nanoparticles on the order of 25nm were synthesized following a previously reported aqueous mechanism [32] for the synthesis of cubes and dendrites. Briefly, an initial volume of 47mL of Milli-Q (Direct-Q uv) water was introduced into a clean beaker and left stirring. A 1mL-aliquot of 5mmol K_2PdCl_4 was subsequently introduced into the reacting vessel. This was followed by the addition of 1mL aliquots of 5mmol CTAB and L-Ascorbic acid within 10 seconds of each other. While this sequence resulted in cubes, switching the order of the last two reagents yielded dendrites. Reagent grade solvents from Sigma Aldrich including K_2PdCl_4 (Potassium Tetrachloro Palladate IV); CTAB (Cetyl trimethyl ammonium bromide); and L-Ascorbic Acid were used in the process. A color change from dark yellow to dark brown confirmed the precipitation of the nanoparticles in solution. The final product was stirred for an additional 5 minutes prior to sitting it in a dark area overnight. The particles were washed to remove excess surfactant material. Washing consisted of centrifuging vials containing the particles, removing the supernatant material and re-suspending the particles in excess Milli-Q (Direct-Q uv) water. This process was continued for 3 additional cycles before supporting. Samples that were used for Transmission Electron Microscopy, X-Ray Diffraction and electrochemistry experiments were studied in unsupported batches. Electrochemistry samples were concentrated by centrifuging down to a minimal volume. Subsequently, measured

depositions were immobilized onto a glassy carbon electrode and bound with Nafion. Samples prepared for H_2-sorption and ethylene hydrogenation experiments were supported on enough Silica (Cab-O-Sil; Sigma-Aldrich) to make a 1wt % silica-supported palladium (Pd/SiO_2) system. The resulting composition was heated enough to evaporate the water then adequately stored for later use. In a similar fashion, 2wt% Vulcan carbon-supported palladium (Pd/C) systems were prepared for Extended X-Ray absorption Fine Structure (EXAFS) experiments.

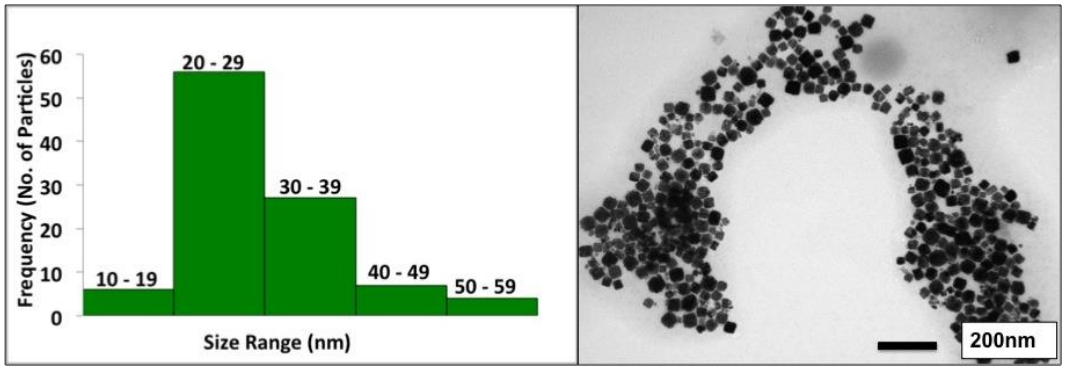

Figure 5 Histogram indicating ranges for Pd cube sizes. The bulk of the cubes fall in the 20 – 40nm range (left). Typical distribution of Pd cubes with average cube size ca. 25nm (right)

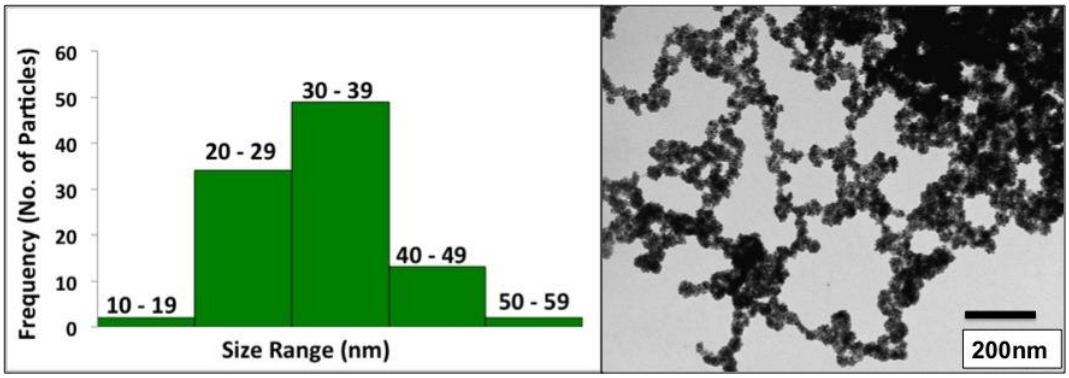

Figure 6 Histogram indicating ranges for Pd dendrite sizes. The bulk of the cubes fall in the 20 – 40nm range (left). Typical distribution of Pd dendrites with average cube size ca. 21nm (right)

2.1.2 Reflux Synthesis of Pt and Ag NPs

Platinum nanoparticles of approximately 3nm were synthesized using a procedure originally adopted from Kuhn et al. [25]. The same technique was adapted to the synthesis of silver nanoparticles of a similar size (employed for a different application). Briefly, 62.15 mg reagent grade chloroplatinic acid ($H_2PtCl_{6;}$ Sigma-Aldrich) was used as precursor. This was combined with 20 mL of de-ionized water, 133 mg of solid polyvinyl pyrolydone (PVP; MW: 40,000 g/mol; Sigma-Aldrich) and 180 mL of methanol in a reaction vessel. The reactor was lowered into an oil bath maintained at 110^{o}C. The reflux process was carried out for three hours without stirring. During this process the solution turned a dark brown or yellow color, confirming the precipitation of the Pt NPs Upon completion of the refluxing process, the supernatant (methanol) was evaporated at 55^{o}C. The remaining suspension was subsequently re-dispersed in ethanol. Select batches of NPs were washed by adding a combination of ethanol and hexane in a 1:3 ratio. This suspension was sonicated for 15 minutes, spun in a centrifuge (VWR clinical 100 centrifuge) at 3000rpm for 10 minutes and the supernatant pipetted off. This process was repeated until the resulting suspension was deemed satisfactorily clear of any surfactant material. This was typically after three cycles. Finally the NP suspensions were suspended in excess ethanol for further studies. Batches of washed and unwashed NP suspensions differed only in the inclusion or omission of this process. Images of the washed and unwashed particles as well as catalytic results are the topic of a first publication on this topic. [50]

2.1.2 Dendrimer-Encapsulated NP Synthesis

A series of bimetallic PdAg and PdNi NPs were synthesized to achieve particle sizes in the range of 1 – 10nm, a range, which is directly relevant for numerous catalytic applications including low temperature PEMFC electrocatalysis. This process was carried out via a complexation / co-complexation technique. The name of the technique originates from the initial

step in this process, which involves the complexation – in the case of a monometallic system; or a co-complexation - in the case of a bimetallic system of the respective ions in controlled volumes and concentrations with the tertiary amine groups within fourth generation PAMAM-OH or (G4-OH) to form G4-OH (M_1^{m+}(x) M_2^{m+}(40-x)), where M_1^{m+} and M_2^{m+} represent the metal ions involved in the synthesis and x represent the equivalent ratios. Dendrimers were purchased from Sigma-Aldrich (10% in methanol) with no further purification performed before use.

In a scintillation vial, 10mls of a 250 μM stock solution was prepared by combining an appropriate volume of the dendrimer solution with enough argon-bubbled "in-house" DI water. In addition, a 40-mol equivalent of solutions containing the desired precursor was prepared. For monometallic Pd experiments, a 0.01M solution of Pd^{2+} from $PdCl_2$; (research grade; from Sigma-Aldrich) salt was added to 1.5mL of the 250μM dendrimer solution. In the case of bimetallic systems, a combination of appropriate volumes of the desired salts, e.g. Pd^{2+} from 0.01M $PdCl_2$ and Ni^{2+} from 0.01M $NiCl_2$ was used in a ratio, which reflects the desired composition.

Table 2 shows typical concentrations and volumes associated with the different ratios. Differences in chelation rates also dictated the order in which the solutions were added. Upon completion of the complexation reaction, excess $NaBH_4$ was added to the reaction vessel, prompting the reduction of the ions to a monometallic or bimetallic composition of NPs. The fresh NPs, still enfolded by the dendrimer framework, were purified via dialysis through dialysis cellulose tubing membranes/sacks (Sigma-Aldrich; max MW: 12000). Dialyses occurred over a 24-hour period with the bags lodged in a 1L DI-water bath with 4 equivalent volume water

changes. At the end of the 24 hr. period, the synthesis was considered complete and the NP suspension was transferred and stored in a scintillation vial for further studies.

Table 2 Ratios and concentrations for the different compositions of Pd-Ag and Pd-Ni NPs used to generate bimetallic NPs

Ratio	Concentration
Pd : Ag (1:2)	660µL (0.01M K_2PdCl_4) 1318µL (0.01M $AgNO_3$)
Pd : Ag (1:1)	930µL (0.01M K_2PdCl_4) 930µL (0.01M $AgNO_3$)
Pd : Ag (2:1)	1311µL (0.01M K_2PdCl_4) 655µL (0.01M $AgNO_3$)
Pd : Ni (1:2)	615µL (0.01M K_2PdCl_4) 1230µL (0.01M $NiCl_2$)
Pd : Ni (1:1)	986µL (0.01M K_2PdCl_4) 986µL (0.01M $NiCl_2$)
Pd :Ni (2:1)	1299µL (0.01M K_2PdCl_4) 650µL (0.01M $NiCl_2$)

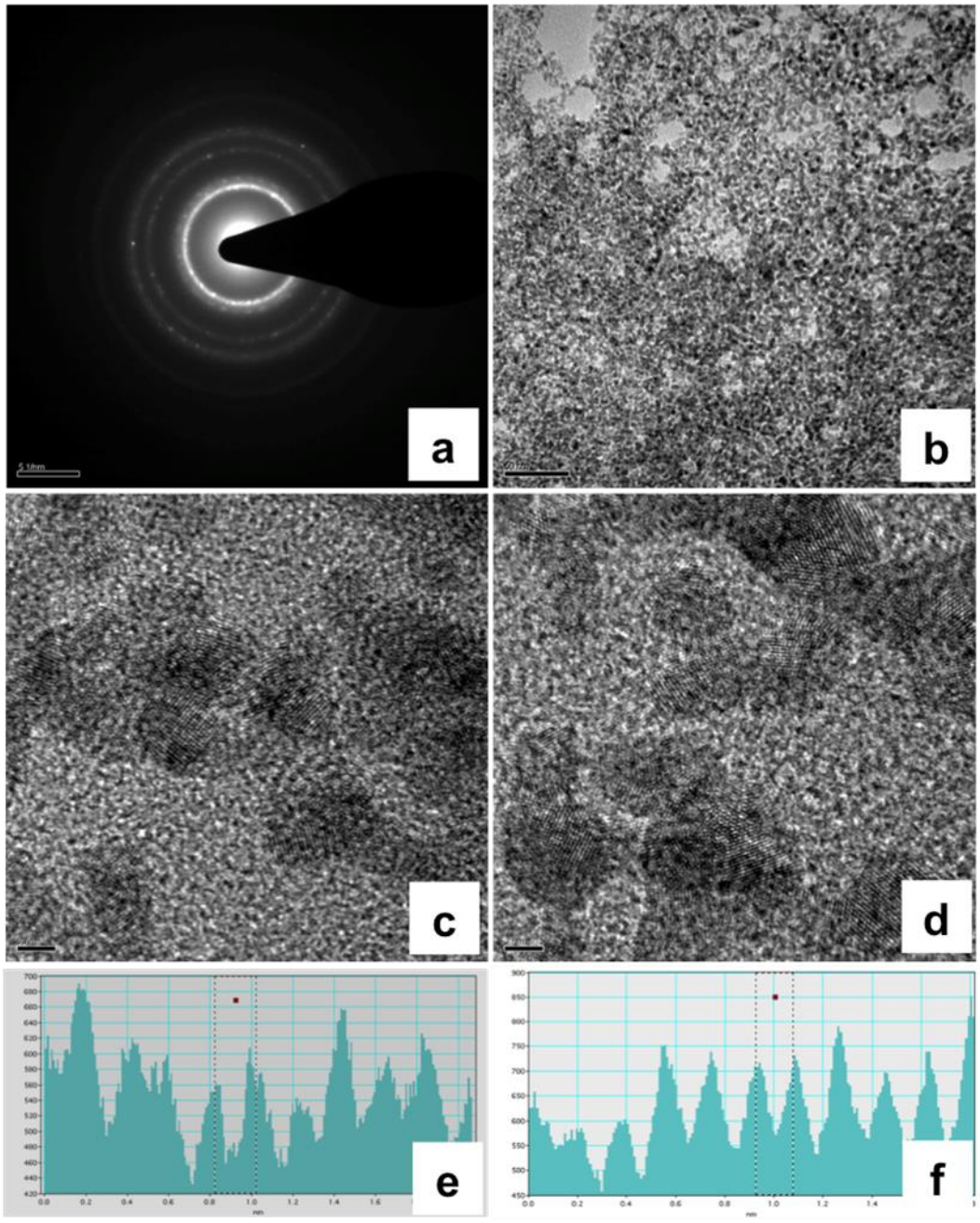

Figure 7 Series of images representing a mixture of Pd and Ag nanoparticles ~2nm. (a-f: EDX Diffraction pattern for P/Ag mixture illustrating rings resulting as a mixture; low resolution image (Scale bar: 60nm); c, d: High resolution images of different regions on carbon grid illustrating physical mixture of Pd and Ag NPs respectively (Scale bar: 2nm); e, f: Atomic spacing identification of individual Pd and Ag NPs, illustrating physical composition of discrete Pd and Ag NPs respectively.

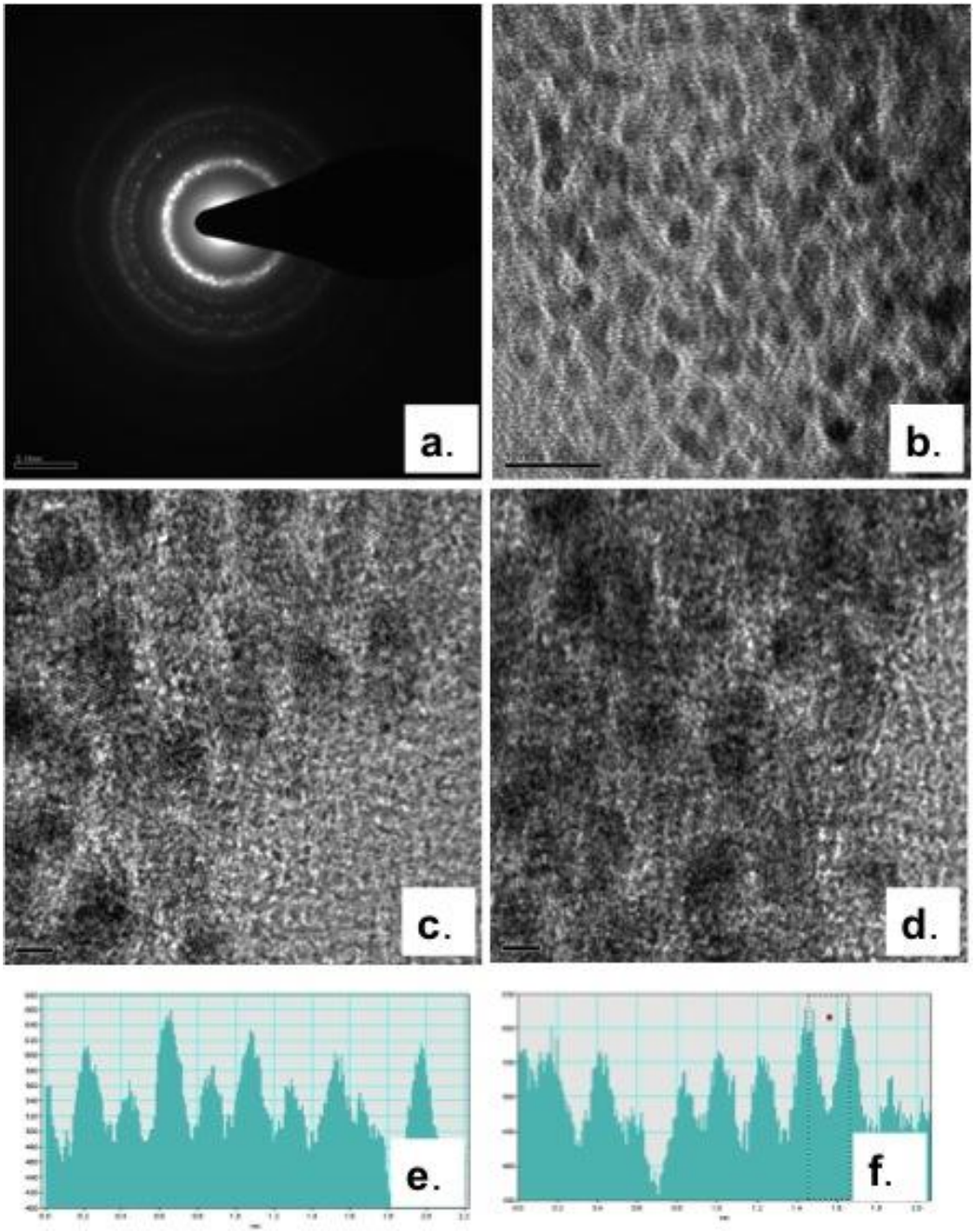

Figure 8 Series of images representing a mixture of Pd and Ni nanoparticles ~2nm. (a,b: EDX Diffraction pattern for P/Ni mixture illustrating rings resulting as a mixture; low resolution image (Scale bar: 10nm); c, d: High resolution images of different regions on carbon grid illustrating physical mixture of Pd and Ni NPs respectively (Scale bar: 2nm); e, f: Atomic spacing identification of individual Pd and Ni NPs, illustrating presence of discrete Pd and Ag NPs respectively

2.1.3 Bimetallic Pd-Ag Nanocages

Hollow cubes were synthesized with a shell consisting of Pd and Ag with trace amounts of Cu. This synthesis process consisted of three different steps. The first step, adopted from Tao et. al [51] involved the polyol synthesis of Ag nanocubes. The as synthesized Ag nanocubes were used as seeds and enhanced with a Pd shell through a similar polyol synthesis technique. Three different shell thicknesses were obtained (5, 6 and 10nm) based on the combination of surfactant and precursor amounts used. Depending on the shell thickness desired, 0.005, 0.1125 or 0.025mmol of Ammonium hexachloropalladate (IV) ($(NH_4)_2PdCl_6$; Sigma-Aldrich) was dissolved together with 2mmol PVP in 9mL (1,5-pentanediol) and purged under an Ar stream for 10 minutes in a three-necked reaction vessel. To this mixture, 1mL of the as-synthesized Ag nanocubes was injected. After adequate mixing, the reaction vessel was maintained at 140^{o}C in an oil bath for 20 minutes under a stream of Ar gas. The resulting NPs were precipitated with excess acetone after cooling.

The resulting NPs were then washed using a procedure previously described and reported. [44, 50, 52] However, centrifuging was done at 6500rpm and the volumes of ethanol and hexane were 1 and 14mL respectively. The washed NPs were finally suspended in an excess of ethanol for characterization, imaging. Details of the imagery as well as the NP composition details can be found in the work of Hokenek et al. [53].

2.2 Electrocatalysis

Electrocatalysis involves the study of catalytic phenomena within an electrochemical environment. This topic encompasses a suite of experimental electrochemical techniques, which are essential for the study, and elucidation of ideal electrocatalysts for PEMFC applications. In

this work, the CV and LSV/ORR techniques were primarily used in tandem with traditional characterization and catalytic experiments to study electrocatalysts.

An understanding of the reactions occurring with a PEMFC allows us to replicate a similar environment using an electrochemistry set-up in order to explore the catalytic properties of model catalysts under consideration. The highly sensitive nature of electrochemical studies requires that prior to each experiment, the electrochemical cell was washed out with aqua regia and allowed to sit over night. Subsequently, it was rinsed out with copious amounts of tap water followed by DI water. It was also rinsed with 0.1M $HClO_4$ or 0.1NaOH, the electrolyte solution it would eventually hold. The experimental set-up itself consisted of a three-electrode electrochemical reactor including a reference electrode, a counter electrode and a working electrode. The reference electrode consisted of a SCE whose potential was routinely measured against second reference electrode – reserved for this singular purpose - in order to maintain accurate readings. Measured potential differences of less than 5mV were considered small enough to ignore, however differences above this value prompted a replacement of the containing fluid, saturated KCl, obtained directly from GAMRY Instruments ®. The counter electrode (Pine) consisted of a coiled platinum wire fitted on the tip of a chemically resistant epoxy rod. The working electrode assembly consisted of a GCE RDE tip fitted into a holding shaft and secured in place by a RDE710 rotator to establish the working electrode. The RDE tip was occasionally replaced by an RRDE tip on which the GC center was surrounded by a platinum ring.

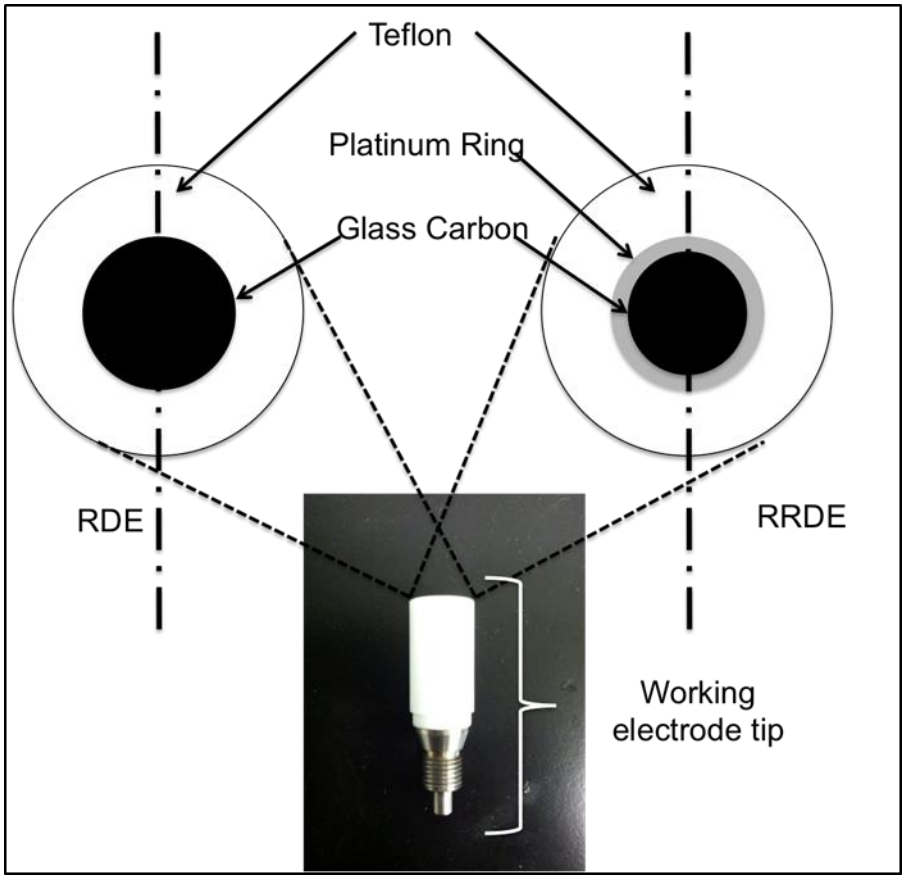

Figure 9 An illustration of the two different types of electrode tips, highlighting their differences. The RRDE tip (right) incorporated a Platinum ring for H_2O_2 detection and reduction while, the RDE tip (left) is equipped only with the GCE core.

The use of either the RDE or RRDE tip was determined by the chemistry of the reactions being studied; a detailed explanation is given later in this document. Occasionally, the electrochemistry assembly was calibrated to ensure continual accuracy and repeatability of measurements. *Reference 3000*™ (Gamry Instruments) and *Reference 600*™ (Gamry Instruments) were used for all experiments.

2.2.1 Electrode Preparation

The working electrode was prepared by mechanically immobilizing a measured volume of the NP suspension onto the glassy carbon center portion of the electrode tip. Each deposition

was air-dried before a subsequent one was made to prevent the spread of the NP film onto the Teflon sleeve. Upon drying, a very thin film of Nafion® 117 (Sigma-Aldrich) was added to bind the NP film to the GCE in addition to facilitating proton conduction. Such a preparation ensures good communication of the NP film with the GCE by virtue of the Nafion® which increases the surface area in communication with the GCE. After each experiment, the electrode tip was mechanically polished on a polishing cloth (BUEHLER®) doused with a small amount of deagglomerated gamma 0.05 micropolish II (BUEHLER®). The polishing process, executed by repeatedly drawing a figure eight in the polish, was continued till the GCE center showed a distinct shiny reflection. Upon satisfactory polishing, the GCE tip was washed with tap, then DI water and subsequently sonicated for five minutes in a FS20H ultrasonicator (Fisher Scientific). This process completed the cleaning of the electrode tip, readying it for a subsequent experiment. NP films that consisted of a thin film of nafion with NPs from the aqueous synthesis (Chapter 4) were more robust and stable than others (Chapter 5), which were based on the combination of nafion with DENs and organically synthesized NP films. The result of this lack in film quality was manifested in the ORR curves recorded.

2.2.2 Cyclic Voltammetry

Within the realm of electrocatalysis, a typical CV experiment consists of measuring the current density response of a modified working electrode. Current density is recorded as a function of a reversible ramp in its potential difference, measured with respect to a reference electrode. In addition to the material composition of the working electrode, the current density response will also vary based on a number of other factors including but not limited to the rotator speed, the amount of material on the electrode, and the concentration and purity of the electrolyte solution. A typical Pd or Pt CV scan consists of three distinct regions, half of which is in the

anodic sweep and the other in the cathodic. The three regions include the HER and OER, corresponding to where H_2 (g) and O_2 (g) respectively are evolved. A third region - the DLR, separates these two regions.

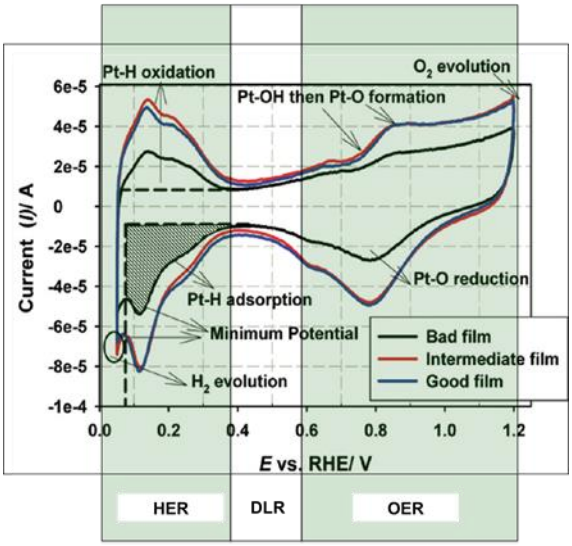

Figure 10 Pt/C Cyclic voltammogram showing HOR, DLR & OER.(Garsany et al. [54])

Two important properties of a material that can be obtained from the CV experiment include the electrochemically active surface area, ECSA and the stability of the material as a function of the cycle / time. By definition, the ECSA is a quantification of the region of the modified working electrode, where actual electron exchange takes place. [55] This is not to be confused with the geometric surface area, which is the visible physical area of the electrode (GCE) as indicated in figure 9 It also differs from the idea of a traditional catalyst surface area, [56] which refers to the number of active sites, which facilitate adsorption, species formation and desorption, all within the pores of a given catalyst material. In general, the higher the ECSA is, the better. It can be measured by integrating the H_2 adsorption region of the cathodic sweep in the HER (see shaded area in figure 10) between the hydrogen evolution peak and DLR. The resulting coulombic charge obtained can be converted, using a previously determined and widely

accepted conversion factor of 212μC/cm^2 [57-60] between the monolayer adsorption maximum and the double layer region as illustrated in figure 10. Stability tests of the electrocatalysts give an indication of how efficient the NP film is over time. Extended CV experiments (on the order of hours or days) can be useful in establishing the rate at which ECSA is lost and, from there can be compared with other materials or NP film compositions.

The general procedure for CV experiments used here was adopted from Garsany et al. [54] and modified to suit the current environment. Briefly, an extended CV experiment was run over several hours to establish a trend in the ECSA loss and identify a point at which the electrode was clean to establish a measurement. CV scans were recorded between 0 and 1.2V RHE (-0.244 and 956 SCE) at 1600rpm. A scan rate of 20mV/s was used to minimize noise contributions while effectively accommodating the distinct features of the CV scan and scan rate of 20mV/s. The electrolyte solution consisted of a freshly prepared 100mL of Ar-bubbled 0.1M $HClO_4$ (aq). All CVs reported were normalized by the geometric surface area of the GCE (0.1964cm^2).

2.2.3 Linear Sweep Voltammetry (LSV) / Oxygen Reduction Reaction (ORR)

ORR experiments constitute an important experiment in evaluating the activity of electrocatalysts. The ORR experiment is similar to the CV experiment since it involves the measure of a current density as a function of a voltage ramp. It does however differ in two distinct manners. Firstly, the voltage sweep is typically carried out in the cathodic direction only. Secondly, it is conducted in an O_2 (g) saturated electrolyte solution, though a second identical scan is recorded in an Ar (g) saturated electrolyte solution. The latter is then subtracted from the former to account for capacitive current contributions from the electrolyte solution, which must be extracted to reveal the absolute ORR profile.

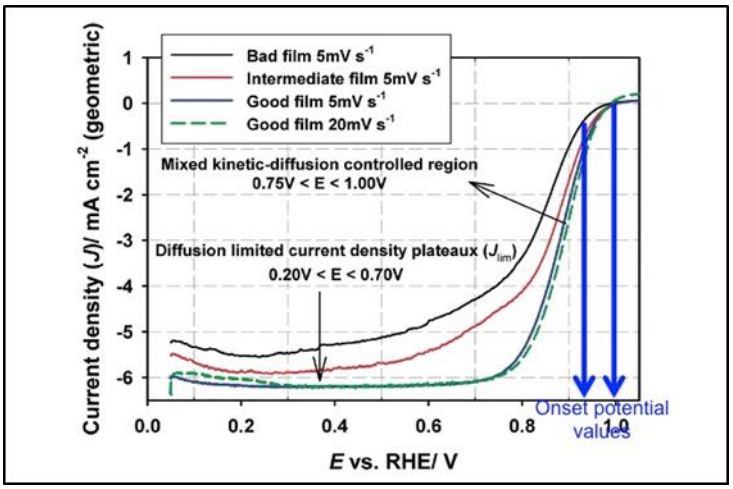

Figure 11 Typical ORR curves (for Pt/C) Adapted from (Garsany et al. [54]) with a designation of the onset potentials corresponding to the different curves.

There are two significant pieces of information that can be obtained from an ORR curve. The first is the onset potential. This refers to the first inflexion point on a cathodic sweep ORR curve or the potential at which the O_2 (g) reduction process starts. It is an intrinsic property of the given electrocatalyst. This property may however be varied by manipulating the properties of the electrocatalyst NPs. It can also vary by virtue of human error or a lack in experiment quality. Typical factors that may contribute to such variations include the quality of the NP film on the WE, the accuracy of the RE, cleanliness of the electrochemical reactor and by inference the absence of impurities from the electrolyte solution. The second piece of information relates to the pathway that is followed in the reduction of O_2 (g) to H_2O(l/g).

$$O_{2(g)} + 4H^+(aq) + 4e^-(aq) \rightarrow 2H_2O\ (l), \qquad E^o = 1.2V \tag{3}$$

There are two pathways to O_2 reduction that are typically observed during an ORR experiment. The first is one illustrated above in (3) assumes that there are no intermediate species and that the formation of water proceeds directly.

$$O_{2(g)} + 2H^+_{(aq)} + 2e^-_{(aq)} \rightarrow H_2O_{2(aq)}, \qquad E^o = 0.68V \tag{4}$$

$$H_2O_{2(aq)} + 2H^+_{(aq)} + 2e^-_{(aq)} \rightarrow 2H_2O_{(aq)}, \qquad E^o = 1.77V \tag{5}$$

The second pathway, the presence of an intermediate species in the form of H_2O_2 is accounted for as seen in (4) and (5). While both pathways end up in the formation of H_2O (l), one particular catalyst may favor one pathway over another. It is possible to determine the pathway that is favored by a particular electrocatalyst by carrying out a series of ORR curves at different rotation speeds (rpm) and fitting the resulting data to a Koutecky-Levich. [61, 62]

The Koutecky-Levich plot is the graph of a straight line, which plots the inverse of the mass transport-limited current, $i_d(i_L)$ at different points on the ORR curve for different rotation rates (ω) as a function of the inverse of the said rotation rate, i.e. $(1/\omega)^{0.5}$. The measured current, i_m is a function of the kinetic current, i_k and the mass transport-limited current, i_d. Furthermore, i_d is a function of the Faraday constant, F (96500 Coulombs per mole, $Cmol^{-1}$); the concentration of dissolved gaseous species, C_{O2} (1.3×10^{-3} moles per decimeter-cubed, $moldm^{-3}$) [63]; the diffusivity of the gaseous species, i.e. D_{O2} in 0.1 $HClO_4$ (1.7×10^{-5} centimeter-squared per second, cm^2s^{-1}); the rotation rate, ω (revolutions per minute, rpms) and the kinetic viscosity, ν (1.0×10^{-2} centimeter-squared per second, cm^2s^{-1}) of the electrolyte solution and the geometric surface area, A. All combined, the Levich equation [64-66] presents a form, which accommodates all the above-mentioned parameters as follows:

$$\frac{1}{i_m} = \frac{1}{i_k} + \frac{1}{i_d} = \frac{1}{i_k} + \frac{1}{0.2nFAD_{O_2}^{\frac{2}{3}} C_{O_2} \omega^{\frac{1}{2}} \nu^{\frac{-1}{6}}} \quad (6)$$

By recognizing that the Levich equation satisfies the requirements for a straight-line plot, a simplification can be made acknowledging all constant terms with a new generic encompassing constant, B. This new modification brings about a simpler form of the Levich equation as follows:

$$\frac{1}{i_m} = \frac{1}{i_k} + \frac{1}{i_d} = \frac{1}{i_k} + \frac{1}{B\omega^{\frac{1}{2}}} \quad (7)$$

where,

$$B = 0.2nFAD_{O_2}^{\frac{2}{3}} C_{O_2} \nu^{\frac{-1}{6}} \quad (8)$$

In this form (8), we can recognize that a plot of the reciprocal of the measured current, i_m^{-1} as a function of the reciprocal square-root of the rotation rate, i.e. $\omega^{-0.5}$ would yield a straight line plot with its ordinate intercept corresponding to the value of the kinetic current, i_k and its slope, equal to the constant B, from where the number of electrons relevant to the electrocatalytic reaction can be extracted. This process of analysis forms the basis of the electrocatalytic evaluation for the different materials evaluated in this document.

2.3 Characterization

2.3.1 Transmission Electron Microscopy

A well-dispersed drop of the NP/BNP suspension was further diluted with hexane (or alcohol – methanol / ethanol) or DI water depending on solvent used during synthesis. The new

mixture was agitated via a Vortex Genie (Fisher Vortex Genie 2) and a drop of the new mixture was pipetted on to the carbon-coated side of a 200 sq. mesh copper grid (Electron Microscopy Sciences, FCF200-Cu) and suspended in a vacuum oven (Fisher Isotemp Vacuum 281A) maintained at 40°C till it was dry. NP/BNP images were obtained using a Tecnai t20 TEM as well as a Tecnai TF20 (200kV) TEM for high-resolution imagery, diffraction patterns as well as atomic plane signatures and EDX spectra. Additionally, atomic spacing and particle size (width – cubes; diameter - spheres, dendrites) distribution were determined via the ImageJ freeware, (NIH) and the ImageJ-based FIJI software.

2.3.2 X-Ray Diffraction

A Philips X-Ray diffractometer was used to generate the X-Ray profiles for desired NP/BNP samples that were synthesized. The instrument was operated at a tension of 45 KV and a current of 40 mA. Typical scans were operated with a step size of 0.02 degree equipped with Cu K [alpha] ([lambda] = 0.154 nm) radiation. Reported XRD pattern noise was reduced using the ***Magicplot*** $^{2.3}$™ plotting software.

2.3.3 X-Ray Absorption Spectroscopy

X-ray absorption spectroscopy (XAS) studies were performed at the DuPont-Northwestern-Dow (DND) Collaborative Access Team (CAT) beamline 5-BM-D (BM = bending magnet, http://www.dnd.aps.anl.gov/) at the Advanced Photon Source of Argonne National Laboratory. For these experiments, the storage ring energy and circulating current were 7.0 GeV and 100.6 mA, respectively. X-rays were selected using a Si (111) monochromator. NP batches examined were supported on VC (2% supported NPs)

CHAPTER 3: PLATINUM LIGAND EFFECTS[1]

3.1 Introduction

Despite many advances to replace the current Pt-based materials with Pt-free materials[67-73] or Pt-based bimetallic particles [74-77], efforts have not yet lead to an ideal material when evaluating both electrocatalytic turnover and cost factors [78]. Thus, it is envisioned that Pt components will be used in the foreseeable future therefore problems associated with its use must be addressed.

An important consideration regarding the use of Pt, or any metallic component, is stability against corrosion under PEMFC operation. In addition to the general notion of metals dissolving in acidic conditions, recent work[79] verified that small Pt particles are more vulnerable to corrosion as compared to large particles and bulk Pt. Additionally, Ostwald ripening, a phenomenon by which smaller (Pt) nanoparticles will dissolve and re deposit on to bigger NPs is of concern as observed by other scientists [66]. This trend compromises the efforts to use small Pt particles for their high surface area, which would lead to an efficient use of the precious metal. The addition of surface stabilizing agents, which would decrease the corrosion rate of Pt, is a method that could be used to enhance the stability of the metal-based ORR electrocatalysts.

[1] This chapter was published in ASTM International (Blavo, S., Baldyga, L., Sanchez, M., Kuhn, J.N., *The Effect of Stabilizing Agent on Platinum Nanoparticles and Implications Towards the Oxygen Reduction Reaction.* ASTM Int., 2011. **8**(9)) Permission is included in Appendix B

Advances in synthetic chemistry now permit the preparation of metal particles with size and shape control and many synthetic routes require the use of chemical additives for the control[80-85]. These chemical additives, also known as surfactants or capping agents, provide morphology control by regulating the metal's nucleation and growth kinetics. By modifying these properties, it is also possible that other properties are altered. In fact, changes in catalytic properties have been implied[86-88] and reported[89]. Other methods, such as use of non-carbon supports[90] and partial coverage of the metal surface by silica [91-93] for particle stabilization were reported for enhancement of Pt stability under conditions relevant to PEMFCs. Additionally, incorporation of organic molecules onto the surface of metal electrocatalysts is responsible for changes in ORR electrocatalysis. The addition of polypyrrole[94, 95] and macromolecular dendrimer polymers[96] were responsible for different product selectivity for ORR catalysis in the presence of methanol. The presence of polyvinylpyrrolidone (PVP) was deemed more important than even the integration of a second metal to Pt particles[97]. These studies suggest that capping agents used during colloidal synthesis of metal nanoparticles may serve a second function—the stabilization of metal particles under acidic conditions.

In this chapter, the role of PVP as a corrosion-resistant surface-stabilizing agent for Pt is evaluated and the approach is highlighted in Scheme 1. Monodisperse and spherical ca. 3 nm Pt particles were synthesized using a single-pot colloidal synthesis with PVP as a surfactant. Following the synthesis, the Pt particles were characterized and used for electrochemical testing. As a control, Pt particles from the same synthetic procedure were repeatedly washed via hexane-ethanol cycles to remove the PVP. The washing cycles do not impact the size or shape of the Pt particles whereas it does effectively remove the PVP as demonstrated by the carbon dioxide profiles observed during the temperature-programmed oxidation experiments. In electrochemical

testing, the Pt particles with PVP (unwashed) demonstrate greater stability than the PVP-free Pt particles (washed) and could provide the necessary stability for commercial realization of PEMFCs.

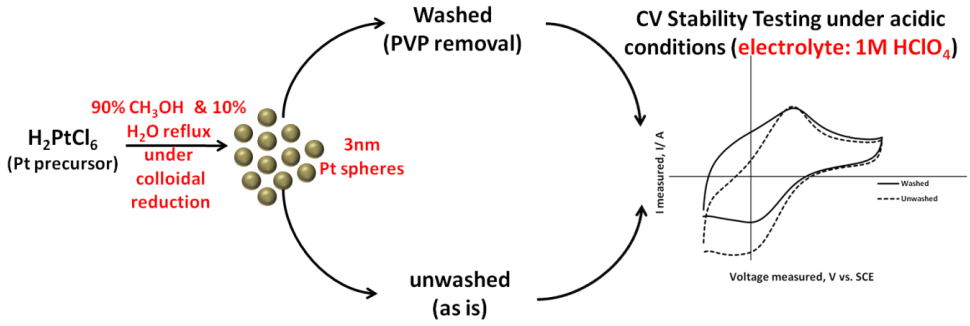

Figure 12 Sequence of experimental procedure from Pt particle synthesis through electrochemical testing.

3.2 Cyclic Voltammetry (CV) Experiment

GAMRY INSTRUMENTS suite of equipment (RDE710 Rotating Electrode, Reference 3000, Dr. Bob Electrochemical cell) was used for all CV experiments. Additionally, reference and counter electrodes, which consisted of a saturated calomel electrode, SCE and Platinum wire, were employed. The working electrode consisted of the rotating disk electrode shaft fitted with the Pt nanoparticle film deposited on the glassy carbon electrode (GCE). Samples were prepared by making thirty 10μL aliquot depositions of the platinum suspension on the GCE. The nature of the suspension required each aliquot to be dry before a subsequent one was added to ensure that all material was deposited on the glassy carbon amorphous surface.

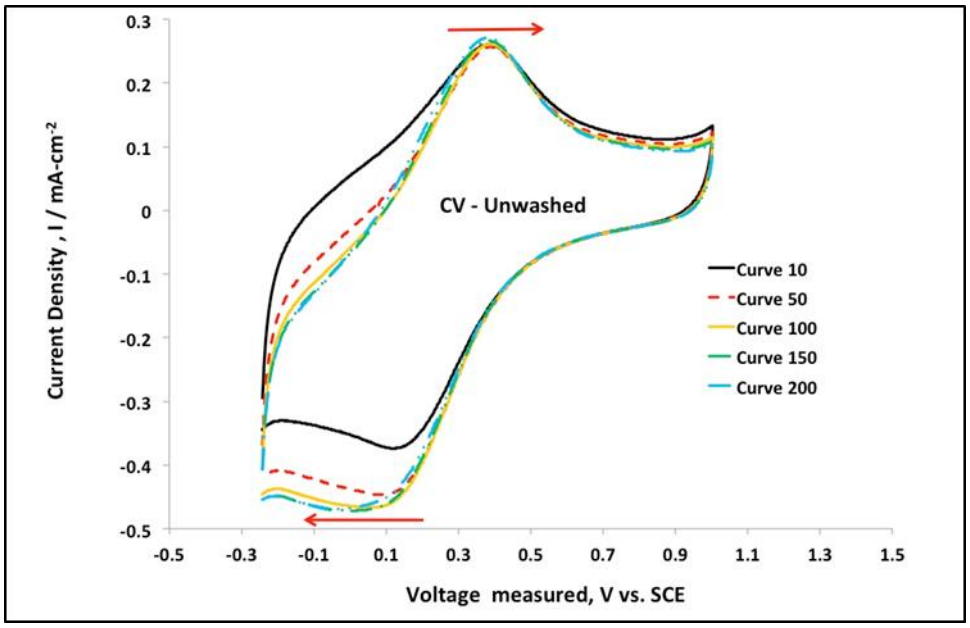

Figure 13 Cyclic Voltammetry Experiment of unwashed Pt NP. 200 cycles were recorded at a scan rate of 50mV/s and a step size of 2mV.

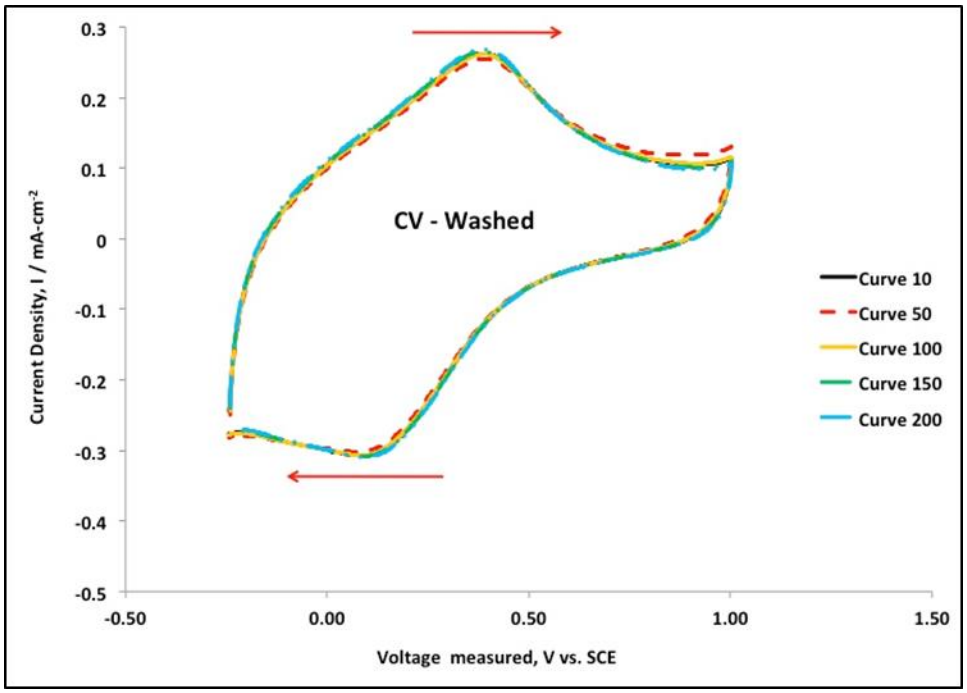

Figure 14 Cyclic Voltammetry Experiment of washed Pt NP. 200 cycles. Cycles were recorded at a scan rate of 50mV/s and a step size of 2mV.

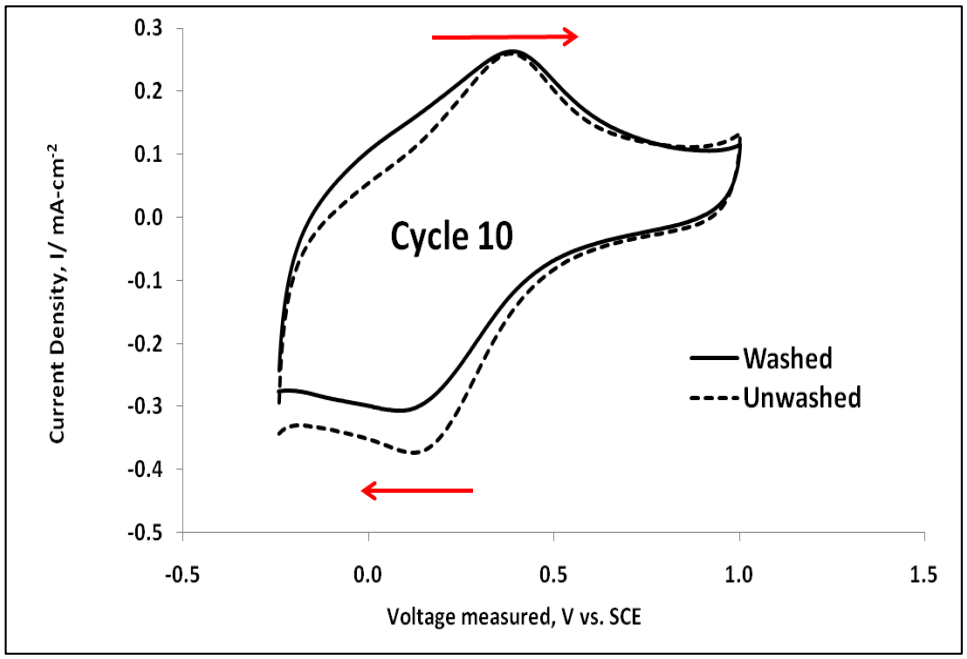

Figure 15 A comparison of respective cycles from the washed and unwashed cyclic voltammetry experiment (Cycle 10).

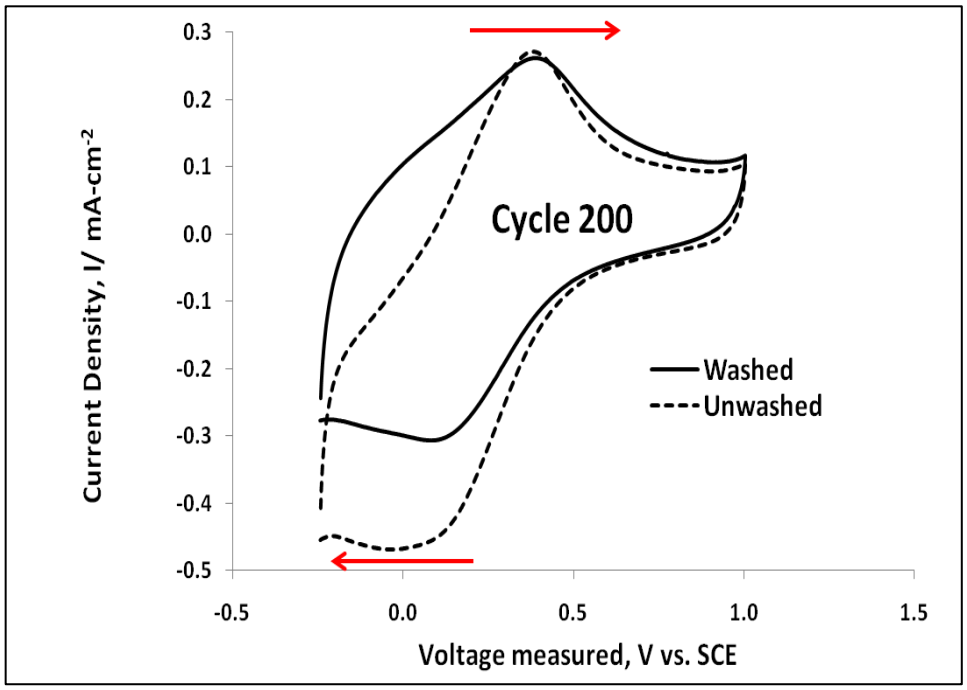

Figure 16 A comparison of respective cycles from the washed and unwashed cyclic voltammetry experiment (Cycle 200).

Prior to each experiment, the electrolyte solution (1M $HClO_4$; Sigma Aldrich) was purged for 20 – 30 minutes with Argon gas to remove any lingering impurities. Electrolyte solution was changed for each experiment to ensure accuracy. CV scans were evaluated between the hydrogen (-0.244V versus SCE) and oxygen (1.005V versus SCE) reduction potentials. At least 200 scans were performed for each experiment; a point at which the scan profile was considered to have stabilized. Current density was determined by normalizing the collected current by the geometric surface area of the GCE.

3.3 Results & Discussion (~3nm Pt NPs)

TEM photographs obtained for the washed and unwashed batches of ~3nm Pt NPs demonstrated that the washing did not have an effect on the Pt particle size. It also revealed the clear presence of the capping agent material. A size distribution of the Pt nanoparticles was also evaluated from TEM images obtained of washed and unwashed Pt NPs. From each sample, 100 particles were sized using the Tecnai ImageJ software and the respective scale bars as a reference. [52]

The respective histograms associated with each Pt NP batch shows the size distribution associated with the Pt NP batches The average size of particles recorded in unwashed batches was 3.4 nm, while that in washed batches was 3.3 nm. These values confirm that the washing steps did not have a considerable impact on the Pt particle size.

From TPO experiments of washed and unwashed Pt particles using 10% oxygen in helium, the oxidation of PVP was observed. TPO experiments, show the corresponding oxidative processes observed for the washed and unwashed Pt particles, respectively.[52] Others have observed the decomposition of PVP under oxygen beginning at 100^oC [98], which can also be seen in both of these experiments. This observation is corroborated by the increased

abundance of CO_2 and H_2O - as expected - during oxidation in the unwashed particle batch. The abundance of H_2O continues to increase until 500^oC in both spectra. The CO_2 abundance in both graphs continues to rise until 400^oC and, later at about 600^oC the abundance rises again for a moment before declining for the rest of the experiment. The difference between the unwashed and the washed TPO experiments is highlighted by the amounts of CO_2 and H_2O, which come off the respective samples. Logically, the unwashed Pt particles batch experiment- with a significant amount of PVP – shows more prominent CO_2 and H_2O peaks while the washed Pt particles batch experiment, show no discernibly similar peaks, an indication that most, if not all of the PVP was effectively removed in that case. (figure 3, [52])

A summary of the electrochemistry results indicated that, for the concentration of the nanoparticle suspension used in both experiments, the profile of the CV scan became constant in the vicinity of 200 cycles. The CV scan corresponding to the washed particles, figure 14**,** shows little variability. On the other hand, the CV result from the unwashed particles in figure 13, showed an appreciable level of variability, particularly, in the region between the hydrogen reduction potential and the vicinity of the peak anodic current of the scan curve.

The differences between the two experiments are further noticed by comparing respective cycles from both experiments as shown in figure 15 and figure 16. This comparison highlights an increase in current density with scan number for the unwashed particle experiment. This trend was attributed to a charge transfer by the functional groups of PVP to the Pt surface, resulting in electron-rich Pt particles that contribute to higher current density curves. This model is in agreement with previous findings [97, 99, 100] that report on the charge transfer between PVP and metal surfaces as important phenomena in catalysis. Briefly, Borodko et al. elaborate on two

distinct mechanisms through which functional groups from the PVP can bind to a Pt (or Rh) surface.

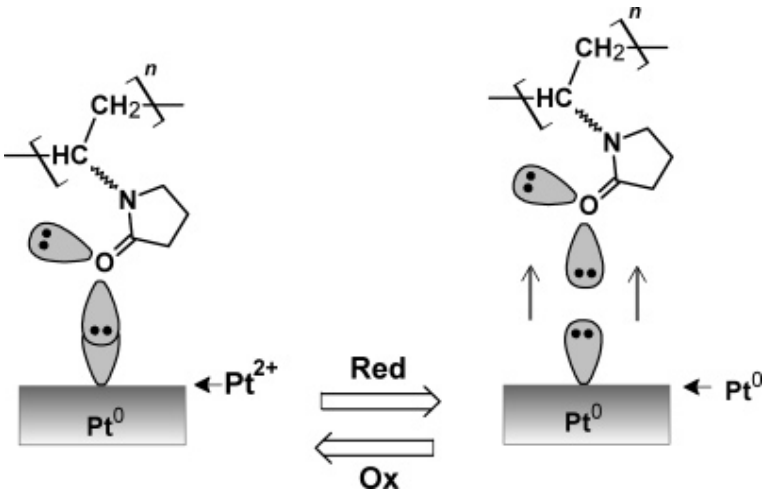

Figure 17 Model for the PVP/Pt Interaction in Reduced and Oxidized States ([2])

In the first instance, the carbonyl group was shown to bind to a Pt surface when in the oxidized state, i.e. surface (Pt^{2+}) species. The authors report on Pt^{2+} acting as a proton acceptor by virtue of their ability to attract carbonyl group lone pairs to the vacant d orbitals. The scenario was reversed for a reduced Pt surface species. Here, in the absence of vacant orbitals, the Pt surface repelled carbonyl group lone pairs. This is illustrated in scheme 3.4a. A second scenario reported a bidentate interaction of PVP with the Pt surface (scheme 3.4b). In addition to the carbonyl group, the Pt surface also accommodated lone pairs from the nitrogen atom in PVP.

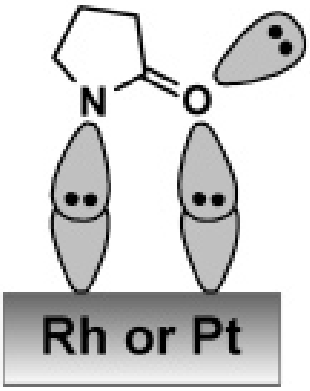

Figure 18 Pyrrolidone bonding to Pt surface as a bridging ligand (courtesy of Borodko et al. [2])

The resulting bond with PVP was much stronger and not as likely to break, as in the case of the monodentate ligand involving the lone pair from the carbonyl group exclusively. By virtue of its interaction with Pt, the PVP degrades much easier than it does in the pure state [101]. It is this decomposition process that promotes the availability of lone pairs which, then bind through monodentate and bidentate ligands to the Pt surface. The progression of the degradation process propels the availability of more lone pairs for interaction with the Pt surface until a saturation point when there are no more sites available for interaction. In the current work, which was the subject of one of our publications [50] we correlate the phenomena observed by Borodko et al. with discrete features of the cyclic voltammograms generated. Reduced Pt species are generated during the forward (oxidation) half of the cycle. As oxygen evolves and the potential is subsequently switched to reduction, the binding of functional groups from the decomposing PVP begins. Equations 9 – 16 illustrate the progression and cycling for the generation of different species during the cyclic voltammogram as a function of sweep voltage. The manifestation of the increased current density owing the binding of PVP with the Pt surface is most evident in the

HOR of the reductive half of the cycle where the differences in current density are most evident (see figure 13 & 16). Borodko et al's evidence suggests that such dramatic increases in the current density are not likely to be as evident, like the CVs in this work demonstrate, during the oxidative process where the Pt species is being converted to Pt^{2+}.

Oxidative half of cycle

$$Pt(s) \rightarrow Pt\text{-}H + e^- \quad (9)$$

$$Pt\text{-}H \rightarrow Pt\text{-}OH \quad (10)$$

$$Pt\text{-}OH \rightarrow Pt\text{-}O \quad (11)$$

$$Pt\text{-}O \rightarrow Pt^{2+} + O_{2\,(g)} \quad (12)$$

Reductive half of cycle

$$O_2\,(g) + Pt^{2+} \rightarrow Pt\text{-}O \quad (13)$$

$$Pt\text{-}O \rightarrow Pt\text{-}OH \quad (14)$$

$$Pt\text{-}OH \rightarrow Pt\text{-}H \quad (15)$$

$$Pt\text{-}H + e^- \rightarrow Pt(s) + H_2(g) \quad (16)$$

While the number of CVs run for each experiment was restricted to 200 in number, preliminary work involved running many more cycles. However, saturation in the measured current density was observed in the vicinity of 200 cycles. Indeed, visual inspection of figures 13 and figure 14 will reveal that the difference between cycle 150 and cycle 200 is minimally discernible. This same point of saturation was also arrived at during thermal degradation experiments by Borodko et al. [101] of PVP on Rh and Pt NPs. Beyond the saturation of

available sites, the explanation for this phenomenon has also been attributed to observed interactions featuring capped metallic NPs with monodentate e.g. (C=O**:)** and bidentate e.g. (C=O**: /** C_2N**:**) ligand species which are chemisorbed on the metal surface [102].

3.4 Conclusions

It was observed that CV scans with PVP capped Pt NPs resulted in higher current density measurements. This observation suggests that in addition to the corrosion resistant properties that PVP can provide for sub-10nm NPs, the incorporation of PVP may in fact improve the performance of low temperature PEMFCs. The observations made in this work suggest that the presence of PVP in platinum nanoparticle syntheses may improve Pt nanoparticle stability and, by inference, their electrocatalytic activity after many electrocatalytic cycles. A model based on the strong interactions between the surface of the Pt particles and the monodentate and bidentate ligand groups is proposed. As a result, it is anticipated that the incorporation of PVP, and possibly other capping agents, may in fact lead to improved PEMFC performance through enhanced stability under application conditions, which could accelerate the commercial availability of PEMFCs.

CHAPTER 4: PALLADIUM MONOMETALLIC SHAPE EFFECTS

4.1 Introduction

Major factors limiting the mass implementation of Proton Exchange Membrane Fuel Cells (PEMFCs) include the elucidation of a cheap yet effective catalyst to replace platinum supported on carbon [103-105] and the ability to safely store hydrogen "on-board" automobiles, which incorporate PEMFCs. Interestingly, these are two properties of Pd that have made it a keen material of interest for PEMFCs

By virtue of its periodic proximity as well as many computational metallic surface studies,[31, 106] Pd has been shown to be an ideal material for incorporation in PEMFCs. Furthermore, currently at a fraction of the price of Pt, it also presents itself as a commercially viable option for commercial scale implementation. A significant body of literature has been dedicated to reducing the amount of Pt used in PEMFCs by combining Pt with other materials or modifying its support to improve performance. A newer and growing body of literature however seeks to replace Pt altogether and, through advances in synthetic chemistry, tailor the properties of new NPs to improve electrocatalytic activity. The progress of this work has been guided through advances in theoretical studies, particularly DFT [107-109], which have been essential in proposing surfaces that may show improved catalytic activity for a given reaction pathway. Of particular interest, is the work of Norkov et. al [110] which highlights the similarity in activity towards the oxygen reduction reaction on the (111) surface for Pt and Pd surfaces relative to other transition metal surfaces that were studied as well. A ranking consisting of the activity of

the different metal surfaces as a function of their oxygen binding energy was made. Metals closest to the peak of the volcano had the best activities, which were characterized by an ideal balance between the materials propensity to react and / or remain inert. In another study, Markovic et al. [111] also showed that, at least for a monometallic Pt surface the ORR activity varied in the order; (110) > (100) > (111). This trend suggests that more kinetically controlled morphologies of NPs would tend towards better electrocatalytic activity than their thermodynamically driven variants. Recent synthetic chemistry efforts have shown that it is possible to generate a number of innovative morphologies based on monometallic or bimetallic compositions by controlling different kinetic factors. The resulting shapes, tailored to feature one or more sets of lattice planes over the other, would then reveal activity trends that promote a given reaction based on the extent to which the enclosed lattice facets tend to facilitate that reaction. The paper by Lim et al. [43] in *Science* is a great example which takes advantage of the bimetallic properties of a relatively new shape – PdPt dendrites - and illustrates how they demonstrate enhanced ORR activity. In this work, we explored the effect of isolating monometallic Pd dendrite properties and compared them with those from Pd cubes using an aqueous synthesis technique described in chapter two. The electrocatalytic properties of the two shapes were also studied and are presented in this chapter. Trends observed between the interaction of hydrogen and the Pd surface during cyclic voltammetry experiments led us to compliment electrocatalysis with traditional catalytic experiments as well based on Pd's inherent H_2-storage properties.

Similar to other precious metals, Pd can absorb hydrogen. However, the absorption capacity of Pd exceeds that of other materials. [112] In fact, Pd is known to absorb up to at least 600 times its volume in hydrogen and this property has made it a model system for hydrogen

storage studies. [112, 113] After dissociation of the hydrogen molecule to hydrogen atoms, the Pd lattice becomes permeable to a fraction of the said ions, which then preferentially lodge within the octahedral sites of the Pd metal sub-surface. [114] The present work highlights the impact of monometallic Pd nanoparticle morphology, which can lead to enhanced hydrogen storage properties, and is a novel contribution to the hydrogen storage field. In this contribution, an enhanced ability to store hydrogen is demonstrated for Pd nanocubes over polycrystalline Pd dendrites and the differences are discussed through results from a series of characterization and testing techniques. Ethylene hydrogenation, a structure insensitive reaction,[89, 114-119] indicated a higher external surface of the dendrites, as compared to the cubes, which agreed with the expectations for the structures from TEM imaging. Cyclic voltammetry, as well as static hydrogen sorption experiments, showed that Pd nanocubes exhibited better hydrogen sorption capacity than Pd dendrite nanoparticles of the same size. This observation was attributed to the facile formation of PdH phases for the Pd nanocubes due to its more open crystal surface structure as compared to the Pd dendrites. It is postulated that adsorbed hydrogen atoms on the Pd surface lodge into the octahedral sites and this rate is proportional to the atomic spacing of the surface plane. The morphology of the nanocubes enhances the interstitial diffusion into the Pd lattice and, consequently, lattice expansion, which combined are proposed as the source of the hydrogen storage enhancement for the (100)-rich nanocubes as compared to the polycrystalline dendrites.

4.2 Electrochemistry Experiments

Samples were prepared by making subsequent aliquot depositions of the Pd suspension on the GCE. The nature of the suspension required each aliquot to be dry before a subsequent one was added to ensure that all material was deposited on the GCE amorphous surface.

Furthermore, a drop of Nafion® 117 solution, deposited on the dried Pd-nanoparticle film acted as a binding agent as well as a proton conduction facilitator.

4.2.1 Cyclic Voltammetry

Prior to each experiment, the electrolyte solution 100mL of 0.1M $HClO_4$ (Sigma Aldrich) was purged for 30 minutes with Argon gas to remove gaseous impurities. After 30 minutes, the modified working electrode was lowered into the electrochemical cell. Cleaning cycles were run between (-0.244V vs. SCE) and (0.356V vs. SCE) for 20 cycles at $100mVs^{-1}$ under Ar. This was followed by a series of 10 cycles at $20mVs^{-1}$ cycled between (-0.244V vs. SCE) and (0.956V vs. SCE) to generate a preliminary estimation of the ECSA. After the CV experiment and still under Ar, an ORR curve was recorded at 3600rpm and $10mVs^{-1}$ before switching the gas flow to O_2.

4.2.2 Oxygen Reduction Reaction

ORR experiments consisted of voltage sweeps from (0.956 vs. SCE) to (-0.244 vs. SCE) at $10mVs^{-1.}$ Sweep experiments were started after flowing O_2 for at least 30 minutes. A series of six different ORR curves were recorded at 100, 400, 900, 1600, 2500 and 3600rpm respectively ORR. In order to account for the capacitive current due to the electrolyte, the background sweep scan was subtracted from each of the ORR curves to elucidate the ORR curve that was attributed to the modified working electrode exclusively. CV and ORR and data were normalized by the geometric surface area of the GCE and the resulting current density was reported as a function of the sweep voltage.

4.3 Catalyst Studies

For samples prepared for H_2-sorption and ethylene hydrogenation, enough silica (Cab-O-Sil; Sigma-Aldrich) was added to the total suspension of Pd nanoparticles to achieve a 1 wt. % silica-supported Pd (Pd/SiO_2) system. The resulting materials were then dried before use. A

similar procedure was used for the samples prepared for X-ray absorption except that the Pd loading was 2%.

4.3.1 Ethylene Hydrogenation

Ethylene hydrogenation experiments were performed on 1% Pd/SiO_2 dendrites and cubes using an in-house reactor system consisting of 8 mass flow controllers (Alicat) connected to a Perkin Elmer AutoSystem Gas Chromatograph for gas analysis. The powder material (~8 mg) was pre-treated in helium at 50sccm and subsequently reduced in 10 $\%H_2$/He (50 sccm) by ramping-up the temperature to 150^{o}C at a rate of 10^{o}C/min with a 30-minute holding period. The system was allowed to stabilize and the temperature of the reactor cooled to below 45^{o}C. At this point, the feed gas composition was modified to include ethylene for a final gas composition of 50 sccm He: 25sccm H_2: 2.5sccm C_2H_4. Additionally, the temperature of the reactor was slowly ramped up at 0.8°C/min to record chromatograms at different temperatures between 50°C and 75°C

4.3.2 H_2 Sorption

Using Quantachrome's Autosorb iQ, sorption isotherms were recorded for 1% silica-supported Pd nanocubes and dendrites. Approximately 750 mg of each material was trapped in a sorption cell using glass wool (Ohio Valley Specialty Company). Each sample was purged in helium at 120°C and subsequently reduced in hydrogen as the temperature was ramped up to 250°C at 20°/min and held for two hours. Then, the cell was evacuated of gas and force cooled to 40°C. At this point the pre-treatment was complete and the analysis was performed using Hydrogen as analysis gas at 40mmHg intervals between pressures of 240 mm Hg and 560 mm Hg.

4.3.3 X-RAY Absorption Spectroscopy

X-ray absorption spectroscopy (XAS) studies were performed at the DuPont-Northwestern-Dow (DND) Collaborative Access Team (CAT) beamline 5-BM-D (BM = bending magnet, http://www.dnd.aps.anl.gov/) at the Advanced Photon Source of Argonne National Laboratory. For these experiments, the storage ring energy and circulating current were 7.0 GeV and 100.6 mA, respectively. X-rays were selected using a Si(111) monochromator. For acquisition of the XAS data, catalyst powders (a mass ~ 50 mg) were finely ground and pressed onto 13 mm diameter pellets using a Carver press operated at 12,500 psi for 20 s. Pellet thicknesses were adjusted to obtain a linear absorption coefficient near 1. Spectra were collected in transmission mode at the Pd K absorption edge (24350 eV) under ambient conditions. Energies were scanned from 150 eV before to 30 eV before the edge in 10 eV steps (background region) and then to 975 eV (representing k = 16 $Å^{-1}$) after the edge in 2 eV steps (pre-edge/edge region). The absorption was measured using ionization chambers before and after the sample. Following the second ionization chamber, the Pd foil and a third ionization chamber were positioned to monitor this reference examined simultaneously. Multiple scans (typically 3 per sample) were obtained to improve the signal-to-noise ratio. Merging of individual scans and data reduction were performed with the Athena software package [120, 121] . The background region (-150 to -50 eV before the edge) was extrapolated and subtracted from the data. Edge energies were selected as energy yielding the maximum absorption derivative. Spectra were normalized with a polynomial spleen operation by the absorption over the Δk range of 2 to 14 $Å^{-1}$. Finally, the spectra were Fourier transformed with a Hanning window from k-space into R-space over the Δk range of 3 to 14 $Å^{-1}$. The data range in k-space was Δk of 3 to 14 $Å^{-1}$ for the Fourier Transform in R-space. Fittings were performed in R-space over ΔR of 1 to 3.5 Å (for 17

independent points) using k-weights of 1, 2, and 3. The Pd-Pd path was used for phase corrections. Coordination numbers (CN), interatomic distances between an absorber and backscatter pair (R), mean-square displacements in the distribution of interatomic distances (σ^2), amplitude reduction factors (σ_o^2), and inner potential corrections (ΔE_o), were the parameters determined from modeling the EXAFS data. Coordination numbers were determined by approximating the amplitude reduction factor of the catalyst samples to those obtained by the reference materials. Only fits with reasonable values for ΔE_o (less than ~|10 eV|) and σ^2 (less than ~0.02 $Å^2$) were considered. Coordination numbers were optimized to obtain an amplitude reduction factor (σ_o^2) similar as to the values obtained above for the specific absorber-backscatter pairs in reference materials. Uncertainty in coordination numbers were 0.2 for Pd-Pd spacings. R-factors less than ~2%, as obtained for the reference materials, were generally used to signify a good fit.

4.4 Results and Discussion

4.4.1 Synthesis

As can be seen in figure 5 and 6 (Chapter 2), Pd cubes and dendrites were synthesized using the same set of ingredients. The difference between the two batches of nanoparticles was the order in which the surfactant material (CTAB) and the reductant material (L-Ascorbic Acid) were added to the reactor vessel. An initial interaction occurs between the Bromide ion from CTAB and the Palladium ion from K_2PdCl_4 to form the $PdBr_4^2$ complex which is more stable than $PdCl_4^{2-}$. Additionally, this bromide complex preferentially prompts formation along the (111) and (100) facets, which result in the cubes recorded upon addition of the reductant, L-Ascorbic Acid. In contrast, by switching the reagent addition sequence, the absence of the templating and strongly binding bromide, resulted in faster nucleation and growth kinetics which

was then halted by the addition of the stabilizing agent, i.e. CTAB. The result of this was the formation of Pd dendrites. The last two ingredients were added within ten seconds of each other, ensuring uniform and homogeneous NPs according to the La Mer model [80]. Still preliminary syntheses resulted in larger dendrites than cubes. To address the size difference, the concentration of Pd precursor was divided into two batches (unlike for the cubic synthesis sequence) and this modification would result in dendrite sizes that were close in size to those of Pd cubes.

Pd NP size determination was done via visual inspection coupled with Image J ® confirmed with the Full Width Half Max (FWHM) estimation of the nanoparticle sizes, from XRD patterns, which suggested a similarity in size notwithstanding shape. (figure 19). Average Pd NP size distribution was between 20 and 30 with average crystallite sizes for Pd cubes and dendrites recorded as 24.7 nm and 21.1nm respectively.

The observations made here, were also confirmed via X-Ray absorption (XAS) experiments. Results (figure 20) revealed similar interatomic bond distance measurements as well as coordination numbers, which are both consistent with typical values reported for Pd. [120, 121] Furthermore, the matching XANES patterns highlight the similarity in oxidation state and size that exists between both shapes, which is also observed. Furthermore, the matching XANES patterns highlight the similarity in oxidation state and size that exists between both shapes, which is also observed.

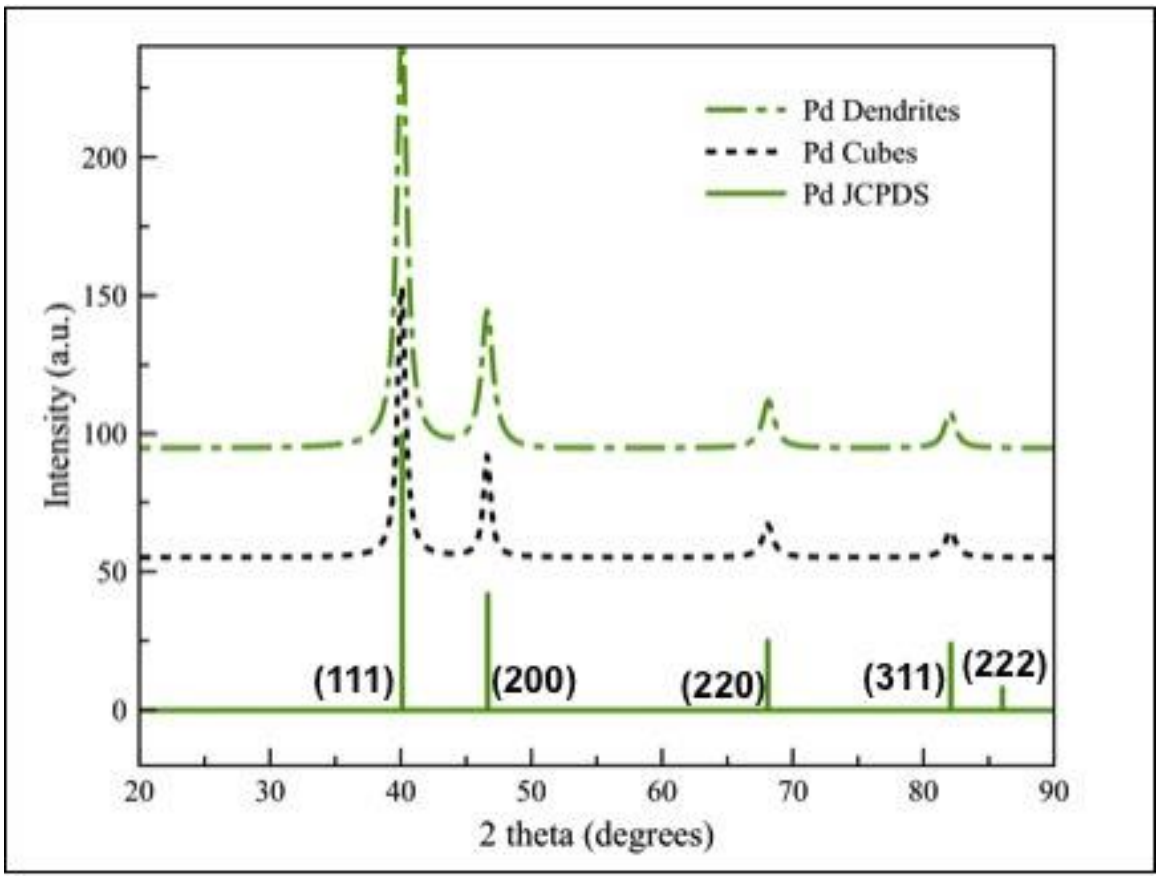

Figure 19 X-Ray Diffraction patterns for Palladium cubes and dendrites compared to JCPDS reference.

4.4.2 Cyclic Voltammetry

A comparison between the Pd cubes and Pd dendrites was obtained by comparing ECSA and stability trends. It was observed that despite running cycles aimed at cleaning the modified WE surface prior to each experiment, the defining features of the CV curves did not become uncompromisingly evident until after at least an hour of continuous running. For this reason, ECSA values were estimated by comparing the integrated value of the hydrogen evolution peak with that of the palladium oxide peak, both on the cathodic sweep of the cyclic voltammogram. Pd cubes consistently exhibited higher ECSA values than Pd dendrites. This was despite the additional apparent surface area that the Pd dendrites presented by virtue of the flower petal-like

fringes on the periphery of the Pd dendrites. After 3.5 hours of continuous cycling, the Pd cubes demonstrated a 50% higher value than the dendrites. This trend was consistent with every subsequent pair of cube and dendrite batches that was evaluated simultaneously. The observed trend was attributed to the Pd-H interaction, which seems to vary as a function of the Pd NP shape. This observation was further examined with an evaluation of the ECSA loss as a function of time (or cycle number). It was determined that in the evaluation of the ECSA in the HOR, the ECSA increased within the first 90 minutes of cycling.

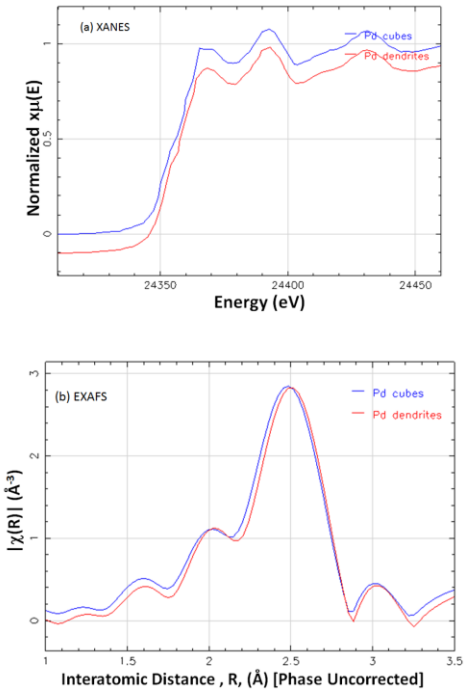

Figure 20 X-ray absorption, the (a) XANES and (b) EXAFS regions, of Pd particles supported on carbon.

Table 3 EXAFS Fittings of the shape controlled Pd particles deposited onto silica (2wt% Pd)

Material	Absorber-backscatter pair	CN	R(Å)	σ^2 (Å^2)	ΔEo (eV)	R factor (%)
Pd cubes/silica	Pd-Pd	10.7	2.738	0.0056	-6.10	0.6
Pd dendrites/silica	Pd-Pd	10.6	2.739	0.0055	-3.60	0.5

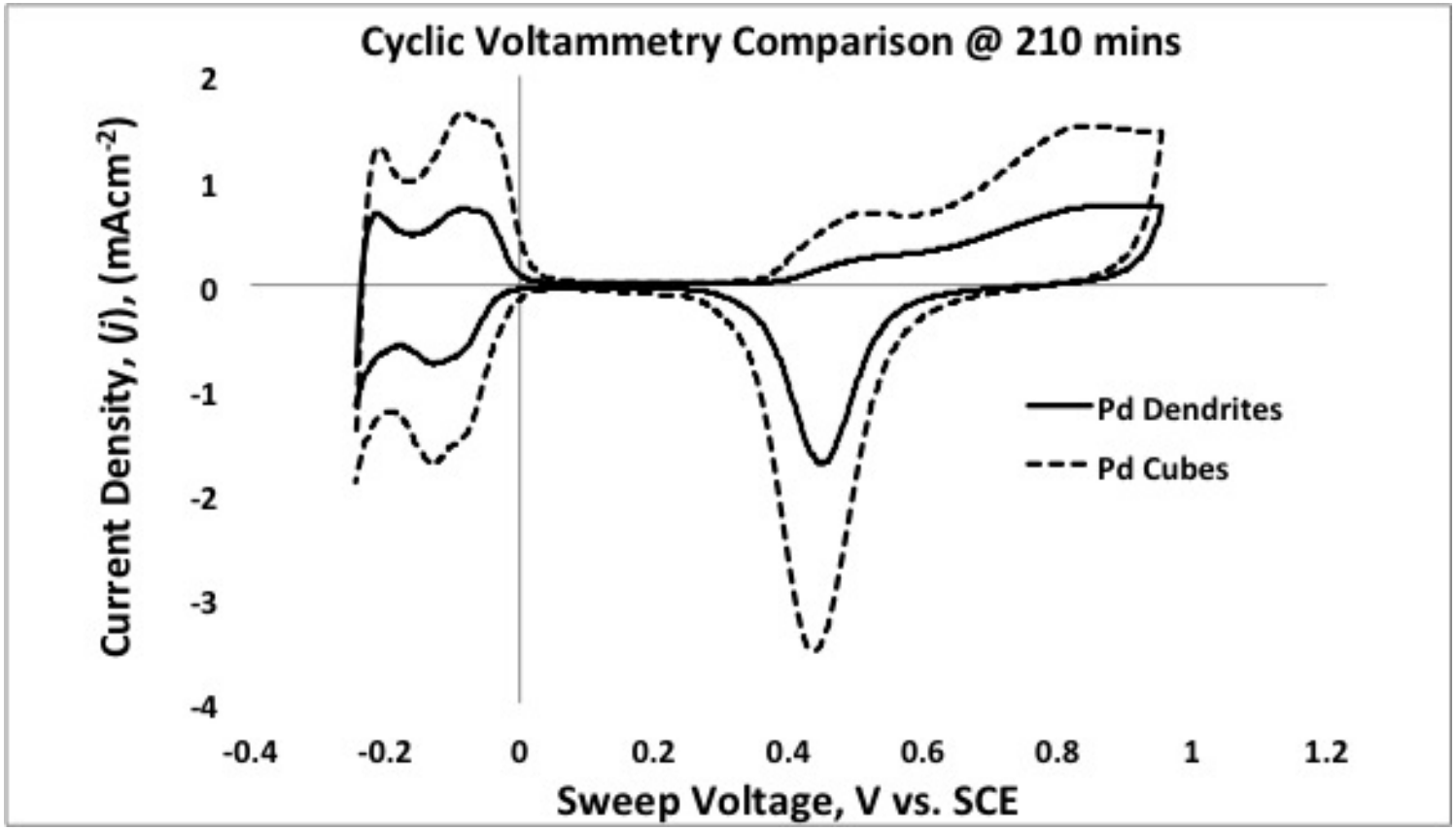

Figure 21 Comparison of typical cyclic voltammograms corresponding to Pd nanocubes and dendrites. CVs were recorded at 1600 rpm and a scan rate of 20mV/s after 210 minutes of continuous cycling.

Subsequently, the ECSA followed a linear decrease in value over time. This finding presents credible reasons to question the accuracy of HOR ECSA use as a means of determining ECSA values and has become a point of recent inquiry. [122] In figures 22 and 24 we compare the integrated values of the HOR and oxide peaks. We also compare the evaluated ECSA for two batches of experiments in each case. The evaluated ECSA values for both experiments were within a 5% margin of error from each other while the Pd dendrites were within a 10% margin of error of each other. While like most ORR electrocatalysts, our Pd nanocubes and dendrites were physically immobilized and as such an ability to transfer the same amount of material to the GCE was critical to accuracy. Furthermore the larger margin of error is explained by the fact that dendrites, which manifested twinning, had to be generated in smaller batches still, and subsequently combined to generate the desired size range and minimize twinning.

The results we observe suggest that the interaction between Pd and H, even in electrochemical environments is credible enough to warrant study and, in the latter part of this chapter, our efforts in that regard are discussed. Furthermore it brings to light the potential of the oxide peak to serve as a more accurate means of measuring ECSA than the HOR especially since the nature of the Pd – O interaction is limited to the Pd metal surface and not the sub-surface.

4.4.3 Oxygen Reduction Reaction

An essential component of electrocatalytic studies is the elucidation of the preferred pathway that the oxygen reduction reaction process adopts. This would inform the use of either the RDE or the RRDE (shown in scheme 2.2a), which employ a 4-electron mechanism or a 2-electron mechanism respectively.

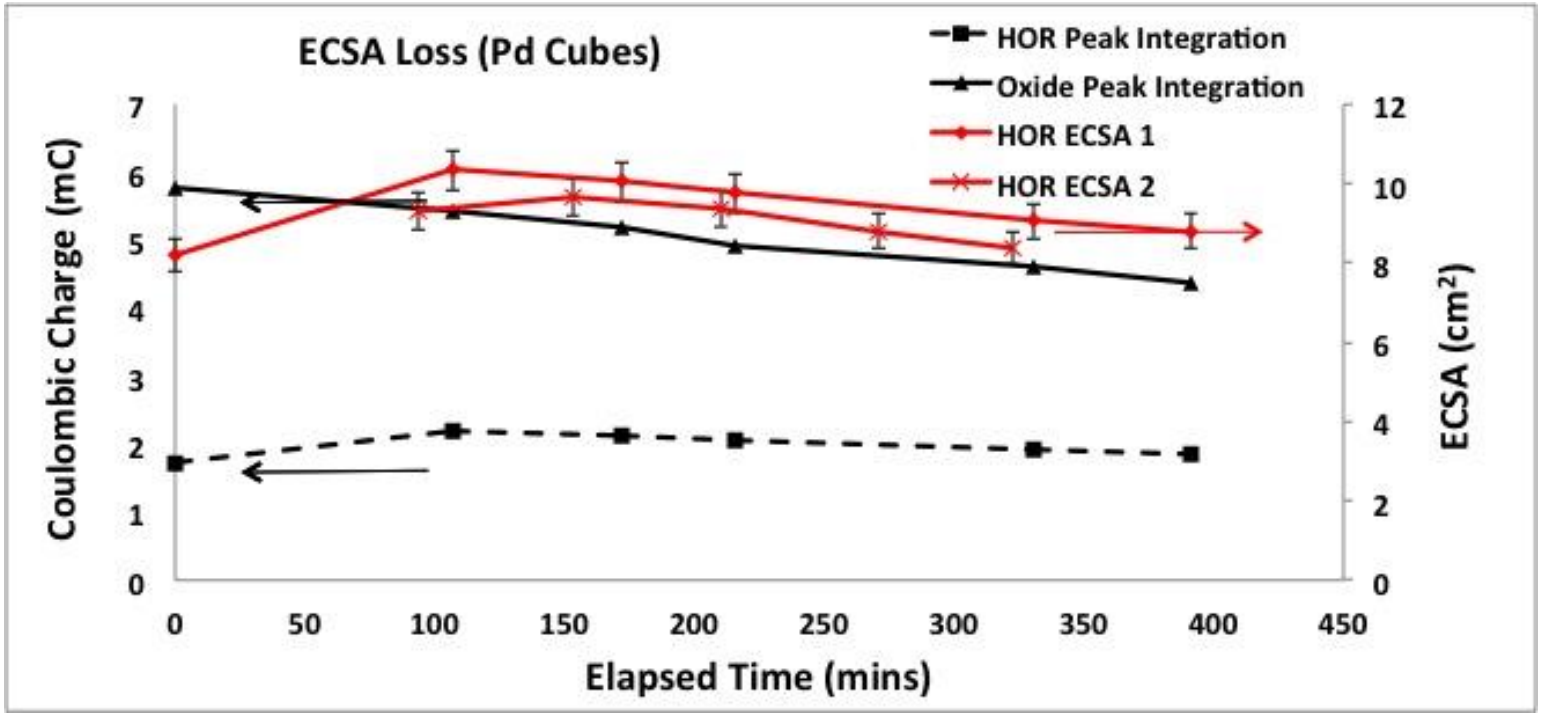

Figure 22 In red: Comparison of two batches of Pd Cube syntheses reproduced to within 5% of each other; black dashed: integrated value of the PdO peak on the cathodic sweep of the voltammogram; solid black: integrated HOR peak

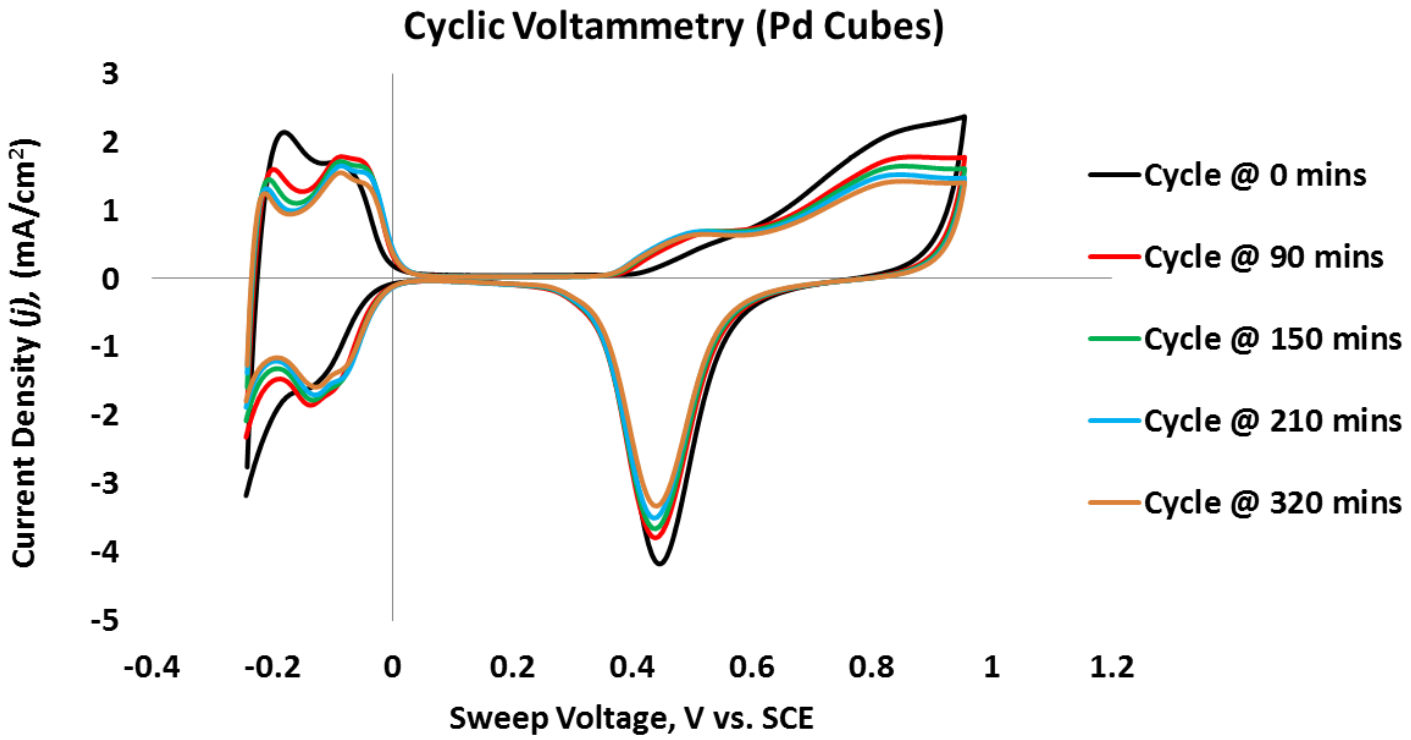

Figure 23 A visual depiction of the reduction in the current density as a function of surface area for Pd cubes over time (cycle number). CVs were recorded at 10mV/s and a 2mV step size.

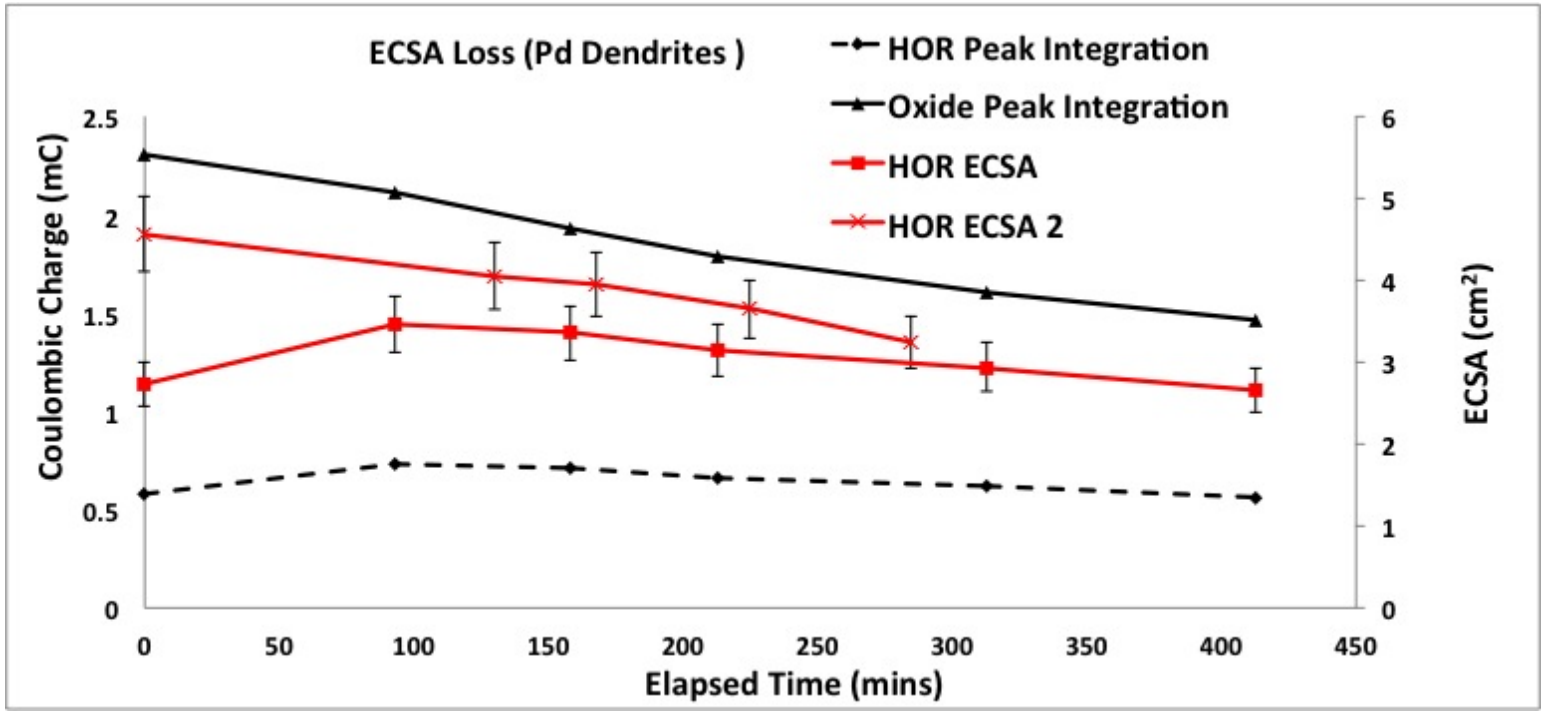

Figure 24 In red: Comparison of two batches of Pd dendrites syntheses reproduced to within 10% of each other;
black dashed: integrated value of the PdO peak on the cathodic sweep of the voltammogram; solid black: integrated HOR peak

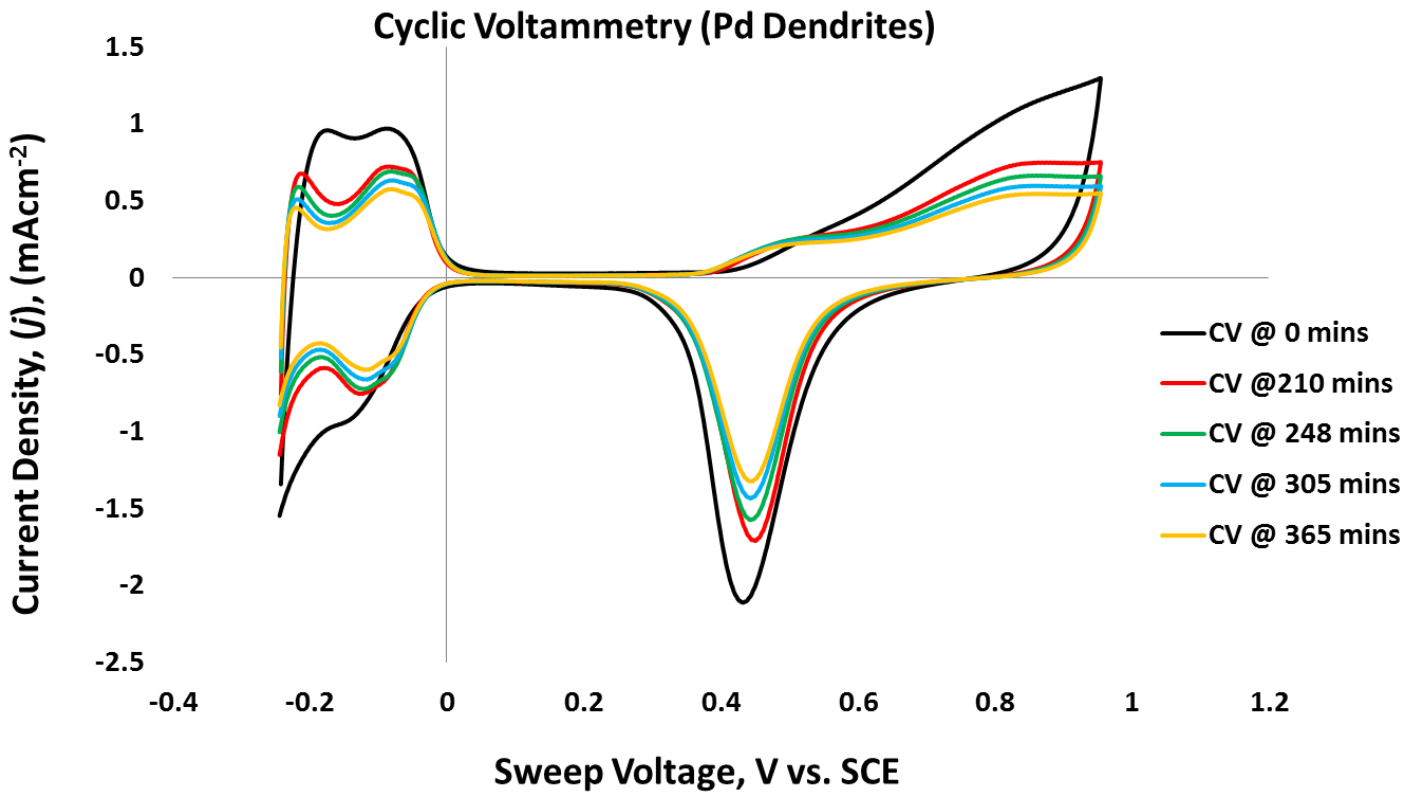

Figure 25 A visual depiction of the reduction in the current density as a function of surface area for Pd dendrites over time (cycle number). CVs were recorded at 10mV/s and a 2mV step size.

A series of linear sweep experiment batches were performed with the different modified WEs as shown in figures 26 and 28. From this information, Koutecky-Levich plots were also generated for each respective series of ORR curves. Typical ORR results are shown in figures 26 and 28 and their corresponding Koutecky-Levich plots are shown in figures 27 and 29. It will be noted that ORR curves obtained at lower rotation speeds have a propensity to introduce more noise, since the dynamic nature of the electrochemical reactor becomes accentuated and so, where appropriate, were omitted.

The Koutecky-Levich plots were generated using a series of six different potential values varying from 0.05 to 0.30 in increments of 0.05. The inverse of the limiting current (iL^{-1}), obtained at these potential values was plotted as a function of the inverse square root of the rotation speed ($\omega^{-0.5}$) to obtain the series of linear plots shown in figures 27 and 29. From the slope of the Koutecky-Levich plots, equal to the constant *B* detailed in equations (5) and (6) from chapter two, the number of electrons participating in the reduction of oxygen can be determined. Averaged over the six voltages reported, *n* values for the cubes and dendrites were 3.69 ± 0.17 and 4.32 ± 0.67 electrons respectively. These results suggest that the oxygen reduction process for the Pd cubes and dendrites is overwhelmingly driven by the 4 –electron pathway or the direct reduction of O_2 to H_2O as indicated by equation (1) in chapter two. However, the four-electron pathway was favored by the dendrites more so than the cubes as evidenced by a higher average n value. In general, the more the potential tended towards a higher positive value, the more it tended towards the four-electron pathway for oxygen reduction and the more it tended towards negative potential values, the more it tended towards the two electron pathway.

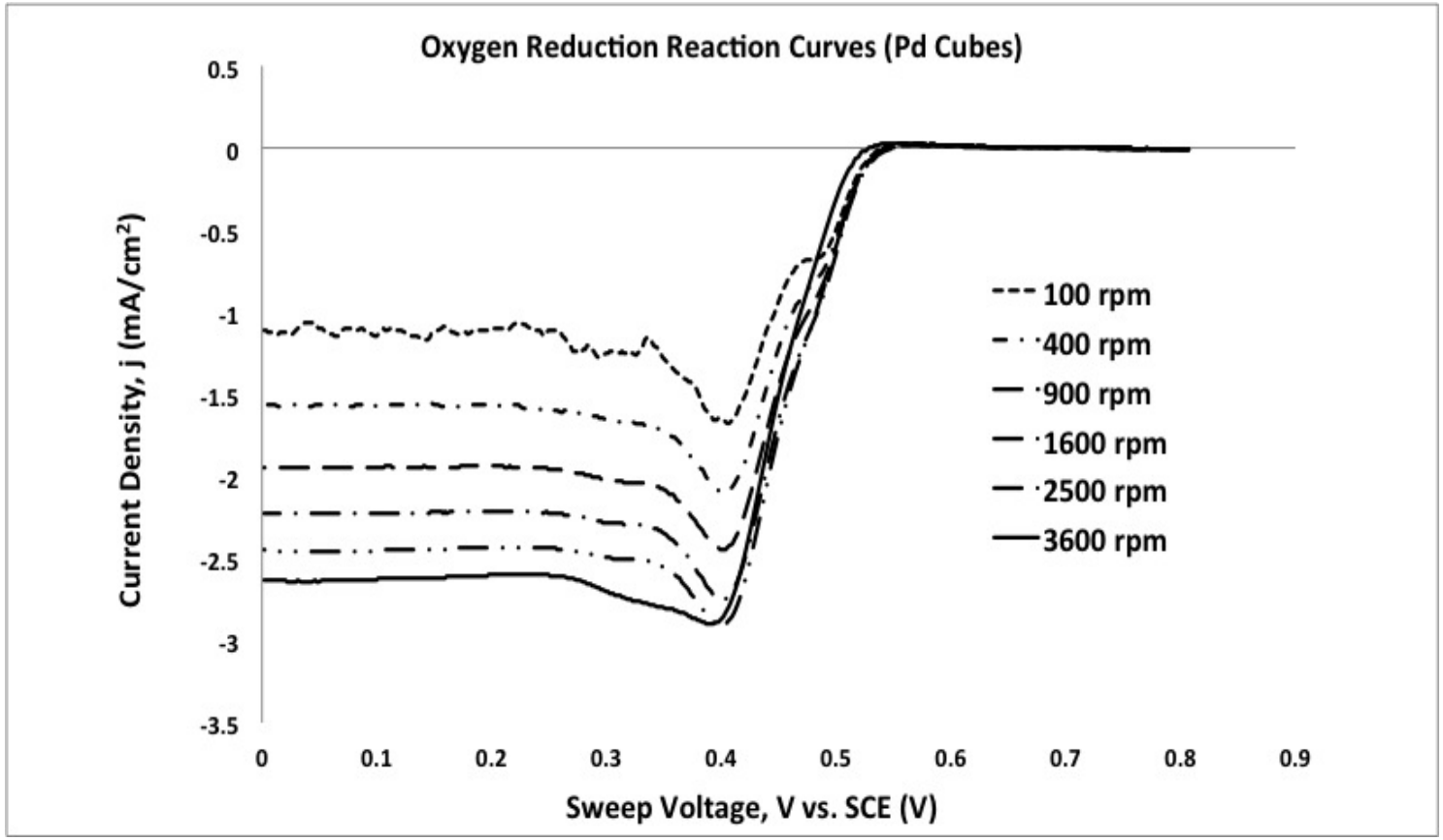

Figure 26 Oxygen Reduction Reaction curves obtained for Palladium nanocubes at different rotation speeds. The scans were recorded at a scan rate of 10mV/s and a step size of 2mV.

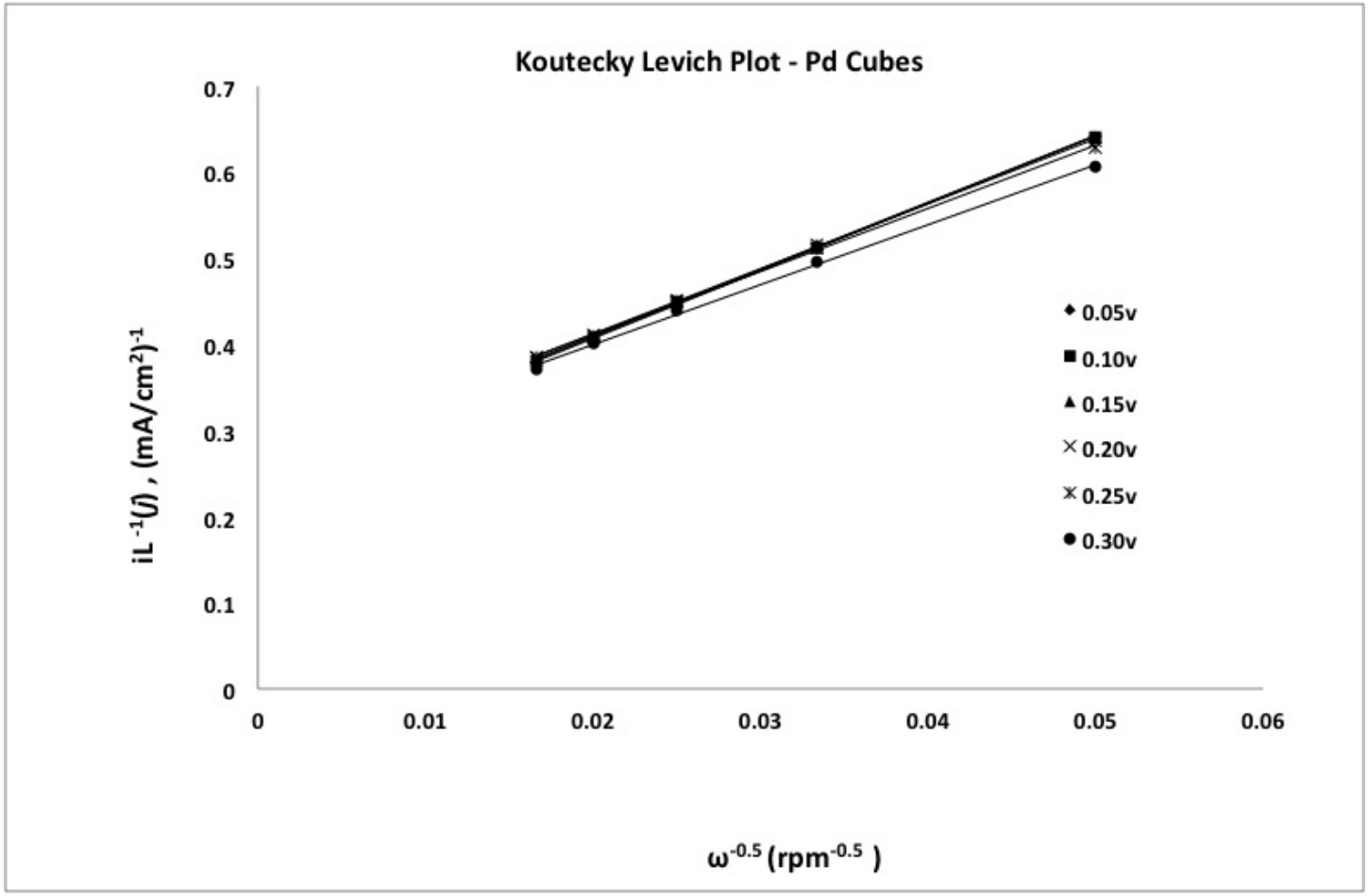

Figure 27 Koutecky-Levich plot corresponding to the series of ORR curves in 4.4a.

Table 4 Summary of Koutecky-Levich Parameters (Pd Cubes)

Pd Cubes		**$iL^{-1}(V)$, ($mAcm^{-2}$)**					
ω, rpm	**$1/\omega^{0.5}$**	**0.05v**	**0.10v**	**0.15v**	**0.20v**	**0.25v**	**0.30v**
100	0.1	0.92	0.87	0.88	0.91	0.90	0.79
400	0.05	0.64	0.64	0.64	0.64	0.63	0.61
900	0.03	0.51	0.51	0.52	0.52	0.51	0.50
1600	0.025	0.45	0.45	0.45	0.45	0.45	0.44
2500	0.02	0.41	0.41	0.41	0.41	0.41	0.40
3600	0.017	0.38	0.38	0.38	0.38	0.38	0.37
No. of electrons, *n*		**3.54**	**3.57**	**3.58**	**3.68**	**3.79**	**3.99**

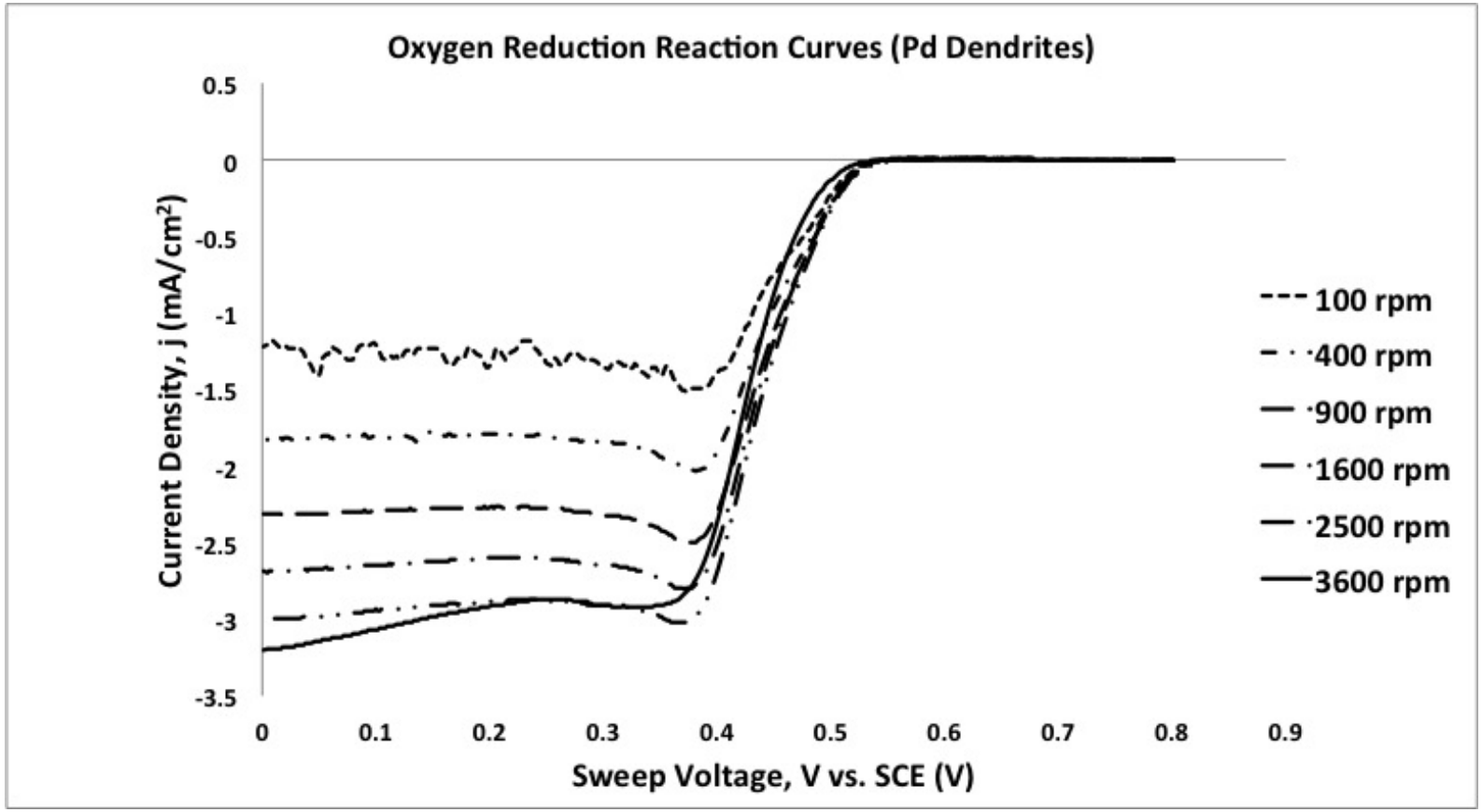

Figure 28 Oxygen Reduction Reaction curves obtained for Palladium nanodendrites at different rotation speeds. The scans were recorded at a scan rate of 10mV/s and a step size of 2mV.

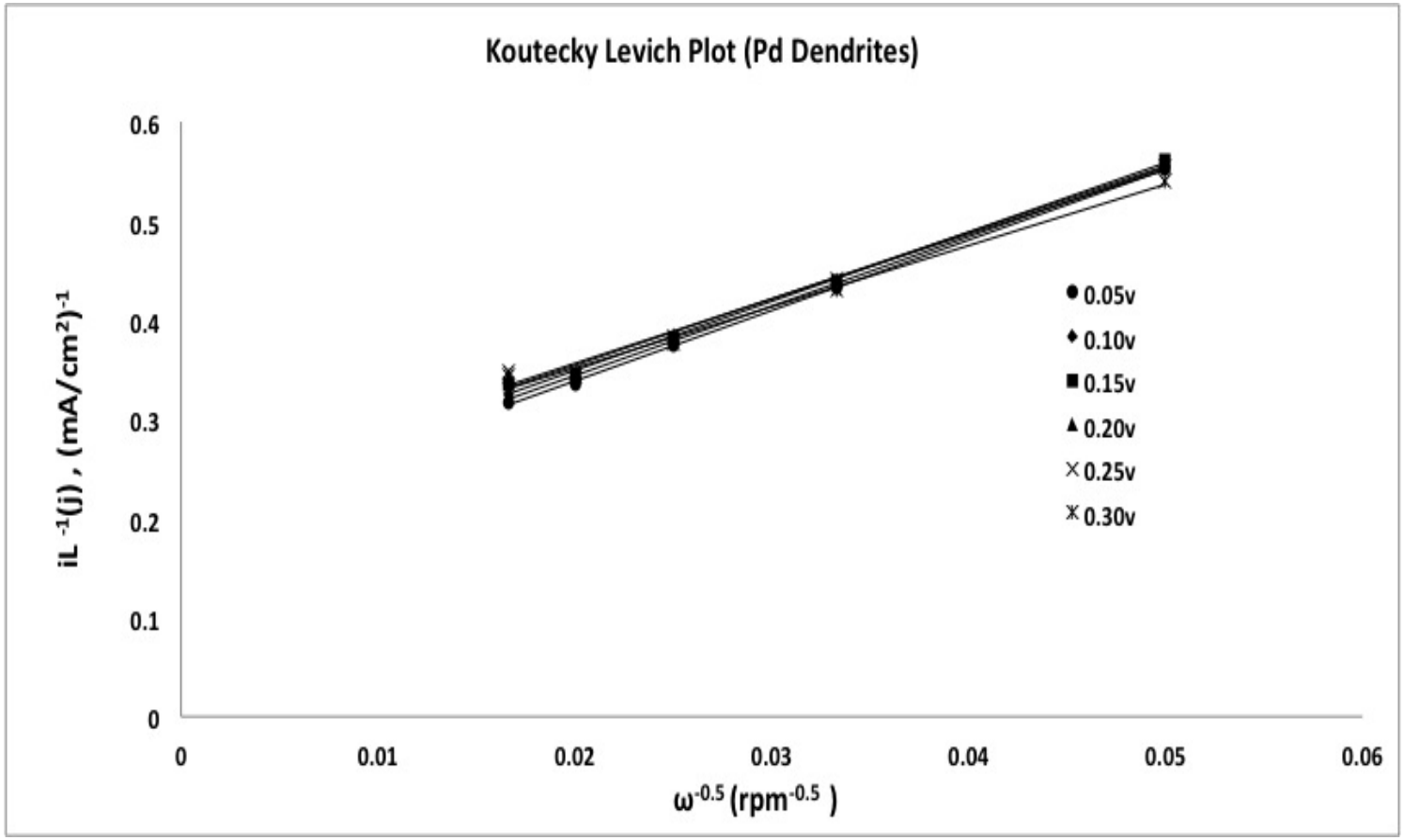

Figure 29 Koutecky-Levich plot corresponding to the series of ORR curves in 4.4c.

Table 5 Summary of typical Koutecky-Levich Parameters (Pd Dendrites)

Pd Dendrites		**$iL^{-1}(V)$, ($mAcm^{-2}$)**					
ω, rpm	**$1/\omega^{0.5}$**	**0.05v**	**0.10v**	**0.15v**	**0.20v**	**0.25v**	**0.30v**
100	0.1	0.86	0.83	0.81	0.74	0.76	0.74
400	0.05	0.55	0.56	0.56	0.56	0.56	0.54
900	0.033	0.43	0.44	0.44	0.44	0.44	0.43
1600	0.025	0.37	0.38	0.38	0.38	0.38	0.38
2500	0.02	0.34	0.34	0.34	0.35	0.35	0.34
3600	0.017	0.32	0.33	0.33	0.34	0.35	0.34
No. of electrons, *n*		**3.90**	**3.96**	**3.97**	**4.14**	**4.26**	**5.66**

Thus, it is presumed from this information that the two-electron and four-electron pathways are in fact present but with the latter dominating over the former.

A typical comparison of the activity as a function of the NP revealed a very small difference between the onset potential of the different shapes of Pd NPs as shown in figure 4.5. The mass activity of the Pd NPs was compared at 0.5V. The comparison showed that the cubes had a mass activity of 0.663mAcm^{-2} compared to a mass activity of 0.306mAcm^{-2} for the Pd dendrites at the same potential. The Pd cubes and dendrites displayed similar onset potentials at 0.54V (0.784 vs. SHE). Mass activities differed by 10mV at the $E_{0.5}$ point of the mixed kinetic-diffusion portion of the curve. This result agrees with CV results, which showed Pd cubes had a higher ECSA, which in turn facilitates the easier reduction of oxygen easier, i.e. at a higher onset potential.

4.4.4 Ethylene Hydrogenation & H_2 Sorption Studies

For ethylene hydrogenation (Figure 4.6), similar trends for both Pd nanoparticle shapes were obtained and both profiles indicated that an Arrhenius-type kinetic model was sufficient to describe the effect of temperature. An a priori visual inspection of the morphology for the two shapes suggested that the dendrite-shaped nanoparticles would exhibit better catalytic properties by virtue of their pronounced branches, which provide additional surface area per mass. Indeed, Pd dendrites consistently exhibited a higher conversion per mass as a function of temperature. Since the reaction is considered structure insensitive, this difference was attributed to the available Pd surface for catalysis.

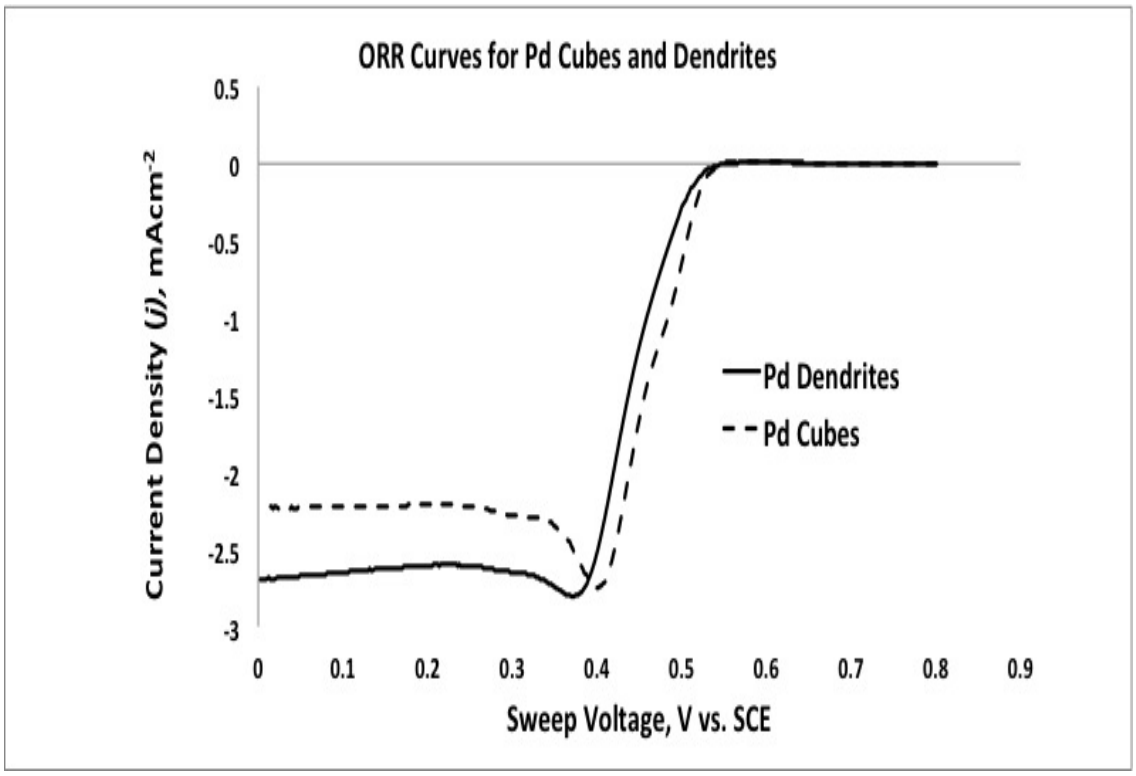

Figure 30 A comparison of the typical ORR profile recorded from Pd cubes and dendrites. ORR curves were recorded at 1600 rpm and a scan rate of 10mV.

Static H_2 sorption measurements (Figure 4.7) showed that the amount of sorbed H_2 per mass of Pd was higher for Pd nanocubes than it was for the Pd dendrites. In other words, the same trend that was observed with CV experiments was observed here as well (Figure 4.2). Additionally, the amount of hydrogen sorbed to the Pd nanocubes under electrochemical conditions was at least twice that for the Pd dendrites. Despite this difference, calculated H:Pd ratios revealed that there were approximately 0.0276 H atoms for every Pd atom. This ratio suggests that the two phases of the PdH species are present in both sets of experiments.

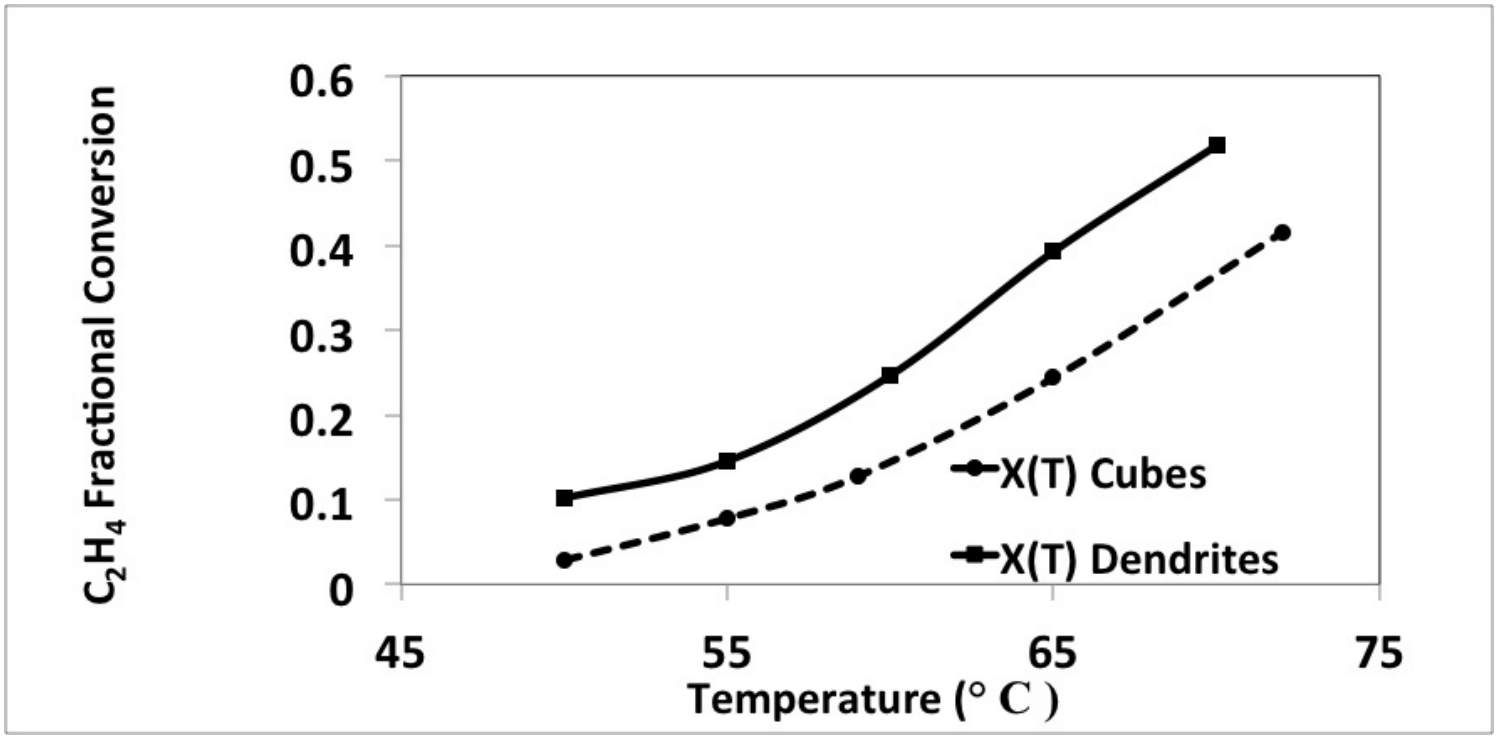

Figure 31 Ethylene hydrogenation fractional conversion as a function of temperature for Pd dendrites and cubes.

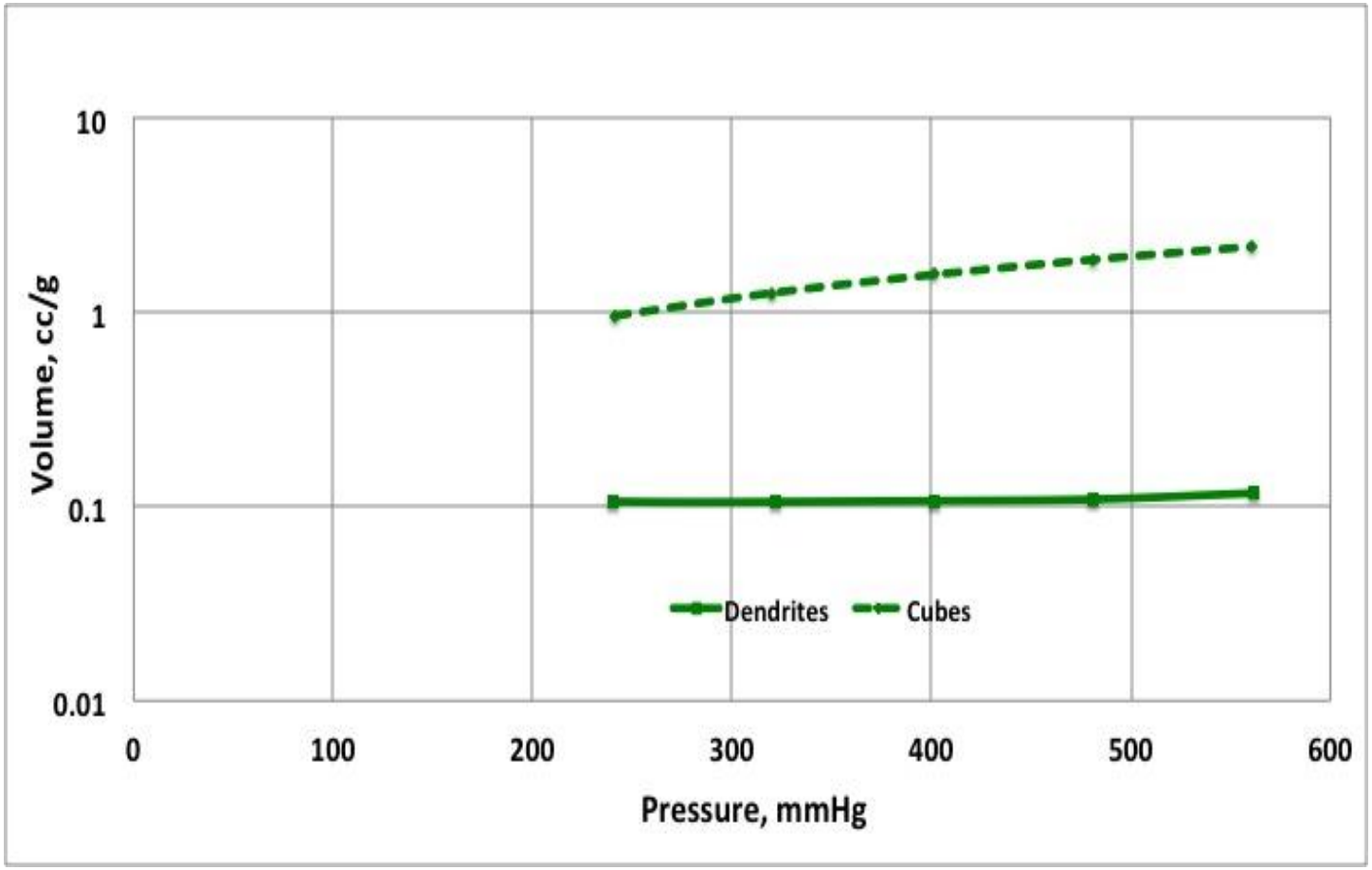

Figure 32 Comparison of H_2 sorption results for Pd dendrites and cubes.

The differences observed in interaction between the Pd nanoparticles and hydrogen, we propose, are caused by the differences in morphology that exist between the two shapes of Pd nanoparticles. In general, the interaction between the Pd nanoparticles and hydrogen atoms falls under one of two categories. Low concentrations of PdH or the α-phase consist of concentrations up to 0.015 H atoms per Pd atom. The β phase co-exists with the α-phase between 0.015H and 0.6H. [123] Beyond this concentration, the β phase species exists exclusively. The evolution of the β phase is accompanied by an expansion of the Pd fcc lattice [123]. In light of this, an orientation preferentially exposing the (100) plane, more prevalent in Pd cubes, logically would facilitate interstitial diffusion and interaction of hydrogen atoms with surface and sub-surface Pd sites.

The results presented are consistent with the behavior of Pd-hydrogen systems. This difference was manifested by a higher prevalence of the (100) planes in Pd nanocubes relative to Pd dendrites. A prevalence of (100) facets in Pd nanocubes would facilitate a flux of hydrogen atoms into the sub-surface of the Pd material ensures an improved coverage of hydrogen on the Pd material. This finding agrees with the trends showed in H_2 sorption measurements under electrochemical conditions discussed earlier which both showed a better interaction of hydrogen with the Pd nanocubes.

4.5 Conclusions

In this work, the difference in NP design was used to study the electrocatalytic properties of different shapes of Pd NPs. Based on our results and the apparent interaction of Pd with H_2, catalytic experiments were performed to elucidate differences in the interaction of H_2 the different shapes of Pd NPs. Our findings indicate that the electrochemical interaction of Pd with H resulted in an ORR activity difference that was only slightly higher for Pd cubes. A Koutecky-

Levich analysis showed that the 4-electron pathway predominated for both shapes of Pd NPs although the Pd dendrites had a higher average number of electrons when measured as a function of potential. Also, the non-linear trend that was observed in the HOR ECSA measurements compared with the linear trend observed in the Oxide peak integration brings into question, the confidence in the accuracy of the HOR ECSA measurement. Furthermore, it suggests that the oxide peak might be a better reference for ECSA determination, since it demonstrated a linear decreasing trend throughout the cyclic voltammetry experiment.

Ethylene hydrogenation experiments favored dendrites, which showed a higher conversion. The results of this study demonstrated a strong impact of the role of Pd particle shape on the ability to store hydrogen within the Pd structure. Results obtained for experiments involving Pd nanocubes and dendrites showed that the prevalence of the (100)-lattice plane has an important influence on the facile sorption of hydrogen. This contribution provides insight into the design and application of varying shapes of Pd NPs for hydrogen storage by identifying structure-function relations for the ideal interactions in metal-hydrogen system. The results of this work indicate that the morphology and the prevalence of certain lattice planes in the first few layers of metallic material samples employed for hydrogen storage applications, could have an impact on the said material's ability to store hydrogen.

CHAPTER 5: PALLADIUM-BASED BIMETALLIC NP STUDY

5.1 Introduction

In this chapter, we extended our study of Pd based nanoparticles for low temperature fuel cell applications. In the process, we adopted two different approaches for NP synthesis that are described in Chapter two. One approach took advantage of the ability to generate sub-5nm nanoparticles through a Dendrimer Encapsulated Synthesis techniques, that we also used for other applications within our group. [124, 125] This technique provides an efficient means of generating very small NPs with high surface area. In addition to traditional catalytic and bio-inspired applications including the ones cited above. DENs have also been used to generate electrocatalysts for low temperature fuel cell applications. In this regard, the Crooks group at the University of Texas has published several journal articles on the subject. [35-37, 126]

The second approach for the synthesis of Pd based NPs, also described in Chapter 2, was inspired by the work of Chen et al. [39] Instead of monometallic Au nanocages however, work in our group adapted this process to generate ca. 50nm Pd nanocages whose properties would be studied for bio-inspired catalytic applications. Details of the synthesis and characterization can be found in the published dissertation of Hokenek, S.[127] In both cases, a combination of Pd and Ag was used in different ratios in an effort to establish a trend that was a function of the material concentrations with the different compositions.

In the adaptation of these NPs for electrocatalytic applications, the goal of this work was to elucidate how ligand and geometric effects might play a role in the resulting electrocatalytic activity of the NPs under study. Indeed, ligand and geometric [45-47] effects could play an important role in improving the activity of bimetallic electrocatalysts [48]. Ligand effects rely on changing the electronic structure of the primary metal site [49] through which a favorable charge transfer is induced while geometric effects as the name suggests, rely on factors including particle size, dispersion state and bond strain.

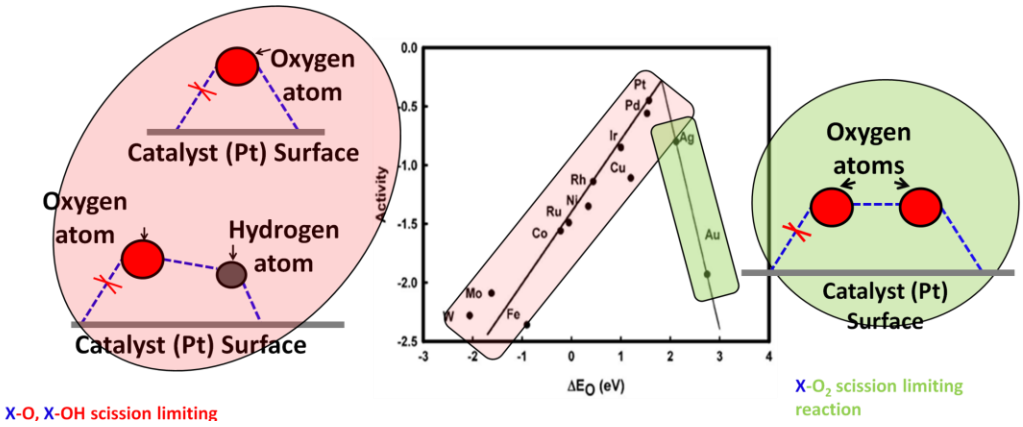

Figure 33 A volcano plot based on DFT studies on the (111) plan of different transition metal surfaces. Picture adapted from Norskov et. al [31]

This work was guided by the following two hypotheses which build on the modeling work proposed by Norskov et. al, summarized in figure 33 above.

Hypothesis 1: Here-in, the influence of ligand effects will be inversely proportional to the oxygen binding energy of the bimetallic systems under consideration, with a more pronounced effect on left volcano branch Pd pairs.

Hypothesis 2: The bimetallic pairs with low binding energies will favor oxygen reduction. By virtue of the lattice faces that favor O_2 reduction, Pd-Ni, Pd-Pt nanocubes will have

lower binding energies than nanospheres, while for Pd-Ag, nanospheres will have lower binding energies than nanocubes

5.2 Electrochemistry Experiments

A series of electrochemistry experiments, very similar to the ones in the previous chapters were adopted for the bimetallic study as well. One difference however, was in the use of an alkaline environment in addition to the acidic environment to study the electrocatalytic properties of select bimetallic pairs. In all, $PdNi_{11}$ and $PdAg_{11}$ DEN batches were studied. In addition, $AgPd_{10\text{-ACID}}$, $AgPd_{10\text{-ALKALINE}}$, $AgPd_{6\text{-ALKALINE}}$ nanocages with 5nm and 10nm Pd shells respectively were also studied.

5.2.1 Cyclic Voltammetry

The acid environment was prepared in a similar manner to that described in previous chapters. The alkaline environment was prepared using an electrolyte solution prepared from 100mL 0.1M $NaOH_{(aq)}$ (Sigma Aldrich). A series of 20 cycles were run in the 0 to -0.8V range vs. SCE to establish a steady state curve. In all, 20 cycles at $100mVs^{-1}$ under Ar. After the CV experiment and still under Ar, an ORR curve was recorded at 3600rpm and $10mVs^{-1}$ before switching the gas flow to O_2.

5.2.2 Oxygen Reduction Reaction

ORR experiments consisted of voltage sweeps from (0.0 vs. SCE) to (-0.8 vs. SCE) at $10mVs^{-1.}$ Sweep experiments were started after flowing O_2 for atleast 30 minutes. A series of six different ORR curves were recorded at 100, 400, 900, 1600, 2500 and 3600rpm respectively ORR In order to account for the capacitive current due to the electrolyte, the background sweep scan was subtracted from each of the ORR curves to elucidate the ORR curve that was attributed to the modified working electrode exclusively.

CV and ORR and data were normalized by the geometric surface area of the GCE and the resulting current density was reported as a function of the sweep voltage.

5.3 Results & Discussion

5.3.1 Pd-Ag Nanocage

In general, it was observed that the quality of the Cyclic Voltammogram (in acidic medium) depended directly on the Pd composition of the film. The higher the Pd concentration, the more defined the nature of the CV curve in the NP film. Indeed, despite the low ECSA, $AgPd_{10}$ exhibited distinct features of the Pd cyclic voltammogram. However the suppressed HOR peak suggests the presence of a second material, Ag, may not be synergistic during the reduction process. In fact, a Koutecky-Levich analysis revealed an electron number, *n,* in excess of either pathway known to be adopted by the oxygen reduction process. Details of the analysis of the $PdAg_{10}$ nanocages under acidic and alkaline media are provided in figures 34 - 36 as well as table 6. Under alkaline media, $PdAg_{10,}$ appears to be active although the activity was limited to the 2-electron pathway of oxygen reduction according to the Koutecky-Levich analysis. It is proposed that the activity observed is due primarily to Ag, a good ORR catalyst under alkaline conditions [128, 129], especially since it has a lower binding energy for the OH than Pd. Still, the Ag-catalyzed ORR process, typically a 4-electron process, [128-130] seems to be hindered by the bimetallic nature of the NP film, which by virtue of the Pd shell thickness would obstruct access to the Ag surface. Indeed, in a similar process resulting in PdAg nanoboxes, Skrabalak et. al [131] describe the solid-solid interdiffusion and subsequent de-alloying typical of PtAg and PdAg systems. However, they explain, that unlike the PtAg, system, they observed a blocking to the pore formation that would result in the hollow core or nanocage resulting in PdAg alloys instead of nanoboxes.

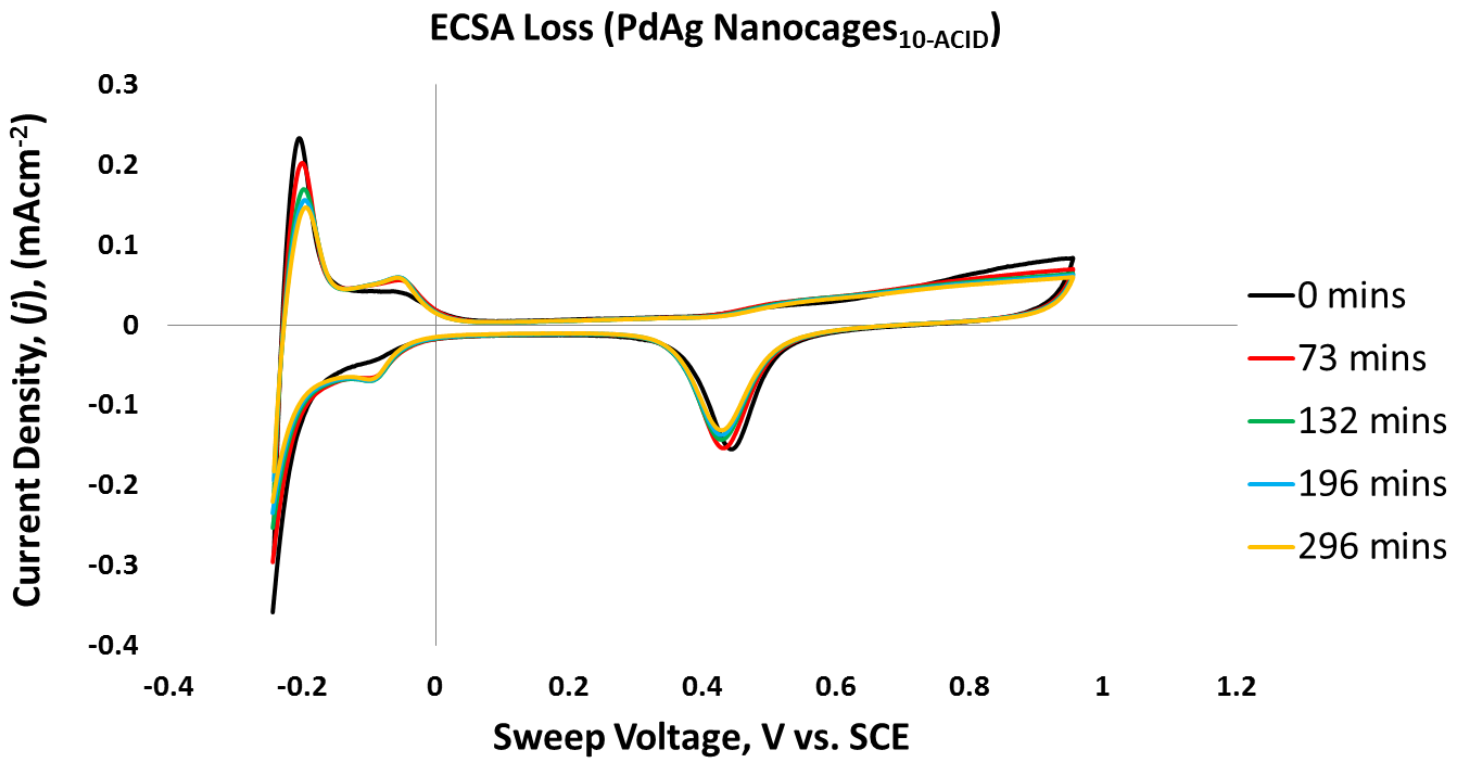

Figure 34 Stability test of $AgPd_{10}$ nanocages showing the change in current density / reduction in ECSA as a function of time.

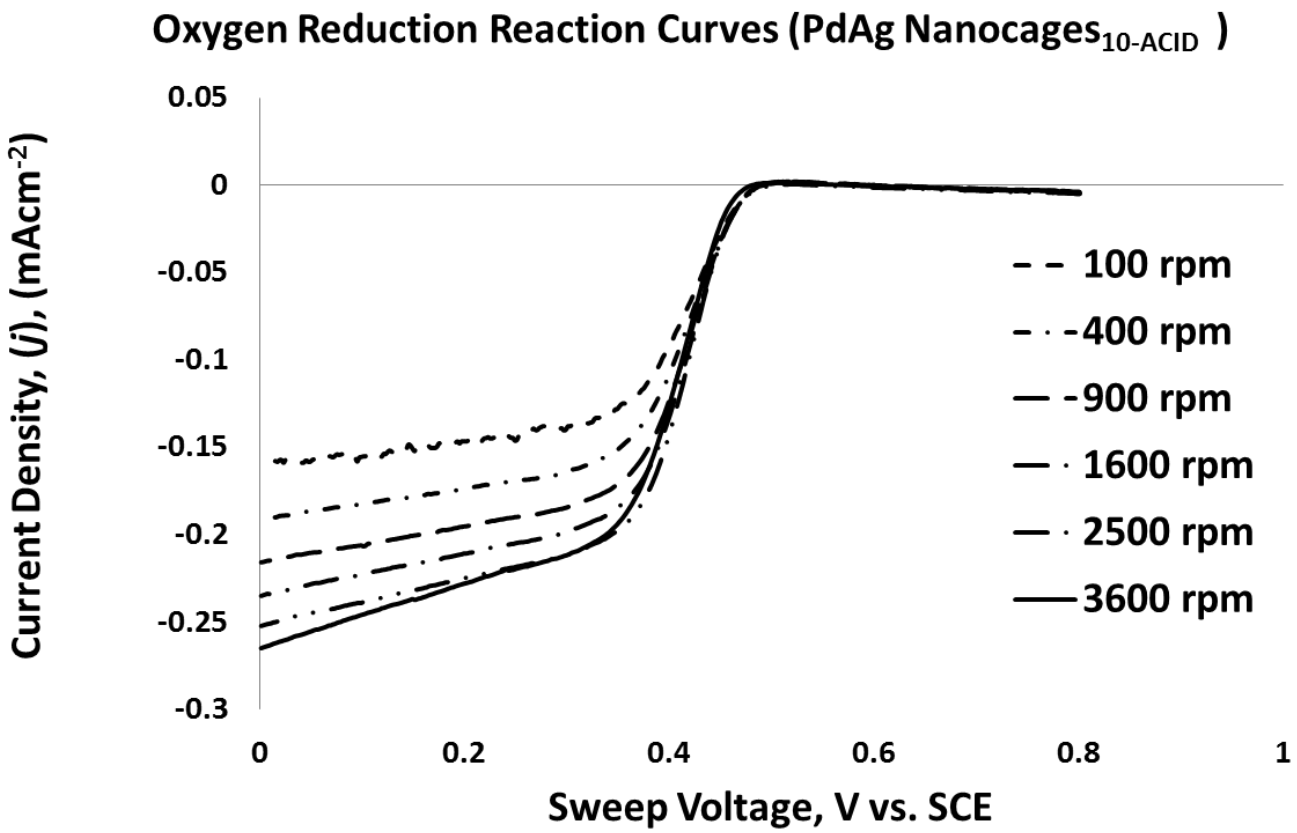

Figure 35 Oxygen Reduction Reaction curves for $AgPd_{10}$ in acidic media at different rotation speeds. The scans were recorded at a scan rate of 10mV/s and a step size of 2mV.

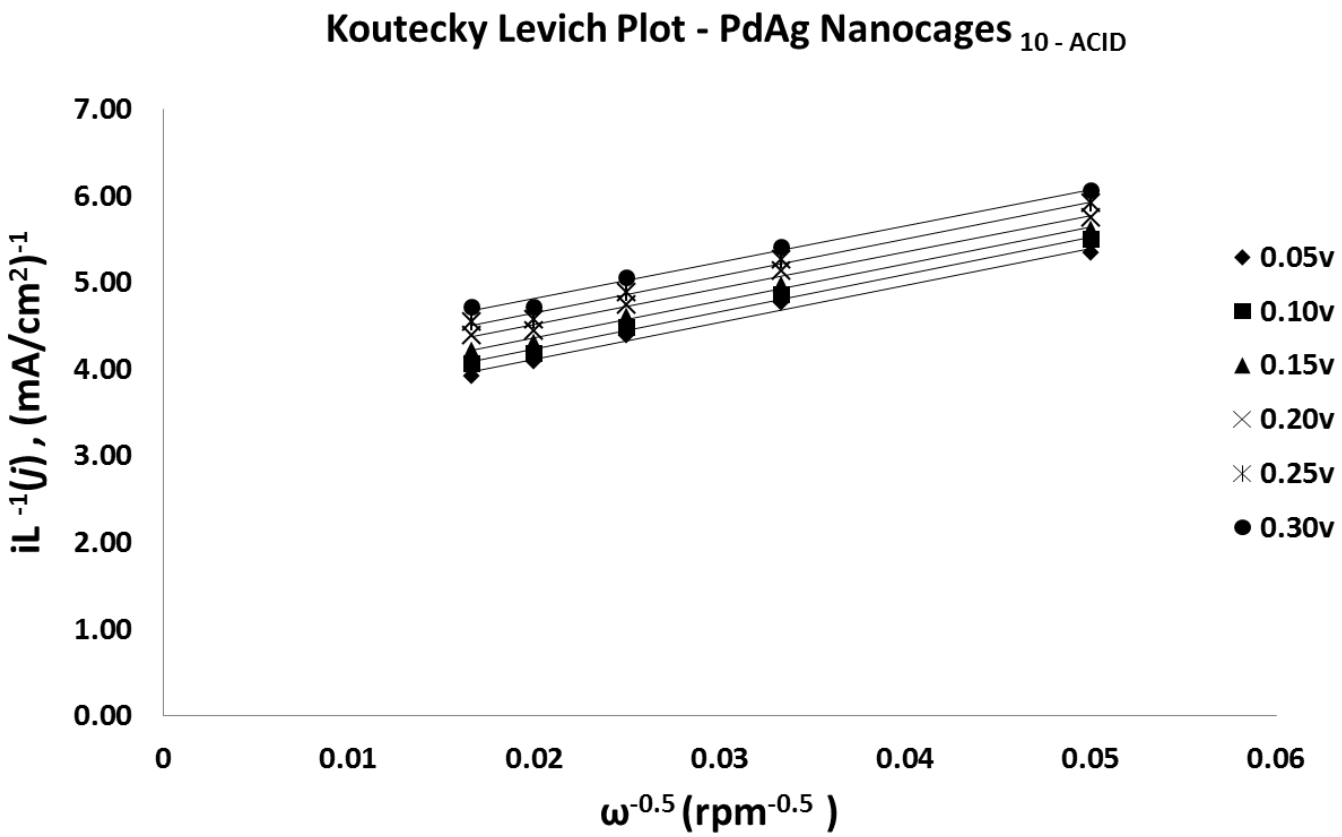

Figure 36 Koutecky-Levich Plot for $AgPd_{10}$ Nanocages in acidic media.

Table 6 Summary of Koutecky-Levich Parameters ($PdAg_{10}$) in acidic media

$AgPd_{10\text{-}ACID}$		**$iL^{-1}(V)$, ($mAcm^{-2}$)**					
ω, rpm	**$1/\omega^{0.5}$**	**0.05v**	**0.10v**	**0.15v**	**0.20v**	**0.25v**	**0.30v**
100	0.1	6.33	6.41	6.62	6.80	6.85	7.14
400	0.05	5.35	5.49	5.62	5.75	5.92	6.06
900	0.033	4.76	4.85	4.98	5.13	5.26	5.41
1600	0.025	4.39	4.48	4.61	4.74	4.88	5.05
2500	0.02	4.08	4.18	4.31	4.44	4.57	4.72
3600	0.017	3.92	4.07	4.22	4.39	4.55	4.72
No. of electrons, *n*		**0.65**	**0.64**	**0.65**	**0.66**	**0.65**	**0.66**

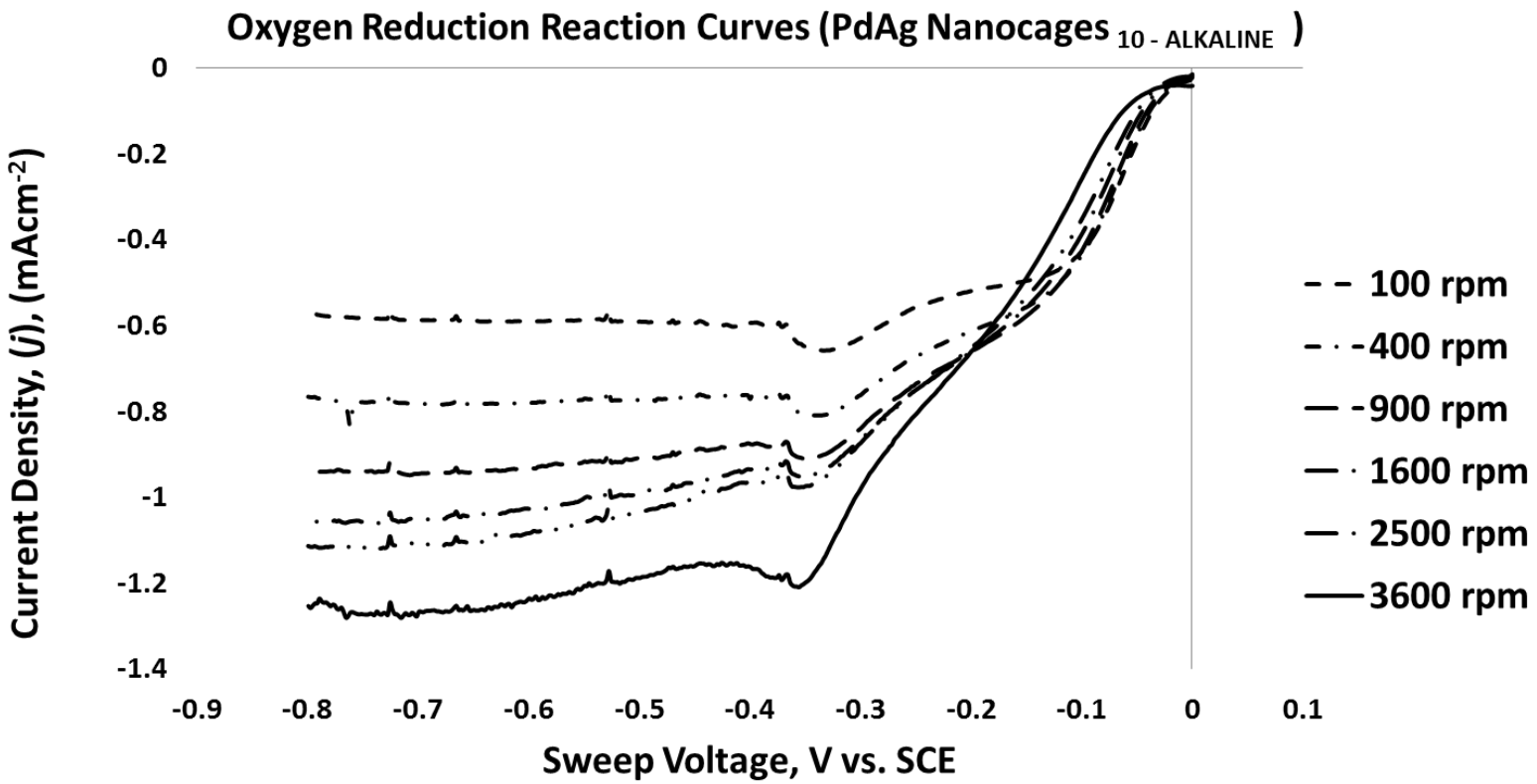

Figure 37 Oxygen Reduction Reaction curves for $PdAg_{10}$ in alkaline media at different rotation speeds. The scans were recorded at a scan rate of 10mV/s and a step size of 2mV.

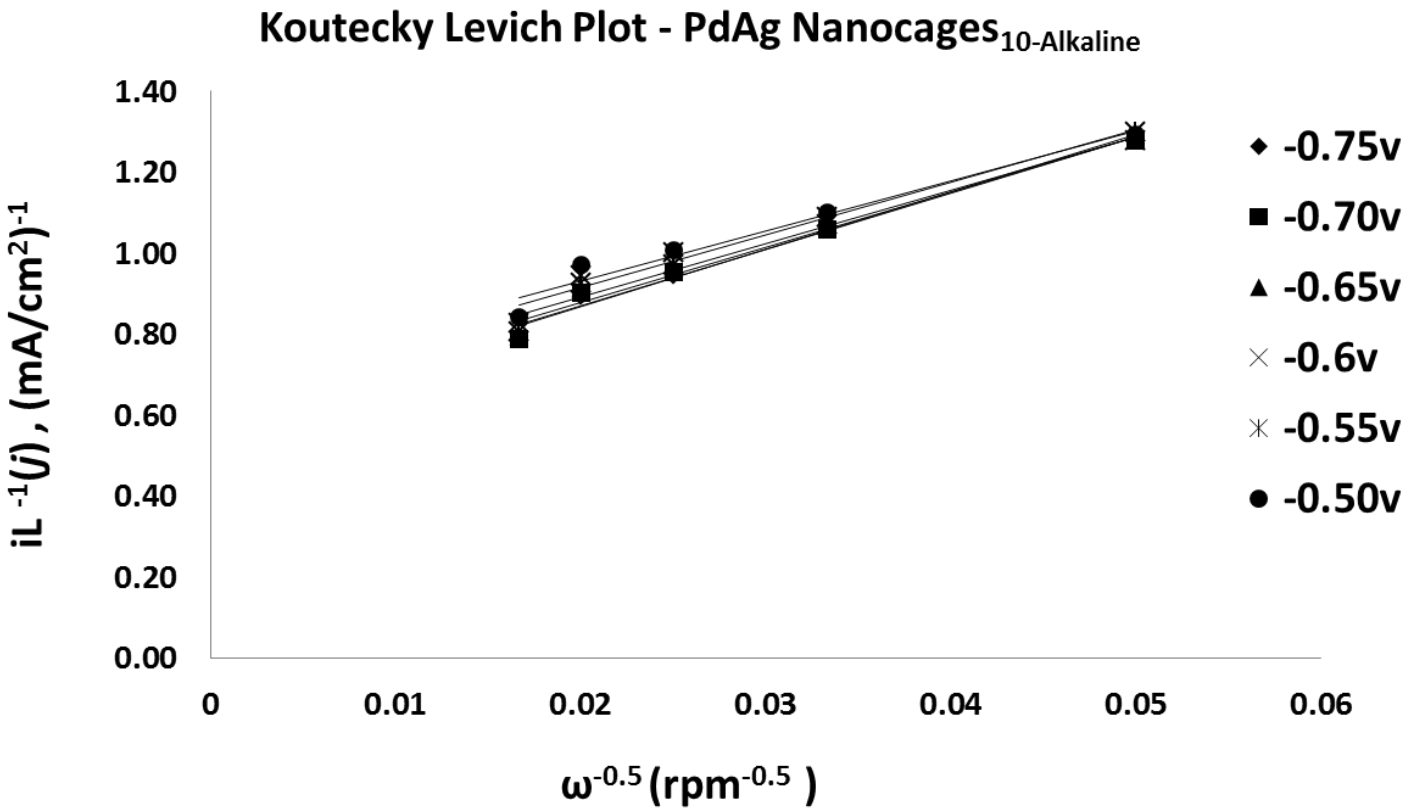

Figure 38 Koutecky-Levich Plot for $AgPd_{10}$ Nanocages in alkaline media.

Table 7 Summary of Koutecky-Levich Parameters ($PdAg_{10}$) in alkaline media

$PdAg_{10}$-ALKALINE		**$iL^{-1}(V)$, ($mAcm^{-2}$)**					
ω, rpm	**$1/\omega^{0.5}$**	**-0.75v**	**-0.70v**	**-0.65v**	**-0.60v**	**-0.55v**	**-0.50v**
100	0.1	1.71	1.70	1.69	1.69	1.71	1.69
400	0.05	1.28	1.28	1.28	1.28	1.30	1.29
900	0.033	1.06	1.06	1.06	1.07	1.09	1.10
1600	0.025	0.94	0.95	0.96	0.97	1.00	1.01
2500	0.02	0.89	0.90	0.91	0.93	0.94	0.97
3600	0.017	0.79	0.79	0.79	0.81	0.83	0.84
No. of electrons, *n*		**1.96**	**2.01**	**2.05**	**2.11**	**2.13**	**2.24**

This observation would suggest, then that the ORR activity of the PdAg system under consideration in alkaline media would be driven primarily by the composition of the alloy and not necessarily by the presence of a cavity resulting from the galvanic process, presenting additional surface area. Moreover, the addition of a high Pd concentration would most likely envelop the Ag cubes and reduce access to the core, based on Skrabalak et al. [131] Thus, a thinner shell (or smaller Pd concentration) should result in a more efficient process. Indeed, when the shell size was reduced to 6nm, or smaller deposits of Pd were employed, the number of obscured Ag sites would reduce, and an improvement in the apparent pathway was observed. As the results of the Koutecky-Levich analysis revealed, the thinner Pd shell resulted in a higher average electron number recorded. While the average electron number for the $PdAg_{10}$ shell was 2.08, the average electron number for the $PdAg_6$ film was 3.49 suggesting that the 2-electron process was still significant with $PdAg_6$ being more efficient at the direct oxygen reduction process. A comparison of the electron numbers from the Koutecky-Levich analysis was made with recent literature [130] values and this revealed that the values corresponded closely with numbers recorded for bulk Ag. However since the OH binding energies for Pd and Ag are so close, [31] it is presumed that the comparison would hold for PdAg systems as well.

5.3.2 Pd-based DEN Systems

Like with the PdAg nanocage systems, it is believed that the resulting pattern in the ORR curve was due in part to the quality of the deposited film. In general, aqueous systems made for more stable depositions while organic- and DEN based depositions were less stable. This lack in stability translated to a reduction in the influence of mass transportation limitations in the diffusion limiting current region of the ORR curves. Still an interesting trend was observed in the change in CV pattern before and after the ORR studies. When Pd combined with an equivalent

mole ratio of Ni, the observed cyclic voltammogram was more, well defined (see figure 41). The delayed hydrogen peak was suggestive of the combination of Pd with another material, in this case, Ni. In a similar composition involving sub-10nm bimetallic nanoparticles of Pd and Ag, the trend was different. Features of the CV voltammogram were much less distinct in the ECSA observed, as is suggested by the differences in the CV voltammograms for the $PdAg_{11}$ system before and after the ORR studies. Indeed, the trend here would seem to suggest that bimetallic nanoparticle pairs with lower combined binding energies for oxygen reduction. Indeed, Koutecky-Levich analyses of the two bimetallic systems revealed that $PdNi_{11}$ was much more efficient at facilitating the 4-electron oxygen reduction reaction pathway, with an average electron number calculated to be 4.24. In the case of $PdAg_{11}$ however, the average number of electrons calculated was well out of range suggesting perhaps that an alkaline environment, like in the case of the PdAg nanocage system, would be a better avenue to capture the associated oxygen reduction reaction kinetics.

5.4 Conclusions

The results, though inconclusive, suggest that in acidic media, CV features due to Pd were prominent. In alkaline conditions, better ORR kinetics were observed with average electrons numbers in agreement with literature. De-alloying limited the potential of additional surface area that could promote accelerated ORR kinetics. While, n values corroborated bulk Ag estimates, from literature, similar Pd and Ag binding energies would require a deeper examination to de-convolute contributions from either material. Equimolar DEN PdAg and PdNi NPs were evaluated for ORR activity in acidic media. While PdAg system results suggested similities to PdAg nanocages, PdNi system was more efficient at facilitating the 4-electron oxygen reduction reaction pathway with an average n value of 4.24 and excellent CV features.

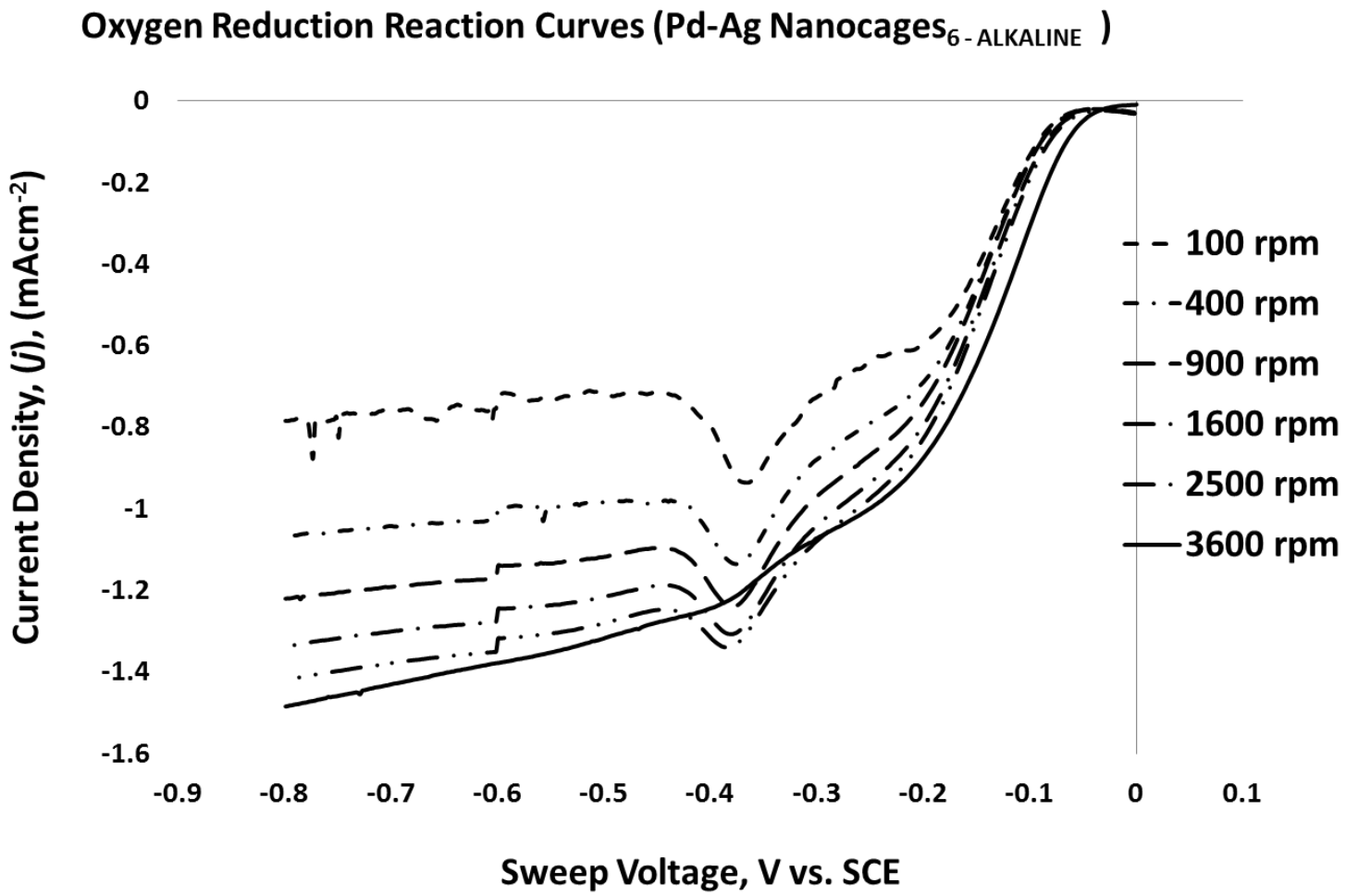

Figure 39 Oxygen Reduction Reaction curves for $PdAg_6$ in alkaline media at different rotation speeds. The scans were recorded at a scan rate of 10mV/s and a step size of 2mV.

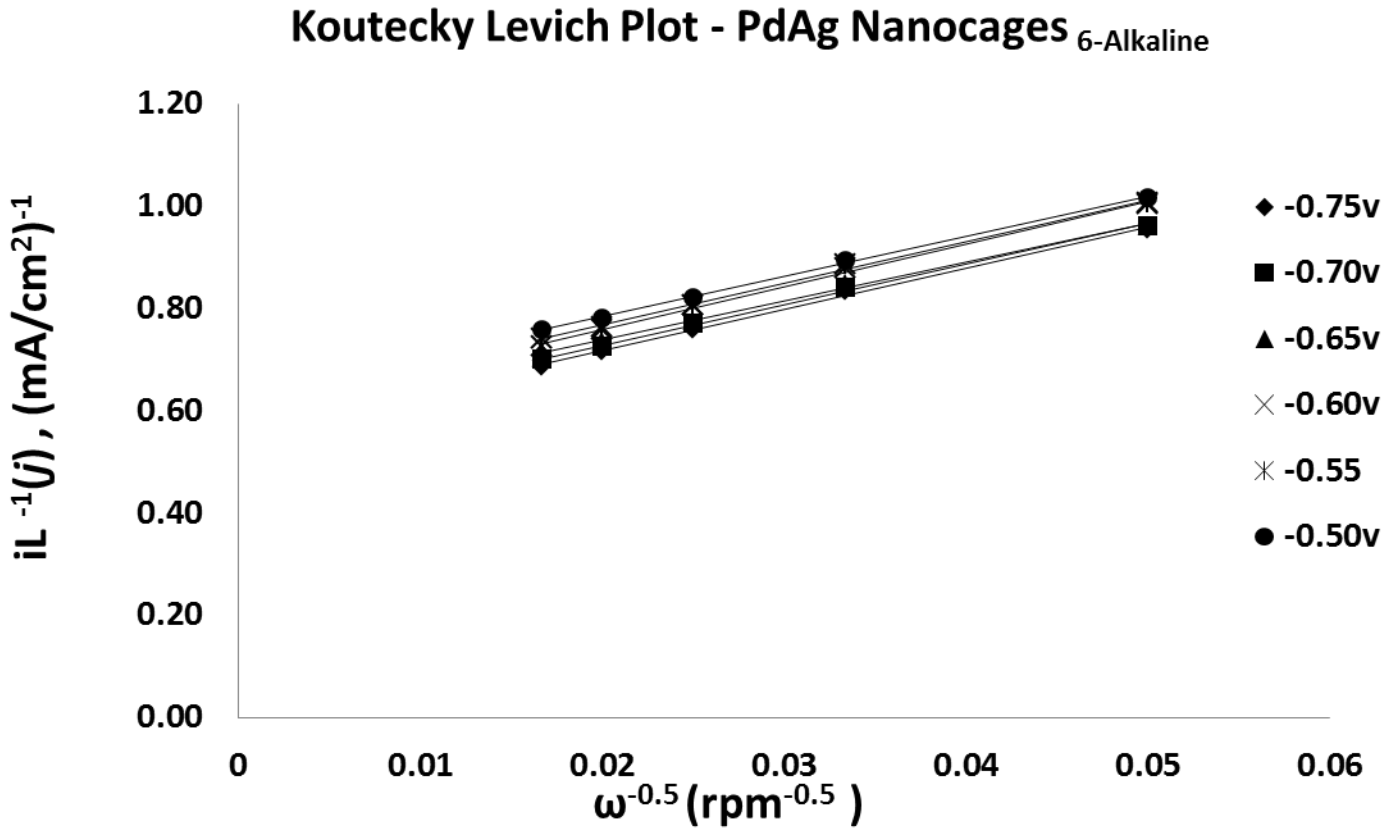

Figure 40 Koutecky-Levich Plot for $AgPd_6$ Nanocages in alkaline media.

Table 8 Summary of Koutecky-Levich Parameters ($PdAg_6$) in alkaline media

$PdAg_{6\text{-ALKALINE}}$		**$iL^{-1}(V)$, ($mAcm^{-2}$)**					
ω, rpm	**$1/\omega^{0.5}$**	**-0.75v**	**-0.70v**	**-0.65v**	**-0.60v**	**-0.55v**	**-0.50v**
100	0.1	1.21	1.32	1.31	1.39	1.36	1.38
400	0.05	0.95	0.96	0.96	1.00	1.01	1.02
900	0.033	0.83	0.84	0.85	0.88	0.88	0.89
1600	0.025	0.76	0.77	0.78	0.81	0.81	0.82
2500	0.02	0.71	0.72	0.74	0.76	0.76	0.78
3600	0.017	0.68	0.70	0.71	0.72	0.74	0.76
No. of electrons, *n*		**3.45**	**3.51**	**3.69**	**3.34**	**3.44**	**3.54**

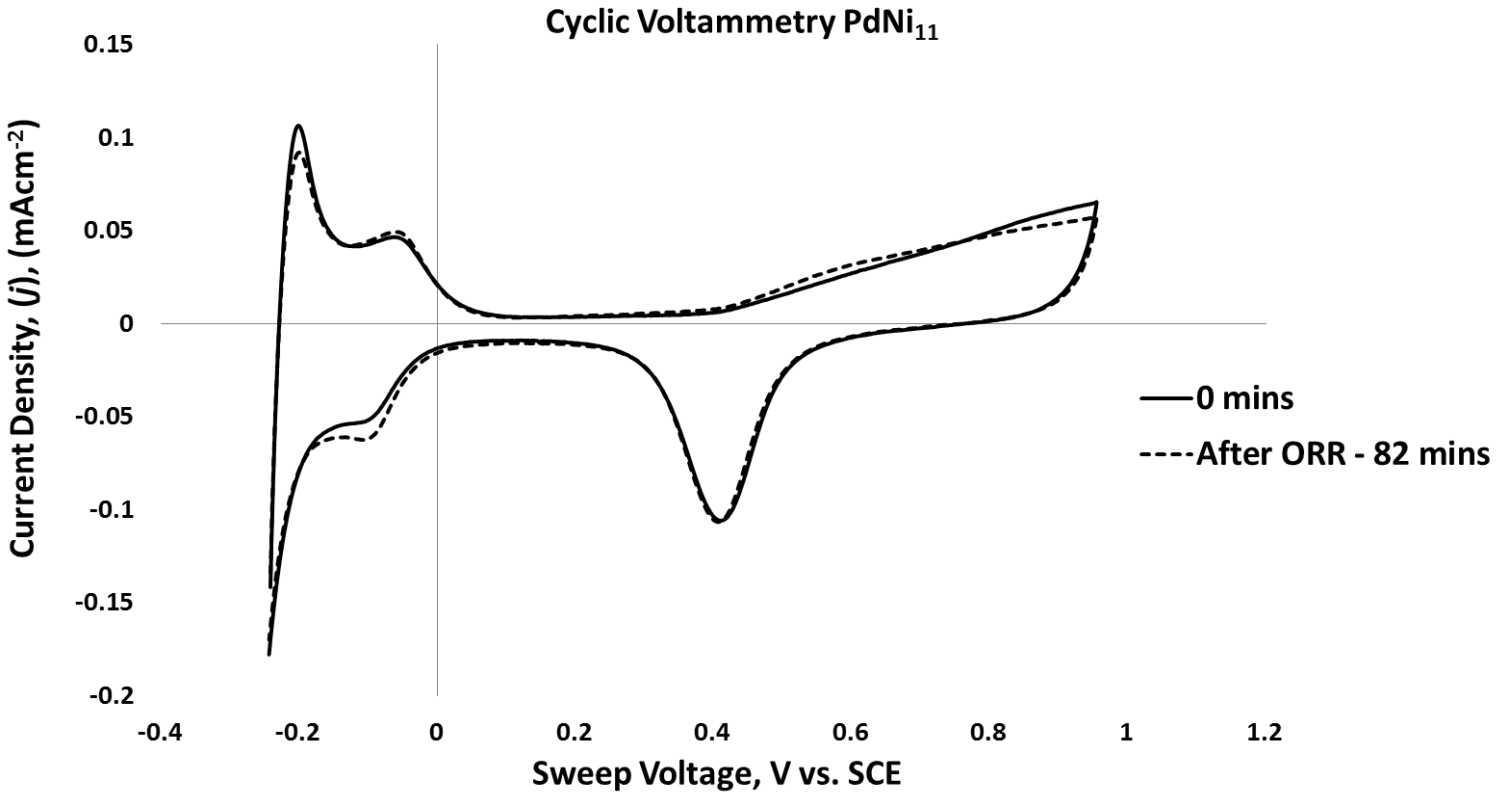

Figure 41 Stability test of $PdNi_{11}$ sub-10nm bimetallic DENs in acidic media showing the change in current density / reduction in ECSA as a function of time.

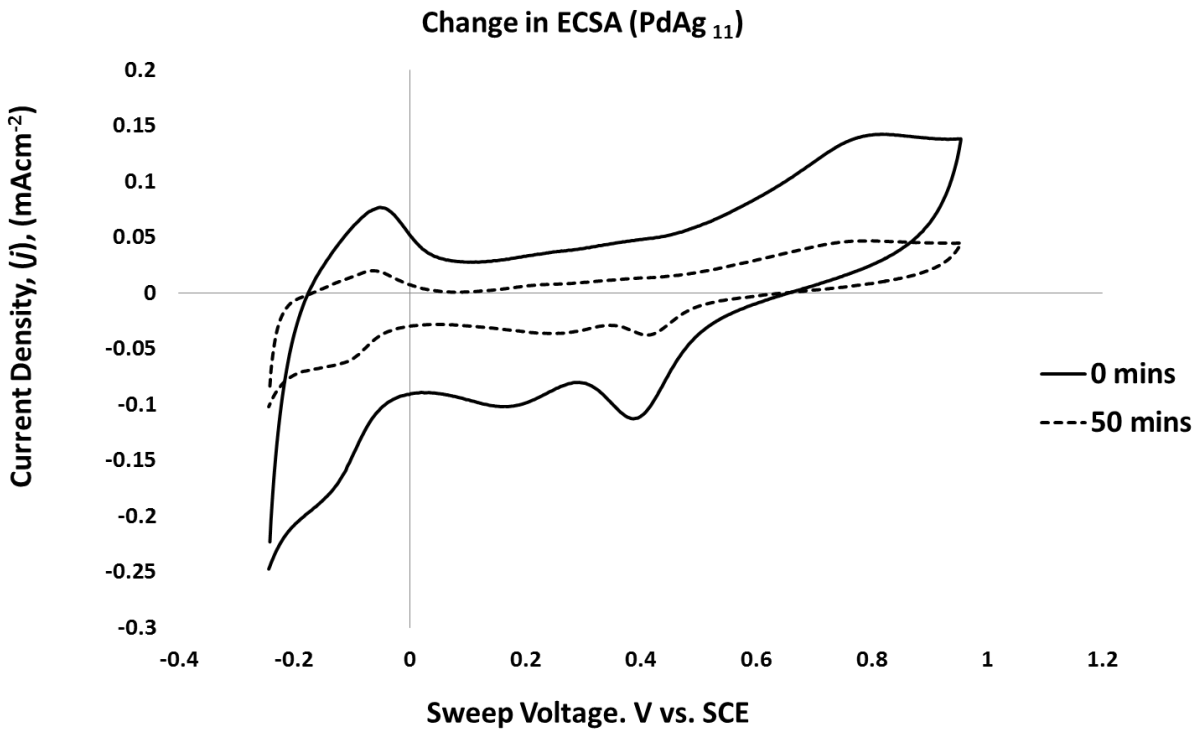

Figure 42 Stability test of $PdAg_{11}$ sub-10nm bimetallic DENs in acidic media showing the change in current density / reduction in ECSA as a function of time.

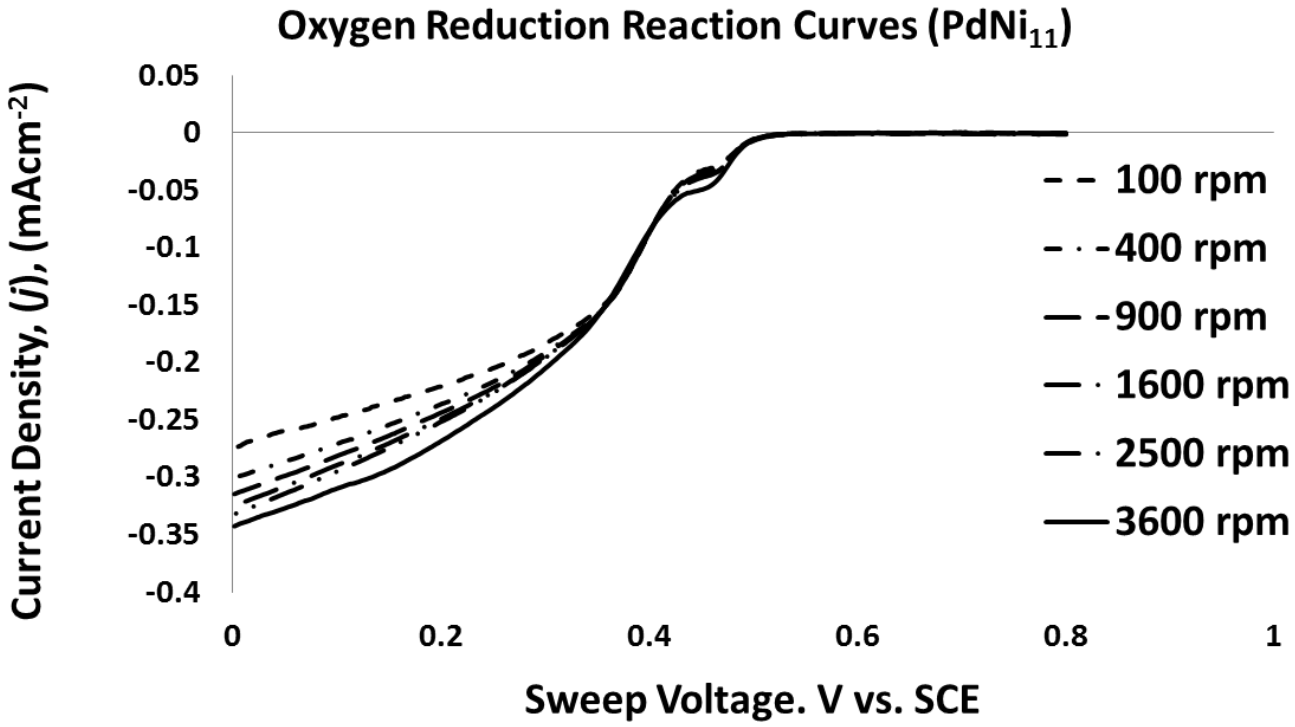

Figure 43 Oxygen Reduction Reaction curves for $PdNi_{11}$ DENs in acidic media at different rotation speeds. The scans were recorded at a scan rate of 10mV/s and a step size of 2mV.

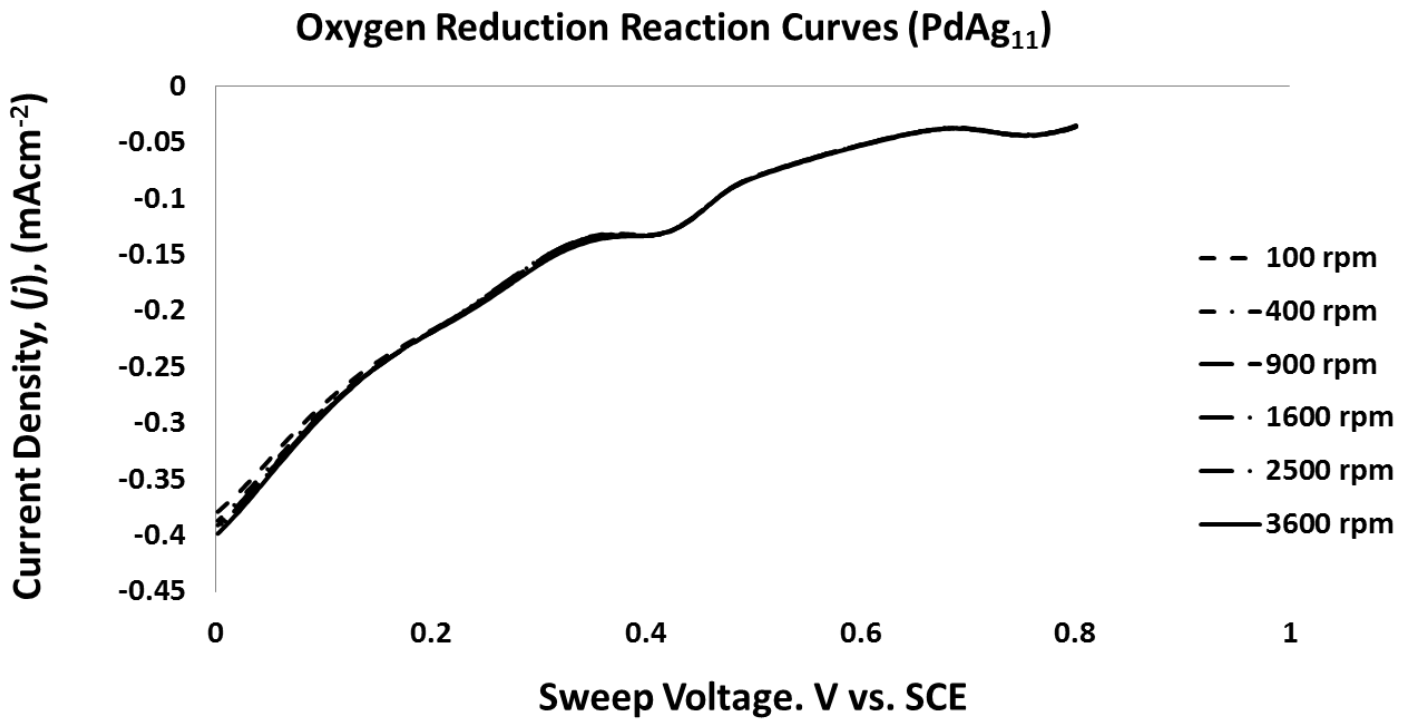

Figure 44 Oxygen Reduction Reaction curves for $PdAg_{11}$ DENs in acidic media at different rotation speeds. The scans were recorded at a scan rate of 10mV/s and a step size of 2mV.

Table 9 Summary of Koutecky-Levich Parameters ($PdNi_{11}$ DEN) in acidic media

$PdNi_{11}$		**$iL^{-1}(V)$, ($mAcm^{-2}$)**					
ω, rpm	**$1/\omega^{0.5}$**	**0.05v**	**0.10v**	**0.15v**	**0.20v**	**0.25v**	**0.30v**
100	0.1	3.86	4.03	4.26	4.52	4.88	5.43
400	0.05	3.50	3.69	3.92	4.22	4.61	5.21
900	0.033	3.34	3.55	3.79	4.10	4.50	5.13
1600	0.025	3.25	3.45	3.69	4.00	4.42	5.10
2500	0.02	3.18	3.39	3.64	3.97	4.41	5.10
3600	0.017	3.06	3.23	3.40	3.72	4.17	4.85
No. of electrons, *n*		**3.36**	**3.54**	**3.40**	**4.02**	**4.69**	**6.42**

Table 10 Summary of Koutecky-Levich Parameters ($PdAg_{11}$ DEN) in acidic media

$PdAg_{11}$		**$iL^{-1}(V)$, ($mAcm^{-2}$)**					
ω, rpm	**$1/\omega^{0.5}$**	**0.05v**	**0.10v**	**0.15v**	**0.20v**	**0.25v**	**0.30v**
100	0.1	3.00	3.50	4.07	4.59	5.26	7.37
400	0.05	2.95	3.47	4.00	4.55	5.26	6.41
900	0.033	2.92	3.45	4.00	4.55	5.29	6.41
1600	0.025	2.91	3.44	4.00	4.57	5.32	6.45
2500	0.02	2.91	3.44	4.00	4.57	5.32	5.10
3600	0.017	2.88	3.41	4.00	4.55	5.21	6.21
No. of electrons, *n*		**22.07**	**35.72**	**14.42**	**89.66**	**-39.80**	**3.83**

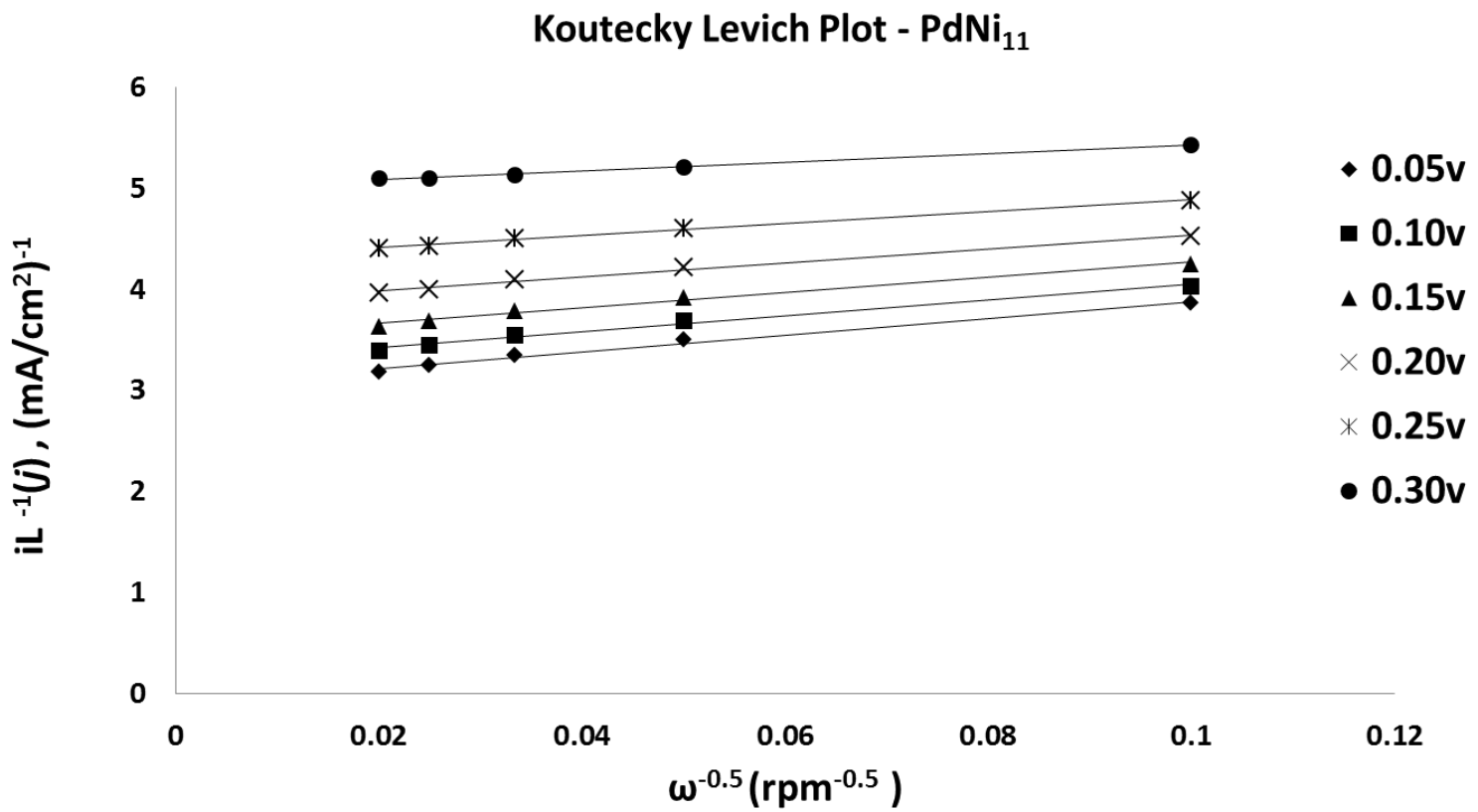

Figure 45 Koutecky-Levich Plot for $PdNi_{11}$ DENs in acidic media.

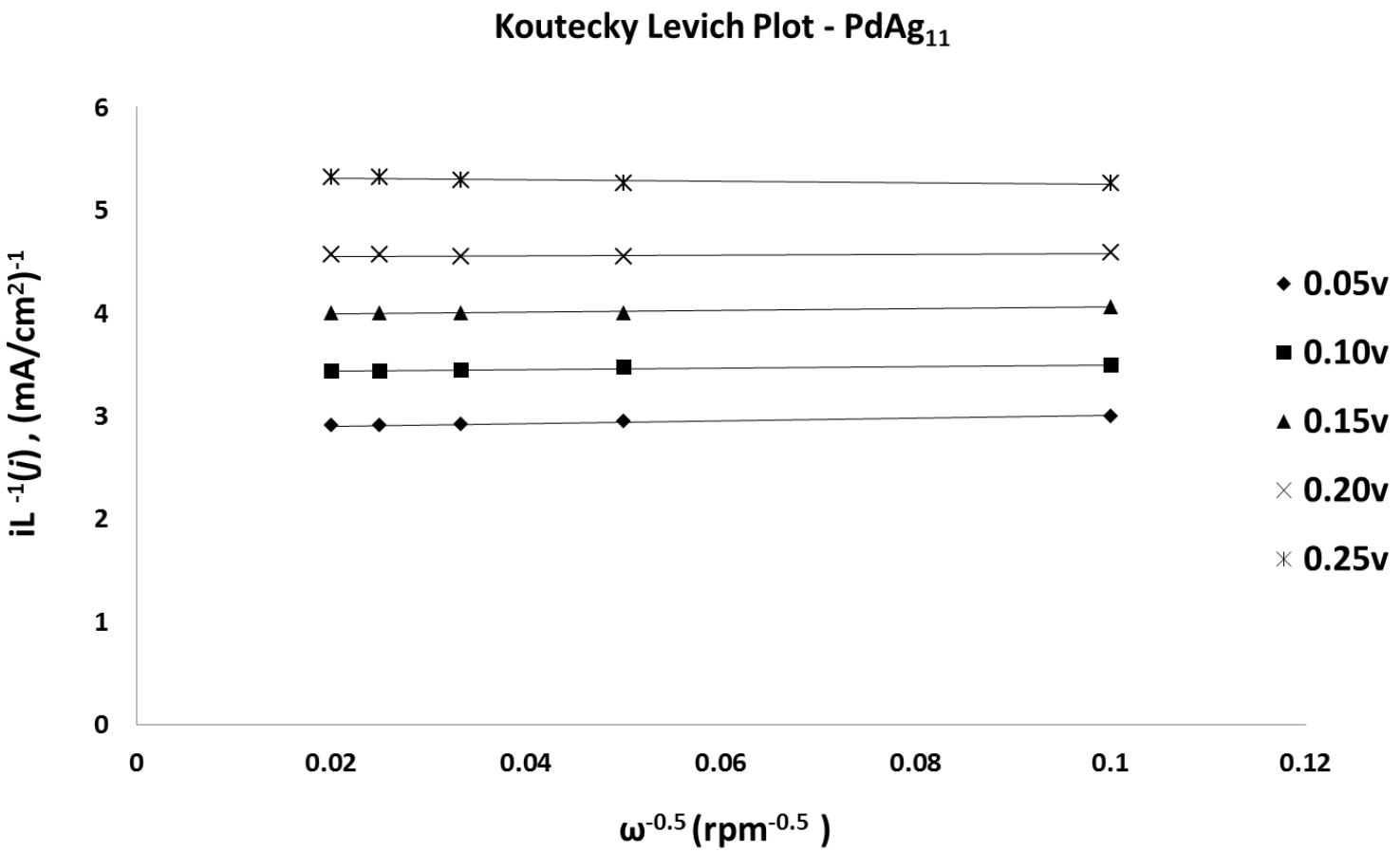

Figure 46 Koutecky-Levich Plot for $PdAg_{11}$ DENs in acidic media.

CHAPTER 6: PROPOSED FUTURE WORK

6.1 Syntheses and Study of Additional Shapes

The synthesis and electrocatalytic study of additional shapes is an area, which holds tremendous promise for the future of this work. As novel approaches to generating new morphologies and composition of catalysts become evident, so will our understanding of NP shape-based electrocatalysis. Particularly, the ability to tailor monometallic shapes, driven by kinetic factors such as the concentration of composition elements as well as reaction time and temperature [34, 132-137] will continue to be of significant interest since many more shapes are yet to be studied. Bimetallic [43, 46, 138-145] and now trimetallic [146-151] compositions are also becoming increasingly popular.

The challenge though will be to harmonize variables including composition, shape and size into a geometry that is favorable to ORR catalysis. Thus, it may be possible to reproduce or surpass the intrinsic electrocatalytic activity of Pt. However, the approach will continue to be guided by how geometric and ligand effects affect the resulting geometry, which can – at least in theory - be predicted by DFT modeling as a means of screening new potential catalysts.

6.2 In-situ FTIR Electrochemical Cell Modification

One of the missing components of the current work is the ability to make transient measurements within the electrochemical reactor. Among other things, this added capability would compliment CV, ORR and activity data by describing how these vary with respect to other

factors such as the rate of ECSA loss, etc. In-situ electrocatalysis is a growing approach to informing more accurately the transient analysis of electrocatalytic systems [46, 152-159]

The current electrocatalytic system will be well enhanced through modifications that can enable in-situ experiments which for example, look at the concentration profile of electrocatalyst material on the surface of the GCE, or an evaluation of the GCE: electrocatalyst: Nafion system and through electron imagery and surface scanning.

6.3 Life Cycle Assessment Modeling (Sima Pro)

One of the main arguments behind the use of PEMFCs is the fact that it reduces the amount of emissions with this form of automotive technology relative to other technologies such as ICEs and the like. However, as discussed earlier, the scarcity of commercial quantities of readily available H_2 (g) for use in PEMFC means that H_2 (g) would have to be produced from auxiliary processes, which may or may not be as clean. Indeed, recognized processes for the generation of H_2 (g) include the steam reforming of CH_4 coupled with a water gas shift reaction to enhance the formation of more H_2 (g). Inherently, this process results in the generation of CO_2, which is a greenhouse gas.

It is possible to capture the entirety of all processes affiliated with the generation of a new product through the use of LCA tools and software. These instruments play an essential role in determining what the resulting environmental impact of a particular process is. They also represent an important step in the elucidation of the most efficient pathway for a particular process. The evaluation process may start from the extraction of raw products through their transportation, assembly and use through to their disposal.

An LCA analysis of PEMFCs, which employ various quantities of Pd- and Pd based catalysts, will make an argument for the commercial viability of the said PEMFCs. Furthermore,

juxtaposing the LCA evaluation of Pd catalyst based PEMFCs with that of other technologies such as ICEs, etc. will present a more realistic perspective of the "clean" credentials of this technology.

6.4 COMSOL Modeling

COMSOL ® is a finite element-modeling package that can account for the transport; heat and mass transfer and the kinetics of a given system. Three subdomains, corresponding to the three phenomena mentioned above, can be accurately modeled independently or coupled to describe a steady state or transient system. A number of COMSOL-related papers have focused on macro modeling [160-162], i.e. looking at phenomena on the level of the entire fuel cell or fuel cell component. A growing number of papers are starting to look at micro modeling [163], i.e. discrete aspects of PEMFC modeling. An example of particular interest is highlighted in the work presented by Cetinbas et al [164]. In this work, the authors studied the properties of discrete Pt NPs supported discretely on a carbon support and enveloped in an ionomer matrix. The results of this work hold relevance within the actual fuel cell but also at the bench scale.

A similar system can be envisaged for some of the different shapes and compositions of Pd and Pd-based NPs that we have synthesized. Variables such as particle size and shape can be varied to determine preliminary trends that evolve exclusively based on the varied parameter. This will inform experimental results by allowing us to isolate effects that are based on the studied variables and others that may be due to error or otherwise.

REFERENCES

1. Carrette, L., Friedrich, K.A., Stimming, U., *Fuel Cells - Fundamentals and Applications.* Fuel Cells, 2001. **1**: p. 5-39.

2. Borodko, Y., Humphrey, S., Tilley, T.D., Frei, H., Somorjai, G.A., *Charge-Transfer Interaction of Poly(vinylpyrrolidone) with Platinum and Rhodium Nanoparticles.* Phys. Chem. C, 2007. **111**: p. 6288-6295.

3. Ewald, J. *Carbon Dioxide at NOAA's Manua Loa Observatory reaches new milestone: Tops 400ppm*. 2013 05/10/2013 [cited 2013 May 12, 2013]; Available from: http://researchmatters.noaa.gov/news/Pages/CarbonDioxideatMaunaLoareaches400ppm.aspx.

4. Carrette, L., K.A. Friedrich, and U. Stimming, *Fuel Cells - Fundamentals and Applications.* Fuel Cells, 2001. **1**(1): p. 5.

5. O'Hayre, R., S.-W. Cha, W. Colella, and F.B. Prinz, *Fuel Cell Fundamenals*2006, New York: John Wiley & Sons.

6. Wright, P.V., *Polymer electrolytes - the early days.* Electrochimica Acta, 1998. **43**: p. 1137.

7. Scherer, G.G., Berichte der Bunsengesellschaft fur Physika-lische Chemie, 1990. **94**: p. 1008.

8. Sheng, W., *Electrocatalytic Activities of Supported Pt Nanoparticles for Low-Temperature Fuel Cell Applications.* Dissertation, 2010.

9. Heitner-Wirguin, C., *Recent advances in perfluorinated ionomer membranes: structure, properties and applications.* Journal of Membrane Science, 1996. **120**: p. 32.

10. Mauritz, K.A. and R.B. Moore, *State of Understanding Nafion.* Chemical Reviews, 2004. **104**(10): p. 50.

11. Wilson, M., F. Garzon, K. Sickafus, and S. Gottesfeld, *Surface Area Loss of Supported Platinum in Polymer Electrolyte Fuel Cells.* J. Electrochem. Soc., 1993. **140**(10)

.

12. Bing, Y., Liu, H., Zhang, H., Ghosh, D., Zhang, J., *Nanostructured Pt-alloy electrocatalysts for PEM fuel cell uxygen reduction reaction.* Chemical Society Reviews, 2010. **39**: p. 2184-2202.

13. Demarconnay, L., C. Coutanceau, and J.M. Léger, *Study of the oxygen electroreduction at nanostructured PtBi catalysts in alkaline medium.* Electrochimica Acta, 2008. **53**(8): p. 3232-3241.

14. Du, B., Zaluzhna, O., Tong, Y.J., *Electrocatalytic properties of Au@Pt nanoparticles: effects of Pt shell packing density and Au core sizew.* Phys. Chem. Chem. Phys, 2011. **13**: p. 11568-11574.

15. Kang, Y., Murray, C., *Synthesis and Electrocatalyic Properties of Cubic Mn-Pt Nanocrystals (Nanocubes).* JACS, 2010. **132**: p. 7568-7569.

16. Lang, H., S. Maldonado, K.J. Stevenson, and B.D. Chandler, *Synthesis and Characterization of Dendrimer Templated Supported Bimetallic Pt-Au Nanoparticles.* JACS, 2004. **126**(40): p. 8.

17. Leontyev, I.N., D.Y. Chernyshov , V.E. Guterman, E.V. Pakhomova, and A.V. Guterman, *Particle size effect in carbon supported Pt–Co alloy electrocatalysts prepared by the borohydride method: XRD characterization.* Applied Catalysis A: General, 2009. **357**: p. 1-4.

18. Wang, Y., Toshima, N., *Preparation of Pd-Pt Bimetallic Colloids with Controllable Core/Shell Structures.* Phys. Chem. B, 1997. **101**: p. 5301-5306.

19. Antoine, O., Bultel, Yann., Durand, R., *Oxygen reduction reaction kinetics and mechanism on platinum nanoparticles inside Nafion.* Electroanalytical Chemistry, 2001. **499**: p. 85-94.

20. Aulice Scibioh, M., Kim, S., Cho, E.A., Lim, T., Hong, S., Ha, H.Y., , *Pt-CeO2/C anode catalyst for direct methanol fuel cells.* Applied Catalysis B: Environmental, 2008. **84**: p. 773-782.

21. Huang, S., Ganesan, P., Park, S., Popov, B.N., *Development of a Titanium Dioxide-Supported Platinum Catalyst with Ultrahigh Stability for Polymer Electrolyte Membrane Fuel Cell Applications.* JACS, 2009. **131**: p. 13898-13899.

22. Watt-Smith, M.J., Friedrich, J.M., Rigby, S.P., Ralph, T.R., Walsh, F.C., *Determination of the electrochemically active surface area of Pt/C PEM fuel cell electrodes using different adsorbates.* Physical Chemistry B, 2008. **41**: p. 1-8.

23. Wei, H., Chen, M., Zou, Z., Li, Z., Zhang., Jin, S., You, D.J., Pak, C., Yang, H., *Oxygen reduction on Pd3Pt1 bimetallic nanoparticles highly loaded on different carbon supports.* Applied Catalysis B: Environmental, 2010. **97**: p. 347-353.

24. Che, M. and A.J. Tench, *Characterization and Reactivity of Mononuclear Oxygen Species on Oxide Surfaces.* Advances in Catalysis, 1982. **31**: p. 77.

25. Kuhn, J.N., Huang, W., Tsung, C., Zhang, Y., Somorjai, G.A., *Structure Sensitivity of Carbon-Nitrogen Ring Opening" Impact of Platinum Particle Size from below 1 to 5 nm upon Pyrrole Hydrogenation Product Slectivity over Monodisperse Platinum Nanoparticles Loaded onto Mesoporous Silica.* JACS Communications, 2008. **130**: p. 14026-14027.

26. Tsung, C., Kuhn, J.N., Huang, W., Aliaga, C., Somorjai, G.A., Yang, P., *Sub-10 nm Platinum Nanocrystals with Size and Shape Control: Catalytic Study for Ethylene and Pyrrole Hydrogenation.* JACS, 2009. **131**: p. 5816-5822.

27. Zhang, Y., Grass, M.E., Habas, S.E., Tao, F., Zhang, T., Yang, P., Somorjai, G.A., *One-step Polyol Synthesis and Langmuir-Blodgett Monolayer Formation of Size-tunable Monodisperse Rhodium Nanocrystals with Catalytically Active (111) Surface Structures.* Physical Chemistry C, 2007. **111**: p. 12243-12253.

28. Sau, T.K., Rogach, A.L., *Nonspherical Noble Metal Nanoparticles: Colloid-Chemical Synthesis and Morphology Control.* Advanced Materials, 2010. **22**: p. 1781-1804.

29. Markovic, N., H.A. Gasteiger, and R.N. Ross Jr., *Oxygen Reduction on Platinum Low-Index Single-Crystal Surfaces in Sulfuric Acid Solution: Rotating Ring-Pt(hkZ) Disk Studies.* The Journal of Physical Chemistry, 1995. **99**(11): p. 3411-3415.

30. Gasteiger, H.A., S.S. Kocha, B. Sompalli, and F.T. Wangner, *Activity benchmarks and requirements for Pt, Pt-alloy, and non-Pt oxygen reduction catalysts for PEMFCs.* Applied Catalysis B: Environmental, 2005. **56**: p. 9-35.

31. Norskov, J., Rossmeisl, J., Logadottir, A., Lindqvist, L., *Origin of the Overpotential for Oxygen Reduction at a Fuel Cell Cathode.* Physical Chemistry B, 2004. **108**: p. 17886-17892.

32. Lee, Y.W., Kim, M., Han, S.W., *Shaping Pd nanocatalysts through the control of reaction sequence.* Chem Comm., 2009. **46**: p. 1535-1537.

33. Niu, W., Zhang, L., Xu, G, *Shape-controlled Synthesis of Single Crystalline Palladium Nanocrystals.* ACS Nano, 2010. **4**: p. 1987-1996.

34. Niu, Z., Peng, Q., Gong, M., Rong, H., Li, Y, *Oleylamine-Mediated Shape Evolution of Palladium Nanocrystals.* Angew. Chem. Int. Ed., 2011. **50**: p. 6315 - 6319.

35. Yancey, D.F., Carino, E.V., Crooks, R.M., *Electrochemical Synthesis and Electrocatalytic Properties of Au@Pt Dendrimer-Encapsulated Nanoparticles.* JACS Comm., 2010. **132**: p. 10988-10989.

36. Ye, H., J.A. Crooks, and R.M. Crooks, *Effect of Particle Size on the Kinetics of the Electrocatalytic Oxygen Reduction Reaction Catalyzed by Pt Dendrimer-Encapsulated Nanoparticles.* Langmuir, 2007. **23**: p. 11901-11906.

37. Ye, H. and R.M. Crooks, *Electrocatalytic O2 Reduction at Glassy Carbon Electrodes Modified with Dendrimer-Encapsulated Pt Nanoparticles.* JACS, 2005. **127**(13): p. 4.

38. Ye, H. and R.M. Crooks, *Effect of Elemental Composition of PtPd Bimetallic Nanoparticles Containing an Average of 180 Atoms on the Kinetics of the Electrochemical Oxygen Reduction Reaction.* JACS, 2007. **129**: p. 3627-3633.

39. Au, L., Y. Chen, F. Zhou, P. Camargo, B. Lim, Z.-Y. Li, D. Ginger, and Y. Xia, *Synthesis and optical properties of cubic gold nanoframes.* Nano Research, 2008. **1**(6): p. 441-449.

40. Chen, J., B. Wiley, J. McLellan, Y. Xiong, Z.-Y. Li, and Y. Xia, *Optical Properties of Pd−Ag and Pt−Ag Nanoboxes Synthesized via Galvanic Replacement Reactions.* Nano Letters, 2005. **5**(10): p. 2058-2062.

41. Cobley, C.M., D.J. Campbell, and Y. Xia, *Tailoring the Optical and Catalytic Properties of Gold-Silver Nanoboxes and Nanocages by Introducing Palladium.* Advanced Materials, 2008. **20**(4): p. 748-752.

42. Fan, F.-R., D.-Y. Liu, Y.-F. Wu, S. Duan, Z.-X. Xie, Z.-Y. Jiang, and Z.-Q. Tian, *Epitaxial Growth of Heterogeneous Metal Nanocrystals: From Gold Nano-octahedra to Palladium and Silver Nanocubes.* Journal of the American Chemical Society, 2008. **130**(22): p. 6949-6951.

43. Lim, B., M. Jiang, P.H.C. Camargo, E.C. Cho, J. Tao, X. Lu, Y. Zhu, and Y. Xia, *Pd-Pt Bimetallic Nanodendrites with High Activity for Oxygen Reduction.* Science, 2009. **324**: p. 1302-1305.

44. Blavo, S.O., E. Qayyum, L.M. Baldyga, V.A. Castillo, M.D. Sanchez, K. Warrington, M.A. Barakat, and J.N. Kuhn, *Verification of Organic Capping Agent Removal from Supported Colloidal Synthesized Pt Nanoparticle Catalysts.* Topics in Catalysis, 2012. **Accepted**.

45. Kitchin, J.R., Norskov, J.K., Barteau, M.A., Chen, J.G., *Role of Strain and Ligand Effects in the Modification of the Electronic and Chemical Properties of Bimetallic Surfaces.* Phys. Rev. Lett., 2004. **93**(15): p. 156801-156805.

46. Nilekar, A., Y. Xu, J. Zhang, M. Vukmirovic, K. Sasaki, R. Adzic, and M. Mavrikakis, *Bimetallic and Ternary Alloys for Improved Oxygen Reduction Catalysis.* Topics in Catalysis, 2007. **46**(3): p. 276-284.

47. Strasser, P., Koh, S., Anniyev, T., Greeley, J., More, K., Yu, C., Liu, Z., Kaya, S., Nordlund, D., Ogasawara, H., Toney, M.F., *Lattice-strain control of the activity in dealloyed core–shell fuel cell catalysts.* Nature Chemistry, 2010. **2**: p. 454-460.

48. Feng, Y.Y., Zhang, G., Ma, J., Liu, G., Xu, B., *Carbon-supported Pt^Ag nanostructures as cathode catalysts for oxygen reduction reaction.* Phys.Chem. Chem. Phys., 2011. **13**: p. 3863-3872.

49. Stamenkovic, V., B.S. Mun, K.J.J. Mayrhofer, R.N. Ross, N.M. Markovic, J. Rossmeisl, J. Greeley, and J.K. Norskov, *Changing the Activity of Electrocatalysts for Oxygen Reduction by Tuning the Surface Electronic Structure.* Angewandte Chemie International Edition, 2006. **45**: p. 2897 –2901.

50. Blavo, S., Baldyga, L., Sanchez, M., Kuhn, J.N., *The Effect of Stabilizing Agent on Platinum Nanoparticles and Implications Towards the Oxygen Reduction Reaction.* ASTM Int., 2011. **8**(9).

51. Tao, A.R., S. Habas, and P. Yang, *Shape Control of Colloidal Metal Nanocrystals.* Small, 2008. **4**(3): p. 310-325.

52. Baldyga, L.M., S.O. Blavo, C.-H. Kuo, C.-K. Tsung, and J.N. Kuhn, *Size-Dependent Sulfur Poisoning of Silica-Supported Monodisperse Pt Nanoparticle Hydrogenation Catalysts.* ACS Catalysis, 2012. **2**(12): p. 2626-2629.

53. Hokenek, S., *Structured Materials for Catalytic and Sensing Applications.* Doctoral Dissertation, 2013.

54. Garsany, Y., Baturina, O.A., Swider-Lyons, K., Kocha, S.S., *Experimental Methods for Quantifying the Activity of Platinum Electrocatalysts for the Oxygen Reduction Reaction.* Analytical Chemistry, 2010. **82**: p. 6321-6328.

55. Vasiliki Fragkou, Yi Ge, Greg Steiner, Dom Freeman, Norbert Bartetzko, and A.P.F. Turner, *Determination of the Real Surface Area of a Screen-Printed Electrode by Chronocoulometry.* Int. J. Electrochem. Sci.,, 2012(7): p. 6.

56. Bartholomew, C.h. and R.J. Farrauto, *Fundamentals of industrial catalytic processes*. 2nd ed2006: John Wiley & Sons.

57. Lu, C.-L., K.S. Prasad, H.-L. Wu, J.-a.A. Ho, and M.H. Huang, *Au Nanocube-Directed Fabrication of Au−Pd Core−Shell Nanocrystals with Tetrahexahedral, Concave Octahedral, and Octahedral Structures and Their Electrocatalytic Activity.* Journal of the American Chemical Society, 2010. **132**(41): p. 14546-14553.

58. Tian, N., Z.-Y. Zhou, N.-F. Yu, L.-Y. Wang, and S.-G. Sun, *Direct Electrodeposition of Tetrahexahedral Pd Nanocrystals with High-Index Facets and High Catalytic Activity for Ethanol Electrooxidation.* Journal of the American Chemical Society, 2010. **132**(22): p. 7580-7581.

59. Cherevko, S., N. Kulyk, and C.-H. Chung, *Nanoporous palladium with sub-10 nm dendrites by electrodeposition for ethanol and ethylene glycol oxidation.* Nanoscale, 2012. **4**(1): p. 103-105.

60. Yang, S.-D., C.-M. Shen, H. Tong, W. He, X.-G. Zhang, and H.-J. Gao, *Highly dispersed Pd nanoparticles on chemically modified graphene with aminophenyl groups for formic acid oxidation.* Chinese Physics B, 2011. **20**(11): p. 113301.

61. *Fuel Cell Science: Theory, Fundamentals, and Biocatalysis*. Electrocatalysis and electrochemistry, ed. A. Wieckowski2010, Hoboken, NJ: John Wiley &Sons.

62. *Fuel Cell Catalysis: A Surface Science Approach*. Electrocatalysis and Electrochemistry, ed. A. Wieckowski2009: John Wiley & Sons.

63. Convert, P., C. Coutanceau, P. Crouïgneau, F. Gloaguen, and C. Lamy, *Electrodes modified by electrodeposition of CoTAA complexes as selective oxygen cathodes in a direct methanol fuel cell.* J. App. Electrochem., 2001. **31**(9): p. 945-952.

64. Bard, A.J. and L. Faulkner, R, *Electrochemical Methods*1980: John Wiley & sons.

65. Bagotsky, V.S., *Fundamentals of Electrochemistry*. 2nd ed2005: John wiley & Sons.

66. Sheng, W., S. Chen, E. Vescovo, and Y. Shao-Horn, *Size Influence on the Oxygen Reduction Reaction Activity and Instability of Supported Pt Nanoparticles.* J. Electrochem. Soc., 2012. **159**(2): p. 7.

67. Matter, P.H., L. Zhang, and U.S. Ozkan, *The role of nanostructure in nitrogen-containing carbon catalysts for the oxygen reduction reaction.* Journal of Catalysis, 2006. **239**: p. 83.

68. Bashyam, R. and P. Zelenay, *A class of non-precious metal composite catalysts for fuel cells.* Nature, 2006. **443**: p. 63-66.

69. Lefèvre, M., E. Proietti, F. Jaouen, and J.-P. Dodelet, *Iron-Based Catalysts with Improved Oxygen Reduction Activity in Polymer Electrolyte Fuel Cells.* Science, 2009. **324**: p. 71-74.

70. Winther-Jensen, B., O. Winther-Jensen, M. Forsyth, and D.R. MacFarlane, *High Rates of Oxygen Reduction over a Vapor Phase–Polymerized PEDOT Electrode* Science, 2008. **321**: p. 671-674.

71. Matter, P.H. and U.S. Ozkan, *Non-metal catalysts for dioxygen reduction in an acidic electrolyte.* Catalysis Letters, 2006. **109**(3-4): p. 115.

72. Biddinger, E.J., D. von Deak, and U.S. Ozkan, *Nitrogen-Containing Carbon Nanostructures as Oxygen-Reduction Catalysts.* Topics in Catalysis, 2009. **52**: p. 1566–1574.

73. Biddinger, E.J. and U.S. Ozkan, *Role of Graphitic Edge Plane Exposure in Carbon Nanostructures for Oxygen Reduction Reaction.* Journal of Physical Chemistry C, 2010. **114**: p. 15306–15314.

74. Greeley, J., E.L. Stephens, A.S. Bondarenko, T.P. Johansson, H.A. Hansen, T.F. Jaramillo, J. Rossmeisl, I. Chorkendorff, and J.K. Norskov, *Alloys of platinum and early transition metals as oxygen reduction electrocatalysts.* Nature Chemistry, 2009. **1**: p. 552-556.

75. Stamenkovic, V.R., B.S. Mun, M. Arenz, K.J.J. Mayrhofer, C.A. Lucas, G. Wang, P.N. Ross, and N.M. Markovic, *Trends in electrocatalysis on extended and nanoscale Pt-bimetallic alloy surfaces.* Nature Materials, 2007. **6**: p. 241-247.

76. Stamenkovic, V.R., B. Fowler, B.S. Mun, G. Wang, R.N. Ross, C.A. Lucas, and N.M. Markovic, *Improved Oxygen Reduction Activity on Pt3Ni(111) via Increased Surface Site Availability.* Science, 2007. **315**: p. 493-497.

77. Zhang, J., K. Sasaki, E. Sutter, and R.R. Adzic, *Stabilization of Platinum Oxygen-Reduction Electrocatalysts Using Gold Clusters.* Science, 2007. **315**: p. 220-222.

78. Gasteiger, H.A. and N.M. Markovic, *Just a Dream—or Future Reality?* Science, 2009. **324**: p. 48-49.

79. Tang, L., B. Han, K. Persson, C. Friesen, T. He, K. Sieradzki, and G. Ceder, *Electrochemical Stability of Nanometer-Scale Pt Particles in Acidic Environments.* Journal of American Chemical Society, 2010. **132**: p. 596–600.

80. Tao, A.R., S.E. Habas, and P. Yang, *Shape Control of Colloidal Metal Nanocrystals.* Small, 2008. **4**: p. 310-325.

81. Zhang, Y., M.E. Grass, S.E. Habas, F. Tao, T. Zhang, P. Yang, and G.A. Somorjai, *One-step Polyol Synthesis and Langmuir-Blodgett monolayer Formation of Size-tunable Monodisperse Rhodium Nanocrystals with Catalytically Active (111) Surface Structures.* Journal of Physical Chemistry C, 2007. **111**: p. 12243-12253.

82. Zhang, Y., M.E. Grass, W. Huang, and G.A. Somorjai, *Seedless Polyol Synthesis and CO Oxidation Activity of Monodisperse (111)- and (100)-Oriented Rhodium Nanocrystals in Sub-10 nm Sizes.* Langmuir, 2010. **26**: p. 16463–16468.

83. Zhang, Y., M.E. Grass, J.N. Kuhn, F. Tao, S.E. Habas, W. Huang, P. Yang, and G.A. Somorjai, *Highly Selective Synthesis of Catalytically Active Monodisperse Rhodium Nanocubes.* Journal of American Chemical Society, 2008. **130**: p. 5868-5869.

84. Tsung, C.-K., J.N. Kuhn, W. Huang, C. Aliaga, L.-I. Hung, G.A. Somorjai, and P. Yang, *Sub-10 nm Platinum Nanocrystals with Size and Shape Control: Catalytic Study for Ethylene and Pyrrole Hydrogenation.* Journal of American Chemical Society, 2009. **131**(16): p. 5817-5822.

85. Huang, W., J.N. Kuhn, C.-K. Tsung, Y. Zhang, S.E. Habas, P. Yang, and G.A. Somorjai, *Dendrimer Templated Synthesis of One Nanometer Rh and Pt Particles Supported on Mesoporous Silica: Catalytic Activity for Ethylene and Pyrrole Hydrogenation.* Nano Letters, 2008. **8**(7): p. 2027-2034.

86. Witham, C.A., W. Huang, C.-K. Tsung, J.N. Kuhn, G.A. Somorjai, and F.D. Toste, *Converting homogeneous to heterogeneous in electrophilic catalysis using monodisperse metal nanoparticles.* Nature Chemistry, 2010. **2**: p. 36-41.

87. Li, Y. and M.A. El-Sayed, *The Effect of Stabilizers on the Catalytic Activity and Stability of Pd Colloidal Nanoparticles in the Suzuki Reactions in Aqueous Solution.* J. Phys. Chem. B, 2001. **105**: p. 8938-8943.

88. Narayanan, R. and M.A. El-Sayed, *Some Aspects of Colloidal Nanoparticle Stability, Catalytic Activity, and Recycling Potential.* Top. Catal., 2008. **47**: p. 15-21.

89. Kuhn, J.N., C.-K. Tsung, W. Huang, and G.A. Somorjai, *Effect of organic capping layers over monodisperse platinum nanoparticles upon activity for ethylene hydrogenation and carbon monoxide oxidation.* Journal of Catalysis, 2009. **265**: p. 209-215.

90. Huang, S.-Y., P. Ganesan, S. Park, and B.N. Popov, *Development of a Titanium Dioxide-Supported Platinum Catalyst with Ultrahigh Stability for Polymer Electrolyte Membrane Fuel Cell Applications.* Journal of American Chemical Society, 2009. **131**: p. 13898–13899.

91. Matsumori, H., S. Takenaka, H. Matsune, and M. Kishida, *Preparation of carbon nanotube-supported Pt catalysts covered with silica layers; application to cathode catalysts for PEFC.* Applied Catalysis A: General, 2010. **373**: p. 176–185.

92. Takenaka, S., N. Susuki, H. Miyamoto, E. Tanabe, H. Matsunea, and M. Kishida, *Highly durable Pd metal catalysts for the oxygen reduction reaction in fuel cells; coverage of Pd metal with silica.* Chemical Communications, 2010. **46**: p. 8950-8952.

93. Takenaka, S., A. Hirati, E. Tanabe, H. Matsune, and M. Kishida, *Preparation of supported Pt–Co alloy nanoparticle catalysts for the oxygen reduction reaction by coverage with silica.* Journal of Catalysis, 2010. **274**: p. 228-238.

94. Jeyabharathi, C., P. Venkateshkumar, J. Mathiyarasu, and K.L.N. Phani, *Carbon-Supported Palladium–Polypyrrole Nanocomposite for Oxygen Reduction and Its Tolerance to Methanol.* Journal of the Electrochemical Society, 2010. **157**: p. B1740-B1745

95. Seo, M.H., E.J. Lim, S.M. Choi, H.J. Kim, and W.B. Kim, *Stability Enhancement of Pd Catalysts by Compositing with Polypyrrole Layer for Polymer Electrolyte Fuel Cell Electrodes.* Topics in Catalysis, 2010. **53**: p. 678–685.

96. Ledesma-Garcia, J., I.L. Escalante-Garcia, T.W. Chapman, L.G. Arriaga, V. Baglio, V. Antonucci, A.S. Aricò, R. Ornelas, and L.A. Godinez, *Pt dendrimer nanocomposites for oxygen reduction reaction in direct methanol fuel cells.* Journal of Solid State Electrochemistry, 2010. **14**: p. 835.

97. Zhang, G.-R. and B.-Q. Xu, *Surprisingly strong effect of stabilizer on the properties of Au nanoparticles and Pt^Au nanostructures in electrocatalysis.* Nanoscale, 2010. **2**: p. 2798–2804.

98. Borodko, Y., H.S. Lee, S.H. Joo, Y. Zhang, and G.A. Somorjai, *Spectroscopic Study of the Thermal Degradation of PVP-Capped Rh and Pt Nanoparticles in H2 and O2 Environments.* Journal of Physical Chemistry C, 2010. **114**: p. 1117–1126.

99. Borodko, Y., S.E. Habas, M.M. Koebel, P. Yang, H. Frei, and G.A. Somorjai, *Probing the Interaction of Poly(vinylpyrrolidone) with Platinum Nanocrystals by UV-Raman and FTIR.* Journal of Physical Chemistry B, 2006. **110**: p. 23052-23059.

100. Borodko, Y., S.M. Humphrey, T.D. Tilley, H. Frei, and G.A. Somorjai, *Charge-Transfer Interaction of Poly(vinylpyrrolidone) with Platinum and Rhodium Nanoparticles.* Journal of Physical Chemistry C, 2007. **111**: p. 6288-6295.

101. Borodko, Y., S.E. Habas, M.M. Koebel, P. Yang, H. Frei, and G.A. Somorjai, *Probing the Interaction of Poly(vinylpyrrolidone) with Platinum Nanocrystals by UV-Raman and FTIR.* J. Phys. Chem. B, 2006. **110**: p. 23052-23059.

102. Jolly, W.L., *Modern Inorganic Chemistry*1989, New York: McGraw-Hill book Company.

103. Bing, Y., Liu, H., Zhang, H., Ghosh, D., Zhang, J., *Nanostructured Pt-alloy electrocatalysts for PEM fuel cell oxygen reduction reaction.* Chemical Society Reviews, 2010. **39**: p. 2184-2202.

104. Fernandez, J.L., J.M. White, Y. Sun, W. Tang, G. Henkelman, and A.J. Bard, *Characterization and Theory of Electrocatalysts Based on Scanning Electrochemical Microscopy Screening Methods.* Langmuir, 2006. **22**: p. 10426-10431.

105. Shao, M.H., K. Sasaki, and R.R. Adzic, *Pd-Fe Nanoparticles as Electrocatalysts for Oxygen Reduction.* Journal of American Chemical Society, 2006. **128**: p. 3526-3527.

106. Greeley, J. and J.K. Norskov, *Combinatorial Density Functional Theory-Based Screening of Surface Alloys for the Oxygen Reduction Reaction.* Journal of Physical Chemistry C, 2009. **113**: p. 4932–4939.

107. Norskov, J.K., T. Bligaard, J. Rossmeisl, and C.H. Christensen, *Towards the computational design of solid catalysts.* Nature Chemistry, 2009. **1**: p. 37-46.

108. Hammer, B., Norskov, J.K., *Theoretical Surface Science and Catalysis—Calculations and Concepts.* Advances in Catalysis, 2000. **45**: p. 71-129.

109. Nillson, A., Pettersson, L.G.M., Hammer, B., Bligaard, T., Christensen, C.H., Norskov, J.K., *The electronic structure effect in heterogeneous catalysis.* Catalysis Letters, 2005. **100**: p. 111-114.

110. Nørskov, J.K., J. Rossmeisl, A. Logadottir, L. Lindqvist, J.R. Kitchin, T. Bligaard, and H. Jonsson, *Origin of the Overpotential for Oxygen Reduction at a Fuel-Cell Cathode.* Journal of Physical Chemistry B, 2004. **108**: p. 17886-17892.

111. Markovic, N.M., Gasteiger, H.A., Ross, P.N., *Oxygen Reduction on Platinum Low-Index Single-Crystal Surfaces in Sulphuric Acid Solution: Rotating Ring-Pt(hkl) Disk Studies.* The Journal of Physical Chemistry, 1995. **99**: p. 3411-3415.

112. Hughes, R., *Composite palladium membranes for catalytic membrane reactors.* Membrane Technology, 2001. **2001**(131): p. 9-13.

113. Tong, H.D., A.H.J. vanden Berg, J.G.E. Gardeniers, H.V. Jansen, F.C. Gielens, and M.C. Elwenspoek, *Preparation of palladium–silver alloy films by a dual-sputtering technique and its application in hydrogen separation membrane.* Thin Solid Films, 2005. **479**(1–2): p. 89-94.

114. Wolfe, R.J., M.W. Lee, and R.C. Davis, *Pressure-composition isotherms for palladium hydride.* Physical Review B, 1993. **48**(17): p. 12415-12418.

115. Cortright, R.D., S.A. Goddard, J.E. Rekoske, and J.A. Dumesic, *Kinetic Study of Ethylene Hydrogenation.* J. Catal., 1991. **127**: p. 342-353.

116. Grunes, J., J. Zhu, E.A. Anderson, and G.A. Somorjai, *Ethylene Hydrogenation over Platinum Nanoparticle Array Model Catalysts Fabricated by Electron Beam Lithography: Determination of Active Metal Surface Area.* J. Phys. Chem. B, 2002. **106**: p. 11463-11468.

117. Moula, M.G., S. Wako, M.U. Kislyuk, Y. Ohno, and T. Matsushima, *Structure Sensitivity in Reactive Carbon Dioxide Desorption on Palladium Surfaces.* Studies in Surface Science and Catalysis, 2001. **132**: p. 701-704.

118. Cremer, P.S. and G.A. Somorjai, *Surface Science and Catalysis of Ethylene Hydrogenation.* J. CHEM. SOC. FARADAY TRANS., 1995. **91**: p. 3671-3677.

119. Cremer, P.S., X. Su, Y.R. Shen, and G.A. Somorjai, *Ethylene Hydrogenation on Pt(111) Monitored in Situ at High Pressures Using Sum Frequency Generation.* J. Am. Chem. Soc., 1996. **118**: p. 2942-2949.

120. Ravel, B. and M. Newville, *ATHENA, ARTEMIS, HEPHAESTUS: data analysis for X-ray absorption spectroscopy using IFEFFIT.* Journal of Synchrotron Radiation, 2005. **12**: p. 537–541.

121. Newville, M., *IFEFFIT: interactive XAFS analysis and FEFF fitting.* Journal of Synchrotron Radiation, 2001. **8**: p. 322-324.

122. Shao, M., J.H. Odell, S.-I. Choi, and Y. Xia, *Electrochemical surface area measurements of platinum- and palladium-based nanoparticles.* Electrochemistry Communications, 2013. **31**: p. 3.

123. Flanagan, T.B. and W.A. Oates, *The Palladium-Hydrogen System.* Annual Review of Material Science, 1991. **21**: p. 269-304.

124. Castillo, V.A. and J.N. Kuhn, *Role of the Ni:Fe Ratio in Ethylene Hydrogenation Activity for Silica-Supported Ni–Fe Clusters Prepared by Dendrimer-Templating.* The Journal of Physical Chemistry C, 2012. **116**(15): p. 8627-8633.

125. Mankbadi, M.R., M.A. Barakat, M.H. Ramadan, H.L. Woodcock, and J.N. Kuhn, *Iron Chelation by Polyamidoamine Dendrimers: A Second-Order Kinetic Model for Metal–Amine Complexation.* The Journal of Physical Chemistry B, 2011. **115**(46): p. 13534-13540.

126. Ye, H. and R.M. Crooks, *Effect of Elemental Composition of PtPd Bimetallic Nanoparticles Containing an Average of 180 Atoms on the Kinetics of the Electrochemical Oxygen Reduction Reaction.* Journal of American Chemical Society, 2007. **129**: p. 3627-3633.

127. Hokenek, S., *Structured Materials for Catalytic and Sensing Applications.* Dissertation Manuscript, 2013.

128. Blizanac, B.B., R.N. Ross Jr., and N. Markovic, *Oxygen Reduction on Silver Low-Index Single-Crystal Surfaces in Alkaline Solution: Rotating Ring DiskAg(hkl) Studies.* J.Phys. Chem B, 2006. **110**: p. 6.

129. Blizanac, B.B., P.N. Ross, and N.M. Markovic, *Oxygen electroreduction on Ag(1 1 1): The pH effect.* Electrochimica Acta, 2007. **52**(6): p. 2264-2271.

130. Singh, P. and D.A. Buttry, *Comparison of Oxygen Reduction Reaction at Silver Nanoparticles and Polycrystalline Silver Electrodes in Alkaline Solution.* J. pHys. Chem. C, 2012. **116**: p. 7.

131. Skrabalak, S.E., J. Chen, Y. Sun, X. Lu, L. Au, C.M. Cobley, and Y. Xia, *Gold Nanocages: Synthesis, Properties, and Applications.* ACCOUNTS OF CHEMICAL RESEARCH, 2008. **41**(12): p. 1587-1595.

132. Cheong, S., Watt, J., Tilley, R., *Shape control of platinum and palladium nanoparticles for catalysis.* Nanoscale, 2010. **2**: p. 2045-2053.

133. Halder, A., Kundu, P., Viswanath, B., Ravishankar, N., *Symmetry and shape issues in nanostructure growth.* Materials Chemistry, 2010. **20**: p. 4763-4772.

134. Hu, B., Ding, K., Wu, T., Zhou, X., Fan, H., Jiang, T., Wang, Q., Han, B., *Shape controlled synthesis of palladiun nanocrystals by combination of oleyamine and alkylammonium alkylcarbamate and their catalytic activity.* Chemical Communications, 2010. **46**: p. 8552-8554.

135. Komanicky, V., Iddir, H., Chang, K., Menzel, A., Karapetrov, G., Hennessy, D., Zapol, P., You, H., *Shape-dependent activity of Platinum array Catalyst.* JACS Communications, 2009. **131**: p. 5732-5733.

136. Subhramannia, M., Pillai, V.K., *Shape-dependent electrocatalytic activity of platinum nanostructures.* Materials Chemistry, 2008. **18**: p. 5858-5870.

137. Zhang, L., W. Niu, and G. Xu, *Seed-mediated growth of palladium nanocrystals: The effect of pseudo-halide thiocyanate ions.* Nanoscale, 2011. **3**(2): p. 678-682.

138. Fernandez, J., Walsh, D.A., Bard, A., *Thermodynamic Guidelines for the design of bimetallic catalysts for Oxygen Electroreduction and Rapid Screening by Scaning Electrochemical Microscopy.* JACS, 2005: p. 357-365.

139. Guo, S., Dong, S., Wang, E., *Three-Dimensional Pt-on-Pd Bimetallic Nanodendrites Supported on Graphene Nanosheet: Facile Synthesis and Used as an Advanced Nanoelectrocatalyst for Methanol Oxidation.* ACS Nano, 2010. **4**: p. 547-555.

140. He, W., X. Wu, J. Liu, X. Hu, K. Zhang, S. Hou, W. Zhou, and S. Xie, *Design of AgM Bimetallic Alloy Nanostructures (M = Au, Pd, Pt) with Tunable Morphology and Peroxidase-Like Activity.* Chemistry of Materials, 2010. **22**(9): p. 2988-2994.

141. Hunyadi, S. and C. Murphy, *Synthesis and Characterization of Silver–Platinum Bimetallic Nanowires and Platinum Nanotubes.* Journal of Cluster Science, 2009. **20**(2): p. 319-330.

142. Lim, B., Jiang, M., Camargo, P.H.C., Cho, E.C., Tao, J., Lu, X., Zhu, Y., Xia, Y., *Pd-Pt bimetallic nanodendrites with high activity for oxygen reduction.* Science, 2009. **324**: p. 1302-1305.

143. Lim, B., Kobayashi, H., Yu, T., Wang, J., Kim, M., Li, Z., Rycenga, M., Xia, Y., *Synthesis of Pd-Au bimetallic nanocrystals via controlled overgrowth.* JACS Communications, 2010. **132**: p. 2506-2507.

144. Peng, Z. and H. Yang, *Synthesis and Oxygen Reduction Electrocatalytic Property of Pt-on-Pd Bimetallic Heteronanostructures.* J. Am. Chem. Soc., 2009. **31**: p. 7542–7543.

145. Wang, W., D. Zheng, C. Du, S. Zou, X. Zhang, B. Xia, H. Yang, and D.L. Akins, *Carbon-supported Pd-Co bimetallic nanoparticles as electrocatalysts for the oxygen reduction reaction.* Journal of Power Sources, 2007. **167**: p. 243–249.

146. Zhu, H., S. Zhang, S. Guo, D. Su, and S. Sun, *Synthetic Control of FePtM Nanorods (M = Cu, Ni) To Enhance the Oxygen Reduction Reaction.* Journal of the American Chemical Society, 2013. **135**(19): p. 7130-7133.

147. Zhang, J., *PEM Fuel Cell Catalyst and Layers: Fundamentals and Applications*2008: Elsevier.

148. Poh, C.K., Z. Tian, J. Gao, Z. Liu, J. Lin, Y.P. Feng, and F. Su, *Nanostructured trimetallic Pt/FeRuC, Pt/NiRuC, and Pt/CoRuC catalysts for methanol electrooxidation.* Journal of Materials Chemistry, 2012. **22**(27): p. 13643-13652.

149. Wanjala, B.N., B. Fang, J. Luo, Y. Chen, J. Yin, M.H. Engelhard, R. Loukrakpam, and C.-J. Zhong, *Correlation between Atomic Coordination Structure and Enhanced Electrocatalytic Activity for Trimetallic Alloy Catalysts.* Journal of the American Chemical Society, 2011. **133**(32): p. 12714-12727.

150. Fang, B., B.N. Wanjala, J. Yin, R. Loukrakpam, J. Luo, X. Hu, J. Last, and C.-J. Zhong, *Electrocatalytic performance of Pt-based trimetallic alloy nanoparticle catalysts in proton exchange membrane fuel cells.* International Journal of Hydrogen Energy, 2012. **37**(5): p. 4627-4632.

151. Qi-Ling, N., N. Sivapregasen, P. Leslie, N. Alexander, N. Patrick, and V. Guntars, *Synthesis highly active platinum tri-metallic electrocatalysts using "one-step" organometallic chemical vapour deposition technique for methanol oxidation process.* IOP Conference Series: Materials Science and Engineering, 2012. **38**(1): p. 012031.

152. Arruda, T.M., Shyman, B., Ziegelbauer, J.M., Mukerjee, S., Ramaker, D.E., *Investigation into the competitive and site-specific nature of anion adsorption on Pt using in situ x-ray absorption spectroscopy.* Physical Chemistry C, 2008. **112**: p. 18087-18097.

153. Erickson, E.M., M.S. Thorum, R. Vasić, N.S. Marinković, A.I. Frenkel, A.A. Gewirth, and R.G. Nuzzo, *In Situ Electrochemical X-ray Absorption Spectroscopy of Oxygen Reduction Electrocatalysis with High Oxygen Flux.* Journal of the American Chemical Society, 2011. **134**(1): p. 197-200.

154. Friebel, D., Miller, D.J., O'Grady, C.P., Anniyev, T., Bargar, J., Bergman, U., Ogasawara, H., Wikfeldt, K.T., Pettersson, L.G.M., Nillson, Anders, *In situ X-ray probing reveals fingerprints of surface platinum oxide.* Physical Chemistry Chemical Physics, 2011. **13**: p. 262-266.

155. Grass, M.E., Y. Zhang, D.R. Butcher, J.Y. Park, Y. Li, H. Bluhm, K.M. Bratlie, T. Zhang, and G.A. Somorjai, *A Reactive Oxide Overlayer on Rhodium Nanoparticles during CO Oxidation and Its Size Dependence Studied by In Situ Ambient-Pressure X-ray Photoelectron Spectroscopy.* Angew. Chem. Int. Ed., 2008. **47**: p. 8893-8896.

156. Haubold, H.-G., P. Hiller, H. Jungbluth, and T. Vad, *Characterization of Electrocalatysts by in situ SAXS and XAS Investigations: Proc. Int. Conf. SRMS-2.* J. Appl. Phys., 1999. **38**: p. 3.

157. Kunimatsu, K., Yoda, T., Tryk, D.A., Uchida, H., Waanabe, M., *In situ ATR-FTIR study of oxygen reduction at the Pt/Nafion interface.* Physical Chemistry Chemical Physics, 2009. **12**: p. 621-629.

158. Price, S.W.T., J.D. Speed, P. Kannan, and A.E. Russell, *Exploring the First Steps in Core–Shell Electrocatalyst Preparation: In Situ Characterization of the Underpotential Deposition of Cu on Supported Au Nanoparticles.* Journal of the American Chemical Society, 2011. **133**(48): p. 19448-19458.

159. Zeng, D., Jiang, Y., Zhou, Z., Su, Z., Sun, S., *In situ FTIR spectroscopic studies of (bi)sulfate adsorption on electrodes of Pt nanoparticles supported on different substrates.* Electrochimica Acta, 2010. **55**: p. 2065-2072.

160. Shi, Z., X. Wang, and Z. Zhang, *Comparison of Two-Dimensional PEM Fuel Cell Modeling using COMSOL Multiphysics.* Excerpt from the Proceedings of the COMSOL Users Conference 2006: p. 9.

161. Mina, P., J. Pauchet, and P. Schott, *Computational Analysis of Transport Phenomena and Electrochemical Reactions in a Polymer-Electrolyte-Membrane Fuel Cell.* Excerpt from the Proceedings of the COMSOL Users Conference 2007: p. 7.

162. Robalinho, E., E.F. Cunha, A.B. Andrade, M.L.M. Bejarano, M. Linardi, and E. Cekinski, *COMSOL Modelling and Simulation of PEM Fuel Cell's Flow Channels.* Excerpt from the Proceedings of the COMSOL Conference, 2007: p. 7.

163. Vaivars, G., P. Ndungu, and V. Linkov, *Catalyst Degradation in PEM Fuel Cells – Modeling Aspects.* Excerpt from the Proceedings of the COMSOL Users Conference 2007: p. 5.

164. Cetinbas, F.C., P.K. Ajay, and S.G. Advani, *Modeling the effect of discrete distributions of Platinum particles in the PEM fuel cell catalyst layer*. Proceedings of COMSOL Conference, 2012(6).

APPENDICES

Appendix A List of Abbreviations and Chemical Formulae

Ag.....Silver
Ar .....Argon
Au.....Gold
Aq.....Aqueous
CTAB.....Cetyl Trimethylammonium Bromide
CV .....Cyclic Voltammetry
Cu.....Copper
DEN .....Dendrimer-Encapsulated metal Nanoparticle
DI .....De-ionized Water
DLR.....Double Layer Region
ECSA .....Electrochemical Surface Area
EXAFS.....Extended X-Ray Absorption Fine Structure
FC.....Fuel Cell
FIJI .....Fiji is just ImageJ
GC .....Gas Chromatrography
GCE.....Glassy Carbon Electrode
$HClO_4$.....Perchloric Acid
HER.....Hydrogen Evolution Region
H_2PtCl_6.....Hexachloroplatinic Acid
ICE .....Internal Combustion Engine
K_2PdCl_4.....Potassium Tetrachloropalladate (II)
K_2PtCl_4.....Potassium Tetrachloroplatinate (II)
K_2PdCl_6.....Potassium Hexachloropalladate (IV)
K_2PtCl_6.....Potassium Hexachloroplatinate (IV)
LSV .....Linear Sweep Voltammetry
Mo .....Molybdenum
MS.....Mass Spectroscopy
MW .....Molecular Weight
Ni.....Nickel
NIH .....National Institute of Health
NP(s) .....Nanoparticle(s)
OER.....Oxygen Evolution Region
ORR .....Oxygen Reduction Reaction
PAMAM-OH .Hydroxyl-terminated Polyamidoamine dendrimer
PEMFC .....Polymer Electrolyte Membrane Fuel Cell
Pd .....Palladium
Pt .....Platinum
PVP .....Polyvinyl Pyrrolidone
RE .....Reference Electrode
RPM/rpm.....Revolutions per minute
Ru .....Ruthenium

Appendix A (Continued)

SCE .....Saturated Calomel Electrode
SiO_2 .....Silicon Dioxide
TEM .....Transmission Electron Microscopy
TPO .....Temperature-Programmed Oxidation
VC .....Vulcan Carbon
XAS.....X-Ray Absorption Spectroscopy
XRD .....X-Ray Diffraction
W.....Tungsten

Appendix B Permission for Use of Material in Chapter 3

B.1 ASTM International

ASTM International
Author/Copyright Owner Agreement

Paper Title as submitted (the "Work")

For U.S. and foreign government employees *who have prepared this Work as a part of their official duties, it is understood that copyright is not available for assignment. This agreement must be accepted so as to agree to and acknowledge all other terms of this agreement.*

"You" means the Author(s) (and Copyright Owner(s), if different))

Author's Obligations. You have submitted the Work to ASTM for publication. You represent that the Work submitted has not been previously published. You promise that the Work is not currently under consideration by another publication. You warrant that the Work is original material (except for any material from copyrighted sources reproduced with the written permission of the copyright holder sufficient to permit ASTM to use the Work as contemplated), and is in no way a violation or an infringement of any copyright belonging to any third party; that the materials contained in the Work are accurate; and that the Work contains no defamatory or otherwise illegal materials.

You grant the following rights to ASTM: the worldwide and perpetual right to (a) print and/or electronically publish and distribute the Work (or portions thereof) in all versions of ASTM publications (in any language and with the right to translate), websites and/or newsletters and right to print and/or electronically publish and distribute the Work to other sites under license or contract with ASTM; (b) include the Work in advertising and promotion; (c) include the Work in print and non-print products anywhere in the world.

Corresponding Author: The corresponding author is the person with whom ASTM communicates. He/She is responsible for updating all co-authors regarding the status of the Work. The corresponding author is responsible for transferring copyright and has communicated the terms of ASTM copyright with co-authors prior to publication.

Electronically accepting this Agreement represents and warrants that you (and any co-authors) are the sole copyright holder(s) of the Work and that you have identified all co-authors to ASTM. You also represent that each of the co-author(s) have also granted permission to ASTM to use their name(s) in connection with any past, present, or future promotional activity by ASTM, including, but not limited to, promotions for upcoming issues or publications, circulation solicitations, advertising, or other publications in connection with the journal.

Compensation. You will not receive or be entitled to any royalty, fee, commission, payment or other compensation.

Copyright Assignment. It is ASTM's policy to require authors/copyright owners to assign the copyright in the submitted works, in order that ASTM may disseminate the Work to the fullest extent. You hereby assign all rights, including the copyright, in the

Appendix B (Continued)

Work to ASTM, prior to publication, by executing this Agreement. including but not limited to any and all copyright(s) therein held by each Author, together with any rights of each to secure renewals, reissues and extensions of copyright that may be secured under the laws now or hereafter in force and effect in the United States or in any other country, and any and all rights to enforce such copyright(s) or bring other claim in connection with such copyright.

The Work becomes the copyrighted property of ASTM and shall not be published anywhere without the prior written consent of ASTM. ***ASTM reserves the right of first publication of all papers offered for publication.***

The author(s), if different from the copyright owner(s) also represents that he/she/they prepared the Work within the scope of their employment, as a work-for-hire.

Peer Review Policy. All papers are subject to review by two anonymous peer reviewers, selected by the Journal Editor(s), as the process is described in ASTM's peer review process (copy will be provided upon request). Submission of Work does not in any way guarantee that ASTM will publish the Work.

Limited Right of Use by Author(s)' Employer. ASTM grants the authors' employer the limited and non-exclusive license to make a limited number of photocopies (hardcopy paper copies, specifically excluding any electronic copies) and circulate these copies within its company for internal purposes. Author(s)' employer acknowledges and will retain ASTM's copyright notice on each hardcopy it makes.

As the Author, ASTM permits you certain uses that do not require permission from ASTM. These include:

- The right to make copies of the Work for your own personal use, including for your own classroom teaching use;
- The right to make copies and distribute copies of the Work to research colleagues, for the personal use by such colleagues(but not commercially or systematically, e.g. via an email list or list serve);
- The right to post the pre-print version of the Work on your website or your employer's website with reference to the publication by ASTM as the copyright holder. Such preprints may be posted as electronic files on the Author's own website for personal or professional use, or on the Author's internal university or corporate networks/intranet, or secure external website at the Author's institution, but not for commercial sale or for any systematic external distribution by a third party (eg: a listserver or database connected to a public access server). Prior to publication, the Author must include the following notice on the preprint: "This is a preprint of an article accepted for publication in (Journal Title Copyright @ (year) (copyright owner as specified in the journal)". After publication of the Work by ASTM International, the preprint notice should be amended to read as follows: "This is a preprint of an article published in (include the complete

Appendix B (Continued)

citation information for the final version of the Work as published in the print edition of the Journal)" and should provide an electronic link to the Journal's WWW site, located at the following ASTM URL: http://www.astm.org. The Author agrees not to update the preprint or replace it with the published version of the Work;

- The right to present the Work at a meeting or conference and to distribute copies of such Work to the delegate attending the meeting after the Work is published by ASTM with appropriate citation to the published article;
- For the author's employer, if the Work is a "work for hire", made within the scope of the author's employment, the right to use all or part of the information in (any version of) the Work for other intra-company use (e.g., training);
- You retain any patent and trademark rights and rights to any process or procedure described in the Work ;
- The right to include the Work in full or in part in a thesis or dissertation (provided that this is not to be published commercially);
- The right to use the Work or any part thereof in a printed compilation of works of the author, such as collected writings or lecture notes (subsequent to publication of the Work by ASTM); and
- The right to prepare other derivative works, to the extent the Work is not book-length form, or to otherwise re-use portions or excerpts in other publications, with full acknowledgement of its original publication by ASTM.

Other uses by authors must be authorized in writing by ASTM.

By electronically accepting this Agreement, you agree to all the above terms and limitations.

July 2007

Appendix C Instruments Used

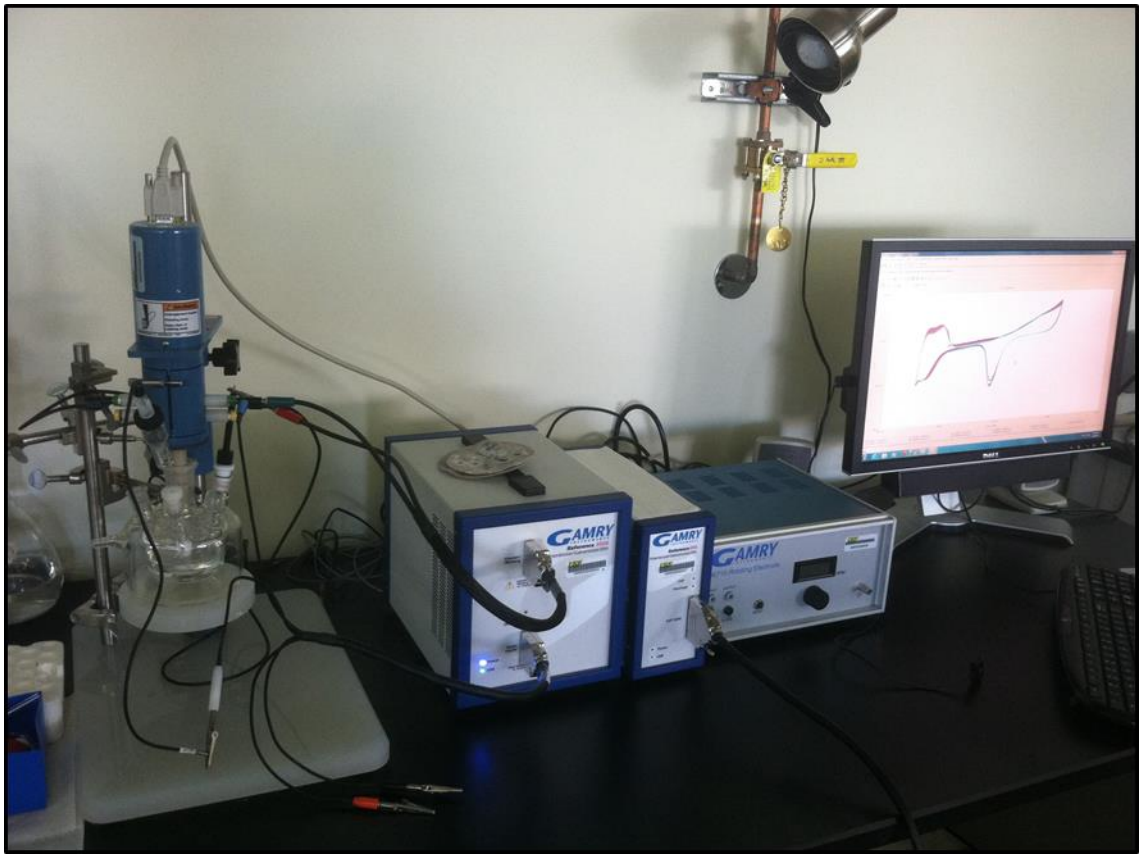

Figure C-1 Suite of GAMRY Instruments ® used to generate Cyclic Voltammetry and Linear sweep Voltammetry data. Included are (R – L): RDE710 Rotator, Reference 600 Potentiostat, Reference 3000 Potentiostat, Electrochemical Set-up including rotating working electrode in electrochemical reactor cell.

Appendix C (Continued)

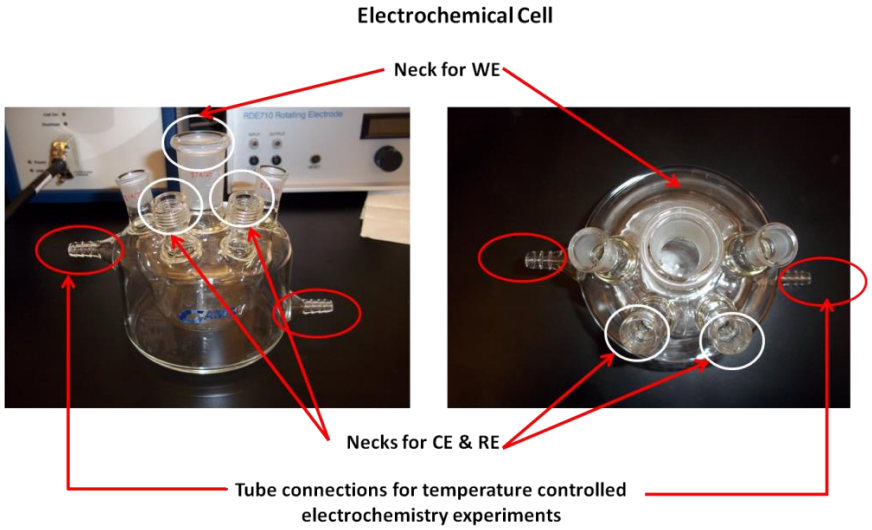

Figure C-2 Electrochemical Cell (Reactor)

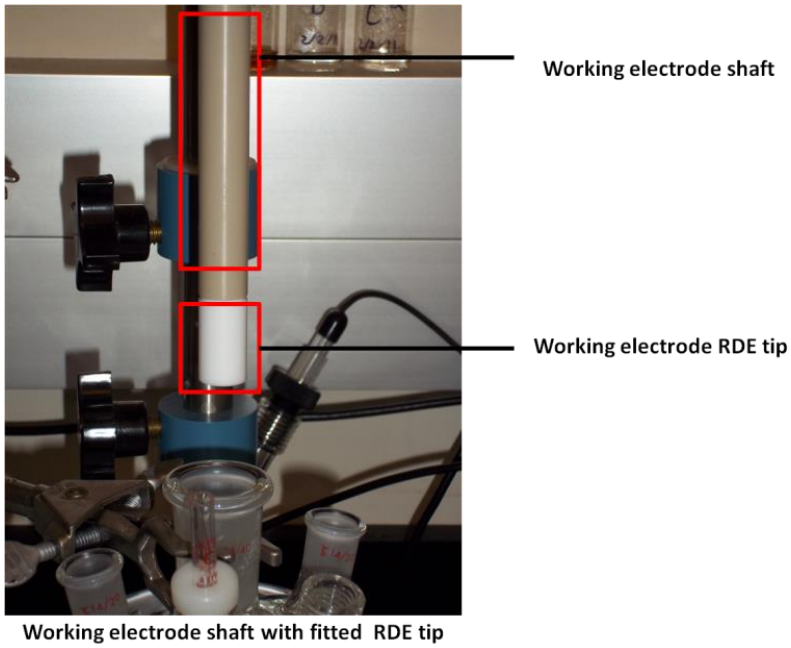

Figure C-3 Working Electrode Assembly

Appendix C (Continued)

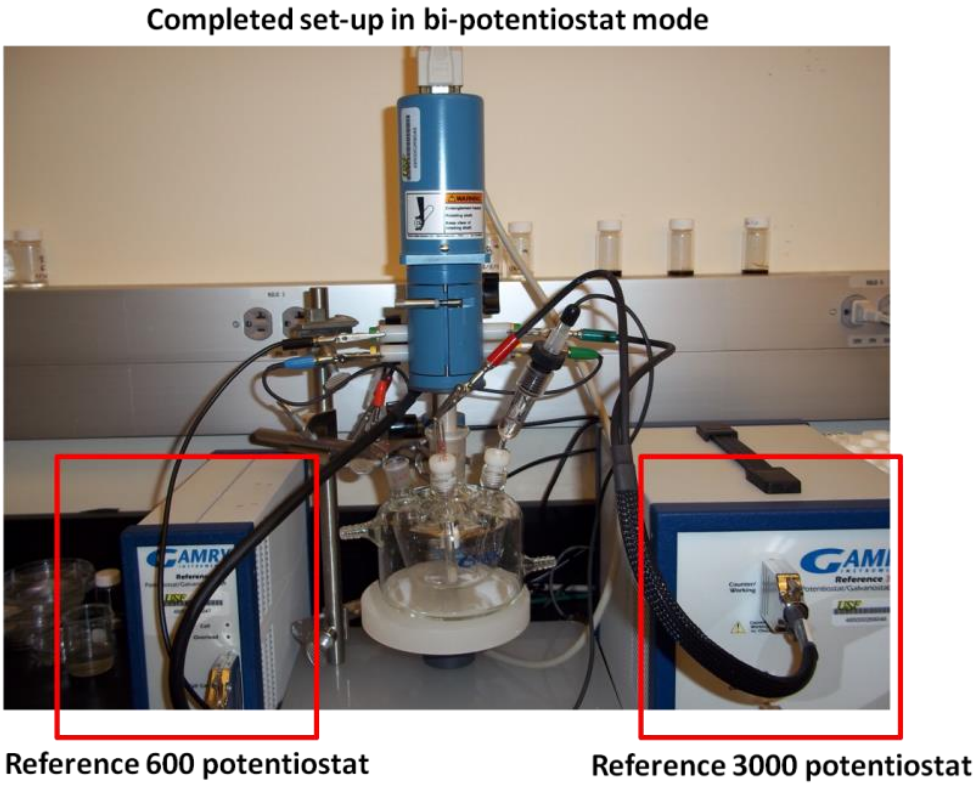

Figure C-4 Electrochemical System in Bi-Potentiostat mode

Figure C-5 Perkin Elmer (Gas Chromatograph) Set-Up

Appendix C (Continued)

Figure C-6 Quantachrome Autosorb IQ

Appendix D Calculating ECSA

A recorded CV set is saved and stored in the *My Gamry Data* Folder. From EChem analyst, it can be opened to look like the screen shot below.

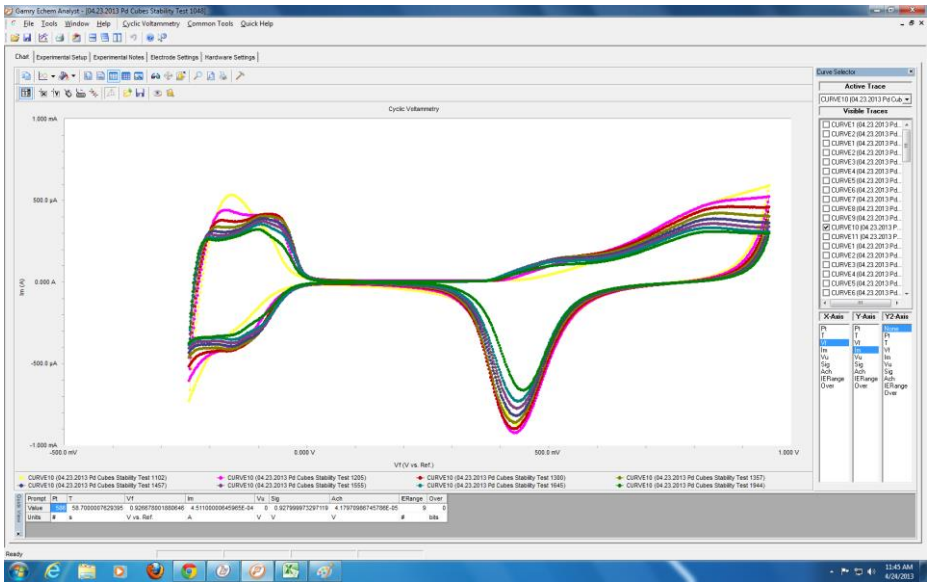

Figure D-1 EChem Analyst Screenshot of a series of Cyclic Voltammograms

From here, a single CV can be chosen for further analysis.

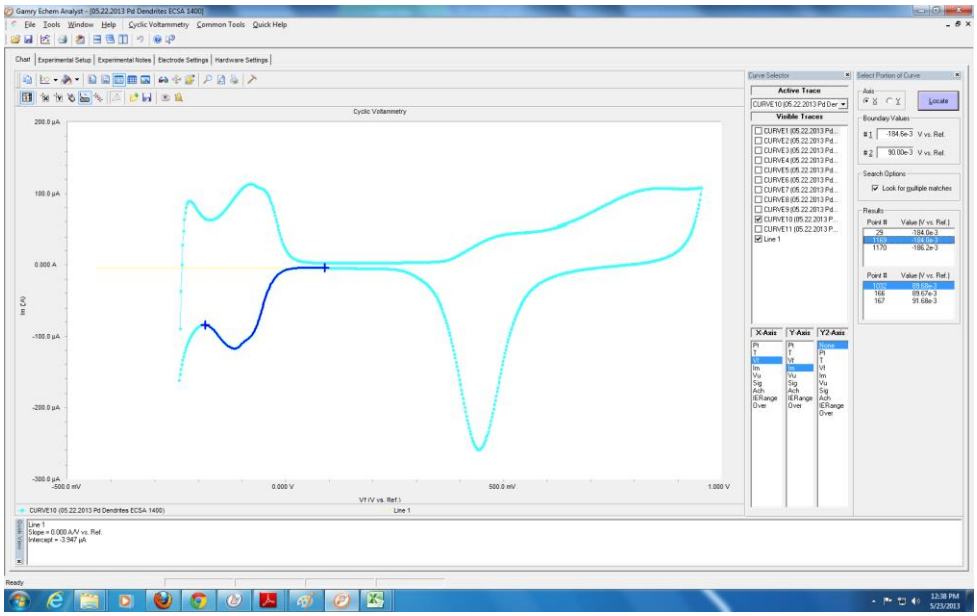

Figure D-2 EChem Analyst Screenshot of a single Cyclic Voltammogram with highlighted Hydrogen Evolution Region

Appendix D (Continued)

Using the keyboard tab, the desired span of the curve to integrate over can be chosen (see blue line above). To avoid over estimating, a line is used to designate the vertical limit / boundary of the integral.

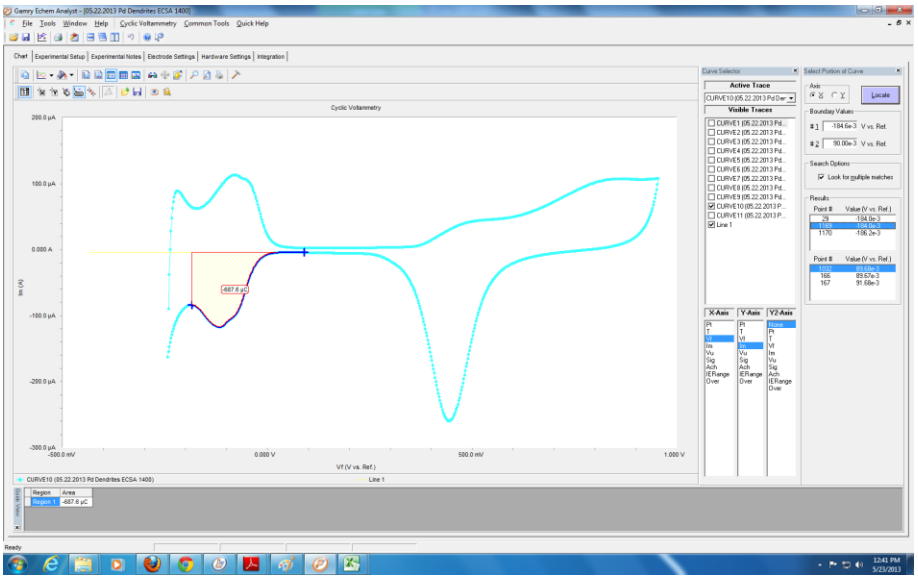

Figure D-3 EChem Analyst Screenshot of a single Cyclic Voltammogram with computationally integrated Hydrogen Evolution Region

The intersection of the curve and the line, establish the area of interest to integrate over. Under the Cyclic Voltammetry tab, the "integrate" button is chosen: This integration is performed using 0.0A as the vertical limit for the integration. Clicking on the "regional basis" tab under the cyclic voltammetry drop-down menu, restricts the integration region to the curve and line chose, and produces a result, which is printed on the screen. The coulombic charge associated with one monolayer of H_2 atoms on a Pd surface is 212μC/cm^2. Using this value, the coulombic charge calculated can be converted to surface area, i.e. electrochemically active surface area. The same procedure can be repeated to integrate over the oxide peak as well, as was done for comparison in this document.

Appendix D (Continued)

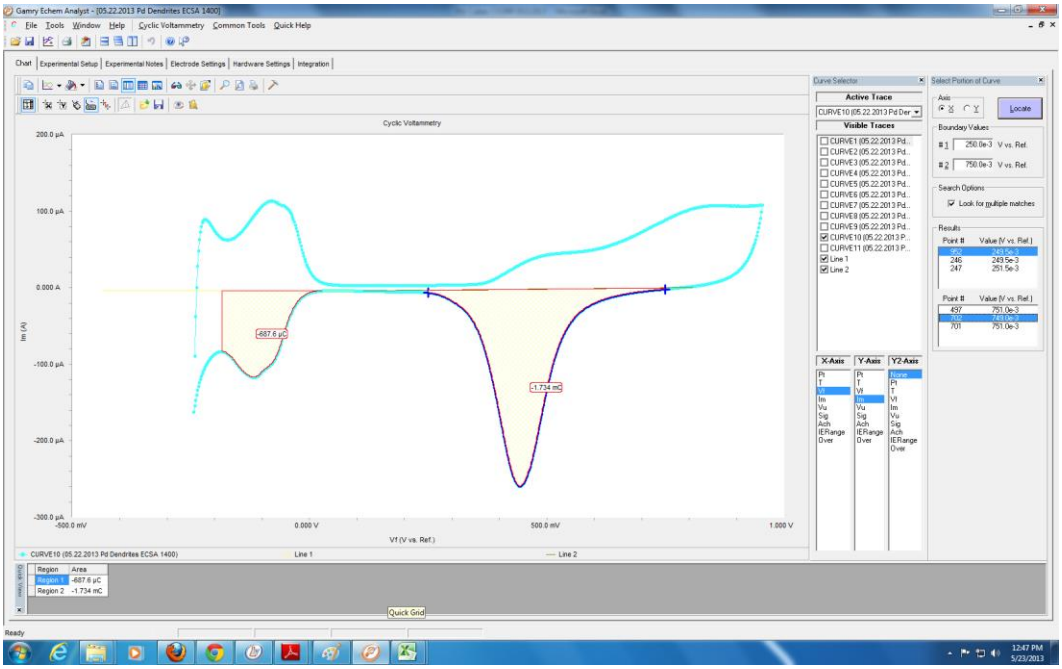

Figure D-4 EChem Analyst Screenshot of a single Cyclic Voltammogram with computationally integrated Hydrogen Evolution and Oxygen reduction peaks

ABOUT THE AUTHOR

Selasi Blavo is a currently a Doctoral Candidate in the Heterogeneous Catalysis and Materials Chemistry group of the Chemical and Biomedical Engineering of the University of South Florida, USF. Prior to USF, Selasi completed an. M.S. in Chemical Engineering at the University of Pittsburgh. Before that he earned Bachelor of Science Degrees in Chemistry and Chemical Engineering from Clark Atlanta University. His research interest is focused on the study of alternative energy technologies applications of heterogeneous catalysis, particularly in the area of PEM Fuel Cells Catalysis. However he has a broader interest in alternative energy research in general.